SeaWiFS Postlaunch Technical Report Series

Stanford B. Hooker, Editor
NASA Goddard Space Flight Center
Greenbelt, Maryland

Elaine R. Firestone, Senior Technical Editor
SAIC General Sciences Corporation
Beltsville, Maryland

Volume 9, SeaWiFS Postlaunch Calibration and Validation Analyses, Part 1

Charles R. McClain
NASA Goddard Space Flight Center
Greenbelt, Maryland

Ewa J. Ainsworth, Robert A. Barnes, Robert E. Eplee, Jr., Frederick S. Patt, and Wayne D. Robinson
SAIC General Sciences Corporation
Beltsville, Maryland

Menghua Wang
University of Maryland, Baltimore County
Baltimore, Maryland

Sean W. Bailey
Futuretech Corporation
Greenbelt, Maryland

McClain, Ainsworth, Barnes, Eplee, Patt, Robinson, Wang, and Bailey

Table of Contents

Table of Contents (Cont.)

McClain, Ainsworth, Barnes, Eplee, Patt, Robinson, Wang, and Bailey

Abstract

The effort to resolve data quality issues and improve on the initial data evaluation methodologies of the Sea-viewing Wide Field-of-view Sensor (SeaWiFS) Project was an extensive one. These evaluations have resulted, to date, in three major reprocessings of the entire data set where each reprocessing addressed the data quality issues that could be identified up to the time of each reprocessing. The number of chapters (21) needed to document this extensive work in the *SeaWiFS Postlaunch Technical Report Series* requires three volumes. The chapters in Volumes 9, 10, and 11 are in a logical order sequencing through sensor calibration, atmospheric correction, masks and flags, product evaluations, and bio-optical algorithms. The first chapter of Volume 9 is an overview of the calibration and validation program, including a table of activities from the inception of the SeaWiFS Project. Chapter 2 describes the fine adjustments of sensor detector *knee* radiances, i.e., radiance levels where three of the four detectors in each SeaWiFS band saturate. Chapters 3 and 4 describe the analyses of the lunar and solar calibration time series, respectively, which are used to track the temporal changes in radiometric sensitivity in each band. Chapter 5 outlines the procedure used to adjust band 7 relative to band 8 to derive reasonable aerosol radiances in band 7 as compared to those in band 8 in the vicinity of Lanai, Hawaii, the vicarious calibration site. Chapter 6 presents the procedure used to estimate the vicarious calibration gain adjustment factors for bands 1–6 using the water-leaving radiances from the Marine Optical Buoy (MOBY) offshore of Lanai. Chapter 7 provides the adjustments to the coccolithophore flag algorithm which were required for improved performance over the prelaunch version. Chapter 8 is an overview of the numerous modifications to the atmospheric correction algorithm that have been implemented. Chapter 9 describes the methodology used to remove artifacts of sun glint contamination for portions of the imagery outside the sun glint mask. Finally, Chapter 10 explains a modification to the ozone interpolation method to account for actual time differences between the SeaWiFS and Total Ozone Mapping Spectrometer (TOMS) orbits.

PROLOGUE

The Sea-viewing Wide Field-of-view Sensor (SeaWiFS) Project Calibration and Validation Team (CVT) is responsible for the overall quality of the data products and for verifying the processing code. The prelaunch quality control strategy was outlined in Volume 38 of the *SeaWiFS Technical Report Series* (Prelaunch). Since SeaWiFS began routine data processing in September 1997, the CVT has constantly worked to resolve data quality issues and improve on the initial data evaluation methodologies. These evaluations have resulted in three major reprocessings of the entire data set (February 1998, August 1998, and May 2000). Each reprocessing addressed the data quality issues that could be identified up to the time of each reprocessing.

The number of chapters (21) needed to document this extensive work in the *SeaWiFS Postlaunch Technical Report Series* requires three volumes: Volumes 9, 10, and 11. The chapters describe the various data quality issues, analyses, and algorithm improvements that have been developed through the third reprocessing. The data evaluations after the third reprocessing indicate that the data products, in most situations including Case-2 waters, are within the prelaunch Case-1 water accuracy goals. Nonetheless, it is expected that other improvements and new geophysical data products will be developed in the future which will require additional reprocessings. The SeaWiFS Project Office will remain dedicated to providing better products and to the documentation of future analysis and algorithm improvement studies.

A short synopsis of each chapter in this volume is given below.

*1.   SeaWiFS Postlaunch
Calibration and Validation Overview*

Since launch in August 1997, the SeaWiFS Project Office has worked diligently to improve all aspects of the mission, including refinements in mission operations, navigation accuracy, data processing efficiency, user and field operations support, and data product quality. Data product quality is the responsibility of the CVT. The work of the CVT prior to launch is largely documented in the *SeaWiFS Technical Report Series* (Prelaunch) and other published documents, including journal articles. Once operational SeaWiFS data processing began in September 1997, the CVT has made many improvements in the prelaunch processing algorithms as a result of innumerable analyses and evaluations. This three-volume set in the *SeaWiFS Postlaunch Technical Report Series* documents the major improvements and analyses that have been completed up to the third reprocessing in May 2000. These improvements have been incremental and have previously spawned reprocessings in January and August 1998. This chapter provides a review of the CVT activities and procedures.

2. Cloud-Top Radiance Analysis for SeaWiFS Bilinear Gain Knee Calibration

The distribution of cloud-top radiances in the vicinity of the knees of the SeaWiFS bilinear gains are used to determine the saturation counts for the ocean detectors more precisely than is possible based on prelaunch calibration data alone. Although the adjusted knee counts have little effect on the ocean data, they should significantly improve the determination of the radiances of thin dust and clouds in the vicinity of, and above, the knees.

3. Lunar Data Analysis for SeaWiFS Calibration

The SeaWiFS CVT uses monthly lunar calibrations to monitor the long-term stability of the radiometric calibration of SeaWiFS. The time series of lunar observations are used to compute time correction factors for the SeaWiFS bands, which are incorporated into the calibration table. The response of band 7 has decreased by 3.4%, the response of band 8 has decreased by 9.9%, and the response of bands 1–6 have decreased by less than 1%, over the course of the mission. The calibration table will be updated as required by the on-orbit performance of the instrument.

4. Solar Data Analysis for SeaWiFS Calibration

Daily solar calibrations are used to monitor the short-term variability in the radiometric response of SeaWiFS in between the monthly lunar calibrations. The time series of solar observations show the effects of both the degradation of the reflectance of the solar diffuser and the change in response of the instrument. The ratio of the band 7 time series to the band 8 time series, which minimizes the effects of the diffuser degradation, shows that the change in response of bands 7 and 8 in the solar data tracks the change observed in the lunar data.

5. Vicarious Calibration of SeaWiFS Band 7

A technique for vicariously calibrating the gain in the SeaWiFS band 7 is described in this chapter, as well as the details of its implementation. The technique has been found to provide a consistent estimate of the gain over the life of the SeaWiFS Project.

6. MOBY Data Analysis for the Vicarious Calibration of SeaWiFS Bands 1–6

The CVT performs the vicarious calibration of Sea-WiFS by comparing normalized water-leaving radiances retrieved from SeaWiFS imagery with contemporaneous measurements of normalized water-leaving radiances from the Marine Optical Buoy (MOBY). This is a system-level calibration that incorporates the performance of both the sensor and the atmospheric correction algorithm. The vicarious gains for bands 1–6 depart from unity over a range of approximately 1–4%, depending on the band, which is consistent with the uncertainty in the prelaunch calibration of SeaWiFS.

7. The Updated SeaWiFS Coccolithophore Algorithm

A coccolithophore identification algorithm has been adapted to work reasonably well for SeaWiFS data containing coccolithophore blooms at a number of sites in the Bering Sea and the North Atlantic. Changes were made in the initial algorithm thresholds that resulted in considerable improvements in the detection of coccolithophores for some cases. Future studies should include additional conditions which were considered in the formulation of the original coccolithophore algorithm, but not considered here—red tides, sediments, whitings, and haze. Finally, a future study may want to re-examine the predictors that are employed to detect the coccolithophore signal. The SeaWiFS 443, 510, and 555 nm bands are slightly different than the CZCS bands used to derive the current predictors. In addition, SeaWiFS has bands at 412 and 490 nm, which CZCS did not have, and these might be useful in deriving a better set of predictors to detect coccolithophores and other water types.

8. The SeaWiFS Atmospheric Correction Algorithm Updates

Modifications to the atmospheric correction algorithm for the third SeaWiFS reprocessing are described in this chapter. The updates include changes to the aerosol look-up tables, the atmospheric diffuse transmittance tables, the ocean whitecap computations, and the implementation of new Rayleigh radiance tables generated with a variety of ocean surface wind speeds. In addition, computation of a new SeaWiFS atmospheric product, the Ångström exponent, is described. These modifications significantly improve the SeaWiFS retrieval results.

9. Correction of the Sun Glint Contamination on the SeaWiFS Aerosol Optical Thickness Retrievals

For ocean color remote sensing, the measurement of radiances affected by sun glint has to be avoided or masked out. SeaWiFS has a capability of operationally tilting the sensor 20° away from nadir to minimize sun glint contamination, however, sun glint is still a factor near the subsolar point. In this chapter, results are presented which quantify the effect of sun glint contamination on the retrievals of atmospheric and bio-optical oceanic products. It was found that, although the sun glint contamination has a minor effect on the retrieved bio-optical oceanic products, the effect on the retrieved atmospheric products (e.g., aerosol optical thickness) is significant. A sun glint correction scheme is described, which was implemented in the Sea-WiFS data processing. It was found that the sun glint correction significantly improves the derived atmospheric products in the vicinity of the subsolar point.

10.   Modifications to the TOMS
Ozone Ancillary Data Interpolation

The method for interpolating the Total Ozone Mapping Spectrometer (TOMS) ozone data used for level-2 processing was changed as a result of new information about the generation of the files by the TOMS Project. The new method and comparison of the old and new results are described in this report.

Chapter 1

SeaWiFS Postlaunch Calibration and Validation Overview

Charles R. McClain
NASA Goddard Space Flight Center
Greenbelt, Maryland

Abstract

Since launch in August 1997, the SeaWiFS Project Office has worked diligently to improve all aspects of the mission, including refinements in mission operations, navigation accuracy, data processing efficiency, user and field operations support, and data product quality. Data product quality is the responsibility of the CVT. The work of the CVT prior to launch is largely documented in the *SeaWiFS Technical Report Series* (Prelaunch) and other published documents, including journal articles. Once operational SeaWiFS data processing began in September 1997, the CVT has made many improvements in the prelaunch processing algorithms as a result of innumerable analyses and evaluations. This three-volume set in the *SeaWiFS Postlaunch Technical Report Series* documents the major improvements and analyses that have been completed up to the third reprocessing in May 2000. These improvements have been incremental and have previously spawned reprocessings in January and August 1998. This chapter provides a review of the CVT activities and procedures.

1.1 INTRODUCTION

The SeaWiFS calibration and validation program has four basic areas of responsibility:

1) Providing the processing algorithms;

2) Verifying and documenting the level conversion processing code, i.e., level-0 through level-3;

3) Tracking sensor performance and calibration from fabrication throughout the lifetime of the mission; and

4) Verifying the quality of the data products.

These responsibilities encompass a broad range of scientific and technological areas of expertise. Given the original 28-month launch schedule, the SeaWiFS Project was hard pressed to define and implement a viable capability for mission operations, data capture, calibration and validation, and data processing.

For the CVT, the principal group that was originally identified by NASA management to assist the SeaWiFS Project was the Moderate Resolution Imaging Spectroradiometer (MODIS) Oceans Team. The SeaWiFS Project directly funded members of that team (H. Gordon, R. Evans, D. Clark, and K. Carder) to accelerate their respective activities and to assist the SeaWiFS Project in preparing for launch.

The CVT also sought the participation and assistance of the ocean color community, fully recognizing that successful fulfillment of its objectives required the participation of a broader community. In many cases, this assistance was funded under grants and contracts, but most often, it was provided by individual researchers on a voluntary basis. As part of this process, the CVT identified areas where the community infrastructure and capability was lacking or nonexistent for supporting a global ocean color mission.

To address the identified deficiencies, the CVT and the SeaWiFS Project Office initiated or accelerated a number of efforts:

1) Measurement protocols;

2) Instrument intercalibrations organized as SeaWiFS Intercalibration Round-Robin Experiments, (SIRREXs);

3) Bio-optical data archiving within the SeaWiFS Bio-optical Archive Storage System, (SeaBASS);

4) Prelaunch Bio-optical Algorithm Working Group†;

5) Advanced laboratory and *in situ* measurement technology;

---

† After launch, the Sensor Intercomparison and Merger for Biological and Interdisciplinary Oceanic Studies (SIMBIOS) program assumed many of the responsibilities related to algorithm development.

6) *SeaWiFS Technical Report Series*† and;

7) Imagery visualization and analysis with the Sea-WiFS Data Analysis System (SeaDAS)‡

Over the course of the extended prelaunch- and operational phases of the project, the CVT conducted and participated in many activities which are summarized in Table 1 and are reviewed in Hooker and McClain (2000).

The revised set (the third reprocessing) of archive geophysical data parameters and the quality control masks and flags are listed in Table 2. Level-1a data are in sensor counts and is navigated, but requires a separate transformation provided by the CVT to convert counts to radiance. The level-2 and -3 products are in geophysical units, e.g., milligrams per cubic meter ($\mathrm{mg\,m^{-3}}$). It is expected that the archive product list will grow as the ocean community defines new products and algorithms and as other Earth science disciplines begin using SeaWiFS data for atmospheric and terrestrial applications. Indeed, the SeaWiFS Project is actively encouraging the development of new products and applications and has worked with other groups to generate non-archive evaluation products, such as the normalized difference vegetation index (NDVI) over land. The SeaWiFS Project, however, does not have the expertise nor the resources to verify non-oceanic products.

1.2 DATA PROCESSING ALGORITHMS

Data processing algorithms include those for sensor calibration, stray light, atmospheric correction, bio-optical properties, masks, flags, and level-3 binning. There is a substantial amount of literature available on these topics for which Table 1 provides many of the references. It is not sufficient to simply verify and document individual algorithms—the organization, links, and sequences of data manipulations within the data processing system must also be described (Darzi 1998). A major component of all this is the creation of the file specifications and input–output routines. Much of this was undertaken by the CVT. In fact, SeaWiFS was one of the first NASA projects to adopt the hierarchical data format (HDF) and worked with the National Center for Supercomputing Applications (NCSA) during the HDF development.

The prelaunch verification of the processing was greatly facilitated by creating simulated data (Gregg et al. 1993 and 1994) by the Mission Operations Element and routine

---

† The *SeaWiFS Technical Report Series* (pre- and postlaunch) are funded by the SeaWiFS Project Office. The majority of volumes are authored by members of the CVT and its collaborators.

‡ The SeaDAS interactive image processing software currently supports processing from the Coastal Zone Color Scanner (CZCS), SeaWiFS, the Ocean Color and Temperature Scanner (OCTS), and the Marine Optical Spectroradiometer (MOS). In addition, it supports the display of MODIS ocean products.

---

end-to-end processing coordinated by the Data Processing Element. The CVT worked closely with the algorithm providers, especially the University of Miami collaborators (H. Gordon, R. Evans, J. Brown, and others), who provided much of the level-2 and -3 processing code. As a result of the extensive prelaunch testing, data flowed through the processing system and to the GSFC Distributed Active Archive Center (DAAC) within hours of the first OrbView-II transmission to the receiving station at the NASA Wallops Flight Facility.

During the 120 day postlaunch data acceptance period, the CVT performed extensive analyses to verify that the acceptance criteria (Hooker and McClain 2000) were satisfied and presented its findings at a miniworkshop with members of the MODIS Oceans Team. Corrections to the operational algorithms during the first four months culminated in the first reprocessing in January–February 1998. More substantial changes, including incorporating time-dependent adjustments to the sensor calibration, necessitated the second (August–September 1998) and third (May 2000) reprocessings. Robinson et al. (2000) summarized the primary changes for each reprocessing. Preparations for the third reprocessing included two miniworkshops where algorithm issues were reviewed and evaluation strategies were defined. The results of analyses conducted in preparation for the second and third reprocessings were posted on project web sites for consideration by the user community. Finally, for the third reprocessing, all level-1, -2, and -3 processing codes were rewritten and streamlined.

1.3 SENSOR CALIBRATION

Table 1 is a list of the various activities and accomplishments of the CVT including documents dealing with the SeaWiFS calibration and characterization and processing algorithms. In the postlaunch phase, the CVT has pursued a variety of analyses for tracking the on-orbit behavior of the instrument, which are included in the following list.

A. Prelaunch

1. Laboratory sensor characterization and calibration

2. Solar calibration for a *transfer-to-orbit* comparison

B. Postlaunch

1. Operational Adjustments

a. Lunar calibration (monthly) for time dependence correction

b. Solar calibration (daily) for time dependence (bands 7 and 8) and fine resolution check of lunar correction

c. Open ocean $\epsilon(765, 865)$ analysis for vicarious calibration (band 7)

d. MOBY L_{WN} time series for vicarious calibration (bands 1–6)

Table 1. Specific activities and accomplishments of the SeaWiFS CVT and collaborators. The term "Vol." indicates a *SeaWiFS Technical Report Series Prelaunch* volume (Appendix A), and the term "Vol. " indicates a *Postlaunch* volume (Appendix A). The CVT web site is located at `http://seawifs.gsfc.nasa.gov/~grey/calval.html`.

Activity or Accomplishment	Reference
Round-Robins and Measurement Protocols	
Seven instrument calibration round-robins	Vols. 14, 16, 34, 37, and Vols. 7
Joint US–Japan SeaWiFS–OCTS	Johnson et al., 1997
prelaunch cross-calibration	Johnson et al., 1997
Data collection protocols	Vols. 5 and 25 (revision)
Data analysis round-robin	Vol. 26
High performance liquid chromatography (HPLC) round-robin	Vol. 14
Tower shading effects experiment	Zibordi et al. 1999
Two measurement protocol experiments	Vols. 3 and 8
Advanced Instrumentation and Community Support	
SeaWiFS SWG *in situ* radiometer calibration support	CHORS, 1992–1995
SeaWiFS Transfer Radiometer (SXR)	Vol. 1
SeaWiFS Quality Monitor (SQM)	Johnson et al. 1998; Hooker and Aiken 1998
SeaPRISM[1] development with the JRC[2]	Vol. 13
NASA Environmental Sampling System development	Hooker and Maritorena 2000
SeaWiFS Sensor Calibration and Characterization	
Two prelaunch solar-based calibration experiments	Vols. 19 and 27
Prelaunch acceptance report	Vol. 22
Prelaunch calibration reports	Vol. 23 and Vol. 4
Stray light description	Vol. 31
Solar diffuser design	Vol. 39
Calibration temperature dependence	Vol. 40
Postlaunch data acceptance evaluation	December 1997
Science quality data certification	McClain et al. 1998
Lunar and solar data analysis procedures	Barnes et al. 1999a
Prelaunch solar calibration transfer to orbit analysis	Vol. 5
Co-Funded MODIS Oceans Team Activities	
Atmospheric corrections	Gordon
Semi-analytical chlorophyll algorithm	Carder
In situ vicarious calibration	Clark
Three operational MOBYs and one shipboard spectrometer	Clark et al. 1997
Support facility in Honolulu and routine deployments	July 1997–present
Two Marine Optical Characterization Experiments (MOCE)	Clark
Postlaunch data acceptance workshop	
SeaWiFS postlaunch initialization cruise	Clark and Gordon
Additional Supported Investigations	
Atmospheric correction studies	Vols. 13, 19, and 27
Bermuda Atlantic Time Series (BATS) observations	Siegel
California Cooperative Fisheries (CalCOFI) cruises	Mitchell
Plymouth Marine Bio-Optical Data buoy (PlyMBODy)	Vol. 33
Nine Atlantic Meridional Transect (AMT) cruises with PML[3]	Vol. 35, Vol. 2, and Aiken et al. 2000
Portable optical measurements laboratory	
CTD and Niskin bottle rosette	
Bio-optical algorithm development and evaluation	O'Reilly
Acqua Alta Oceanographic Tower (AAOT) observations	Zibordi
Productivité des Systèmes Océaniques Pélagiques (PROSOPE)[4]	Claustre and Morel

Table 1. (cont.) Specific activities and accomplishments of the SeaWiFS CVT and collaborators. The term "Vol." indicates a *SeaWiFS Technical Report Series Prelaunch* volume (Appendix A), and the term "Vol. " indicates a *Postlaunch* volume (Appendix A). The CVT web site is located at `http://seawifs.gsfc.nasa.gov/~grey/calval.html`.

Activity or Accomplishment	Reference
Algorithm Development	
Workshops (Meeting summaries published)	Vols. 18, 24, 36, and 43
Seven prelaunch bio-optical algorithm and protocols workshops	
Absorption measurement workshop at SIO[5]	Mitchell
One calibration workshop	
Two atmospheric correction workshops (One was a joint meeting with MODIS Project)	
SeaWiFS Bio-optical Algorithm Mini-workshop (SeaBAM)	
SeaWiFS postlaunch data acceptance workshop	
Two SeaWiFS algorithm evaluation mini-workshops	
Atmospheric correction algorithm	Gordon and Wang 1994a, and Gordon 1995
Bio-optical data archive SeaBASS	Vol. 20
Data quality masks and flag algorithms	Vol. 28
Out-of-band effects and correction scheme	Vols. 28, 39, 40, and 41
Initial level-3 binning algorithm	Vol. 32
$K(490)$ algorithm	Vol. 41 and Vol. 11
SeaWiFS stray-light correction algorithm	Vol. 41
CZCS pigment and chlorophyll *a* algorithms	O'Reilly et al. 1998 and Vol. 11
CVT image gallery	`http://calval-2.gsfc.nasa.gov/calval/`
Quality Control (QC) Software	
Operational QC Software	Vol. 38
Level-1, -2, and -3 quality assurance	
Ancillary data quality assurance (winds, pressure, ozone)	
Derived product evaluation	
Sensor engineering telemetry data tracking (Presently handled by Mission Operations)	
Calibration evaluation (lunar, solar, vicarious)	
Operational Processing Software	
Format specifications and code for all products	`http://seawifs.gsfc.nasa.gov/SEAWIFS/ SOFTWARE/SOFTWARE.html #Product Specifications`
Documentation on final processing flow completed	Darzi 1998
Level-1, -2 and -3 code verification (At-launch and first through third reprocessings)	
SeaWiFS Data Analysis System[6] (SeaDAS)	
Three training classes	Summer 1994
Preliminary version	Summer 1994
Interactive Data Language (IDL) licenses (45 total)	Distributed to the Science Working Group
One training class	May 1995
Version 1	Summer 1995
Sun workstation delivered to Shirshov Institute (Moscow)	1995
One training class	April 1996
Version 2	May 1996
Version 3	September 1997
Seven training classes	November 1997

Table 1. (cont.) Specific activities and accomplishments of the SeaWiFS CVT and collaborators. The term "Vol." indicates a *SeaWiFS Technical Report Series Prelaunch* volume (Appendix A), and the term "Vol." indicates a *Postlaunch* volume (Appendix A). The CVT web site is located at `http://seawifs.gsfc.nasa.gov/~grey/calval.html`.

Activity or Accomplishment	Reference
SeaDAS (cont.)	
Version 3.1	February 1998
Two training classes	July 1998
Version 3.2	October 1998
Version 3.3	April 1999
Linux version	May 1999
Version 4	May 2000

1. SeaPRISM is the SeaWiFS Photometer Revision for Incident Surface Measurement.
2. JRC is the Joint Research Centre (Ispra, Italy).
3. PML is the Plymouth Marine Laboratory (Plymouth, England).
4. The French meaning for PROSOPE translates to productivity of pelagic oceanic systems.
5. SIO is the Scripps Institution of Oceanography.
6. SeaDAS is primarily funded by the NASA Oceanography Program, however, the SeaWiFS Project is presently providing the funding needed for equipment upgrades and system administration assistance. The SeaDAS staff rely largely on the CVT for processing code.

Table 2. SeaWiFS archived atmospheric and ocean surface products for the third reprocessing. The QC masks and flags are listed as well because some are used as exclusion criteria for the level-3 binning. The Tilt and Sensor Engineering Limits flags are applied line-by-line and are not represented in the level-2 products as graphic overlays.

Level	Product Type	Product Name
Level-1	Geolocated Sensor Counts†	
Level-2	Ocean Products	L_{WN}(412, 443, 490, 510, 555, and 670 nm) accuracy goal: $\pm5\%$ Chlorophyll a accuracy goal: $\pm35\%$ in Case-1 water $K(490)$
	Atmospheric Products	$\gamma(510, 865)$ (Ångström exponent) $\tau_a(865)$ $\epsilon(765, 865)$
	QC Masks	Land‡ Cloud and ice‡ Sun glint‡ Atmospheric correction failure or invalid data‡ High L_t‡
	QC Flags	Large solar zenith angle (increased to 75°) ‡ Large satellite zenith angle‡ Negative L_W (bands 1–5)§ Stray light‡ Coccolithophore‡ Low $L_{WN}(555)$‡ Outside chlorophyll a algorithm range (0–64.0) Missing ancillary data Turbid Case-2 water Shallow water High $\tau_a(865)$ Tilt underway‡ Absorbing aerosol‡ *Trichodesmium*

Table 2. (cont.) SeaWiFS archived atmospheric and ocean surface products for the third reprocessing. The QC masks and flags are listed as well because some are used as exclusion criteria for the level-3 binning. The Tilt and Sensor Engineering Limits flags are applied line-by-line and are not represented in the level-2 products as graphic overlays.

Level	Product Type	Product Name
Level-2	QC Flags	Chlorophyll algorithm failure‡ Maximum number of NIR iterations exceeded‡ Sun glint correction $L_r > L_t$ Atmospheric correction warning‡
Level-3	Binned Products	All level-2 fields $C_a{:}K$ [ratio of chlorophyll $a/K(490)$]

† CVT provides calibration tables to convert counts to radiance separately.
‡ Masks and flags used as exclusion criteria in the generation of level-3 binned products.
§ Values set to zero for binning.

C. Product Evaluations

1. Global clear-water time series (8-day binned data) using L_{WN} (bands 1–6) $\epsilon(765, 865)$, $\tau_a(865)$, chlorophyll a, number of clear-water bins

2. $L_t - L_r < 0$ and negative L_W analyses (statistics and global distributions)

3. $\tau_a(865)$ comparisons with Aerosol Robotic Network (AERONET) data and SeaWiFS

4. L_W and L_{WN} comparisons (*in situ* versus SeaWiFS)

5. Chlorophyll a and $K(490)$ comparisons (*in situ* versus SeaWiFS)

6. E_s (surface irradiance) comparisons (*in situ* versus theoretical clear-sky values)

7. Global time series of the mean cloud albedo at 865 nm (inconclusive and discontinued)

8. Earth curvature effects on L_r estimates

9. f/Q corrections (bidirectional reflectance) to L_W values (Morel and Gentili 1996)

10. Effects of alternative solar spectra, $F_0(\lambda)$, on vicarious calibrations and derived products

11. Band 8 calibration evaluation using clear sky, low chlorophyll region along Antarctic coast

Of the postlaunch analyses, all are described in detail in various chapters of this volume with the exception of the cloud albedo time series. The cloud albedo time series proved to be very noisy; it was dropped after the lunar and solar calibrations were shown to be very robust for tracking sensor degradation.

The overall scheme for sensor calibration is shown in Fig. 1; it illustrates how the various prelaunch and postlaunch calibrations are connected. The lunar calibration is used to remove any time dependence in the sensitivity (Eplee and Barnes 2000); the solar calibration is used as a cross check of the lunar measurements for bands 7 and 8 (Eplee et al. 2000). Because there is no accurate method for vicariously calibrating band 8 at this time, the prelaunch calibration is assumed. This assumption is verified to within $\pm 2\%$ by the solar calibration transfer-to-orbit results (Barnes et al. 1999b). These results are supported by an analysis of clear sky (cloud albedo threshold set at 0.35), low chlorophyll waters, i.e., no NIR reflectance, along the Antarctic coast near 60°S,25°E during November 1997 through January 1998. Under these conditions, $L_t(865)$ always exceeded $L_r(865)$, i.e., band 8 is not undercalibrated, and the average $\tau_a(865)$ value was around 0.01, similar to the minimum values observed at the McMurdo research station in the Antarctic during the same time, i.e., band 8 is not significantly overcalibrated.

After the time dependencies are removed, the prelaunch calibration coefficients (Johnson et al. 1999) for bands 1–6 are adjusted using MOBY matchups to minimize the average differences between the buoy and SeaWiFS normalized water-leaving radiances (Eplee and McClain 2000). The band 7 (765 nm) calibration is adjusted so the atmospheric correction parameter at 765 and 865 nm, $\epsilon(765, 865)$, is near the expected value at the MOBY site (Robinson and Wang 2000). Checks of the results of this process include analyses of the eight-day global binned products to verify that no unexpected trends are occurring. For example, the second global reprocessing was initiated when it was realized that bands 7 and 8 were degrading. This degradation resulted in a steady increase in the $\epsilon(765, 865)$ values with a commensurate gradual decrease in the global mean clear-water radiances.

Match-up analyses using independent *in situ* data are also used for verification (Bailey et al. 2000). These analyses show that the SeaWiFS clear-water radiances after the second reprocessing compare very well with the *in situ* values suggesting that the sensor calibration is correct. The comparisons, however, over regions of high chlorophyll and
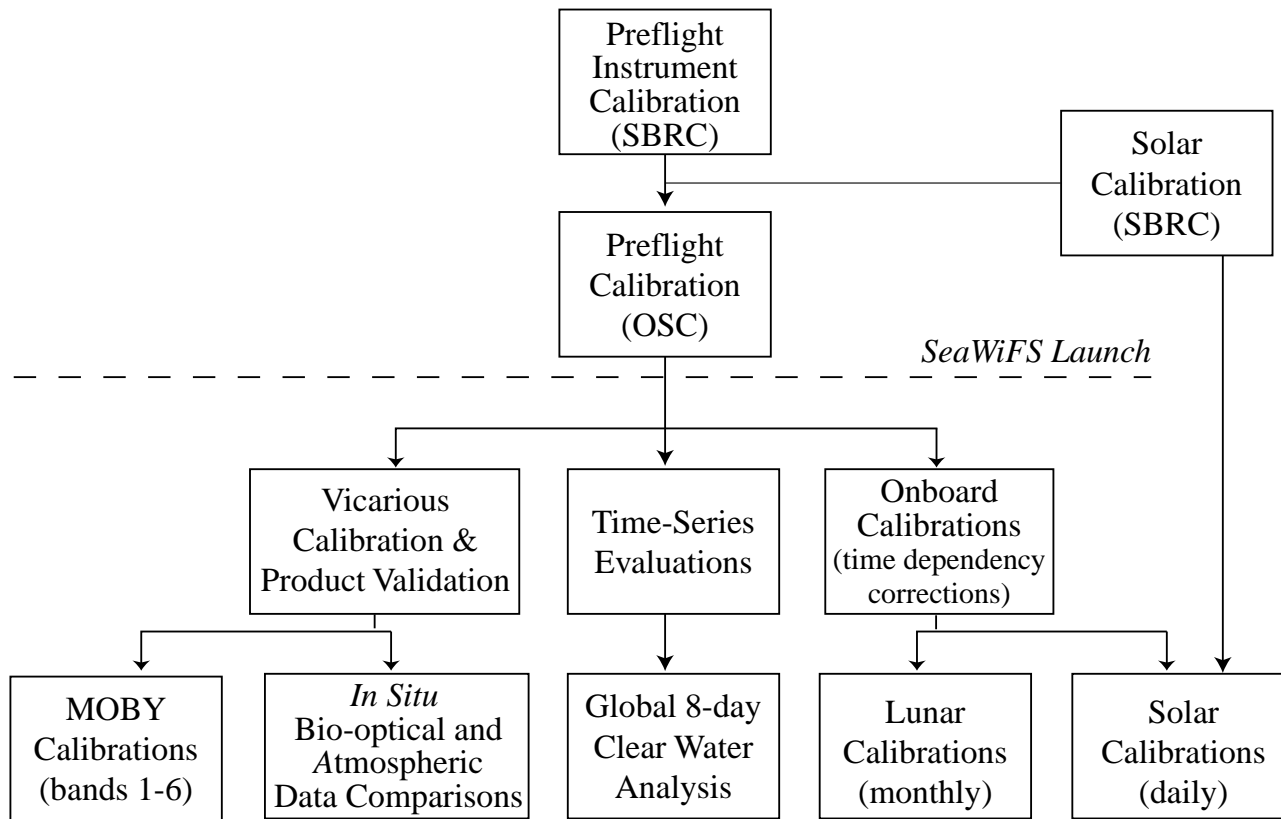
Fig. 1. Schematic of the SeaWiFS calibration chronology and methods.

turbid water show that the SeaWiFS water-leaving radiances are low, particularly at 412 and 443 nm, which has been attributed to the assumption of zero water-leaving radiance at 765 and 865 nm in the atmospheric correction algorithm. One of the primary reasons for initiating the global third reprocessing is to address this problem. Below is an outline of the entire calibration verification procedure.

A. Determine temporal degradation lunar calibration data

    1. Degradations in bands 1, 2, 5, 6, 7, and 8 observed

B. Determine nominal L_{WN} values from MOBY

    1. Use the same values as used in MOBY–SeaWiFS match-up data set

C. Set band 7 calibration correction factor

    1. Assume band 8 prelaunch calibration

        a. Calibration correction factor = 1.0

        b. Time-dependent degradation correction from lunar data

    2. Adjust band 7 calibration factor to get appropriate mean $\epsilon(765, 865)$ value

        a. Time-dependent degradation correction from lunar data

        b. Use MOBY LAC time series

D. Analyze MOBY L_{WN} data for bands 1–6

    1. Use theoretical E_s values

2. Check for trends in time series

3. Use MOBY LAC time series

4. Apply exclusion criteria to match-up data set

5. Adjust calibrations to minimize SeaWiFS–MOBY L_{WN} differences for valid match-up data

    a. Compute geometric mean of match-up ratios

    b. Generate final calibration adjustment factors

E. Check global clear-water L_{WN} values from eight-day composite time series and compare them with nominal MOBY clear-water values

F. Evaluate mask and flag performance (e.g., cloud and coccolithophore)

G. Run match-up analyses on other ship and buoy data for verification of clear-water L_{WN} values

1.4 PRODUCT VALIDATION

Product validation consists of match-up analyses and real-time quality control. McClain et al. (1996) outline the various analyses that were envisioned prior to launch. Since launch, these analyses have been substantially expanded and refined as is outlined in this volume. All global area coverage (GAC) and local area coverage (LAC), including high resolution picture transmission (HRPT) station data products, are passed through automated checks

and visual inspections before being approved for archiving at the GSFC DAAC. Not every file can be reviewed visually, but those that trigger a flag from the automated checks are inspected.

Another aid in diagnosing problems is the routine generation of quality control products which are not archived and are automatically purged after a certain period of time. The quality control products up to the third reprocessing were:

a) Zonal wind;

b) Ozone;

c) Sensor azimuth angle;

d) $L_r(443)$;

e) Second aerosol model;

f) Merdional wind;

g) Solar zenith angle;

h) $L_{WN}(670)$;

i) $L_g(865)$;

j) Surface pressure;

k) Albedo at 865 nm;

l) $L_a(765)$;

m) $L_f(865)$;

n) Precipitable water;

o) Sensor zenith angle;

p) $L_t(443)$;

q) First aerosol model; and

r) $\epsilon(765, 865)$ flag, i.e., pixels having values outside the range of valid $\epsilon(765, 865)$ values.

These products were discontinued once the third reprocessing commenced, as their routine generation was no longer necessary for product evaluation.

The other aspect of quality control is the definition of quality control masks and flags. These are listed in Table 2 along with the level-3 exclusion criteria. Pixels that are masked are not processed to level-2. Pixels that are flagged are processed, but are not necessarily included in the level-3 products. Beginning with the third reprocessing, suites of quality control products and masks and flags will be refined at each reprocessing. It should be noted that the present suit of masks and flags are designed to optimize the accuracy of the chlorophyll a product. In the future, as suites of products for atmospheric, terrestrial, and other ocean parameters are defined, each will need its own set of masks and flags.

Finally, the CVT works closely with the SIMBIOS Project (McClain and Fargion 1999), which is co-located with the SeaWiFS Project, to provide cruise support so as to optimize the collection of *in situ* data with respect to the SeaWiFS coverage. This support includes overpass predictions in advance to assist researchers planning ship tracks and station times. The project provides real-time data products, which can be tailored to the researchers' needs via the SIMBIOS web site†. These products can be electronically mailed to the ship or to a point of contact. In addition, if the ship locations are known a week or more in advance of the satellite overpass, onboard LAC data can be scheduled to ensure that high resolution data over the ship will be available for match-up analyses.

During the first two years of operations, the project supported 125 field studies. In addition, LAC data are routinely scheduled over time series sites, such as MOBY, the AAOT site (offshore of Venice, Italy); the BATS site; the Hawaii Ocean Time-series (HOT) site; certain Tropical Ocean Global Atmosphere (TOGA) program Tropical Atmosphere–Ocean (TAO) moorings; and others. LAC recorder space that is not used to cover validation targets is used over default regions of interest, such as the Galapagos Islands. Figure 2 provides a typical LAC data collection summary. The SIMBIOS program supports a number of *in situ* data collection activities including cruise and mooring bio-optical data and aerosol optical thickness from a number of AERONET sites. The match-up methodology for atmospheric parameters is outlined in Wang et al. (2000).

1.5 SUMMARY

Since the inception of the SeaWiFS Project in the early 1990s, the CVT has labored diligently to ensure that a comprehensive and effective calibration and validation program was in place by launch. The four-year launch delay allowed time for many capabilities to be realized in time for launch. The overall philosophy of the CVT has been to involve the research community as partners and to initiate activities which develop community infrastructure. In order to gain a better appreciation for the challenges of field data collection, the CVT has developed its own field program dedicated to improving measurement accuracy and collecting high quality bio-optical data. Dr. Stanford Hooker leads this effort and has been actively involved in the AMT program (Robins et al. 1996 and Aiken et al. 1998), the PROSOPE cruise, and a variety of measurement protocol experiments on the AAOT platform (Hooker et al. 1999).

With each reprocessing, significant improvements in the data products have been achieved. After the second reprocessing, problems with low or negative water-leaving radiances persisted in certain situations. As a result, improvements have been made in a number of algorithms in preparation for the third reprocessing:

1. Sensor degradation correction (Eplee and Barnes 2000);

2. Bilinear gain knee offset adjustments (Eplee and Patt 2000);

3. Improved ozone interpolation scheme (Ainsworth and Patt 2000);

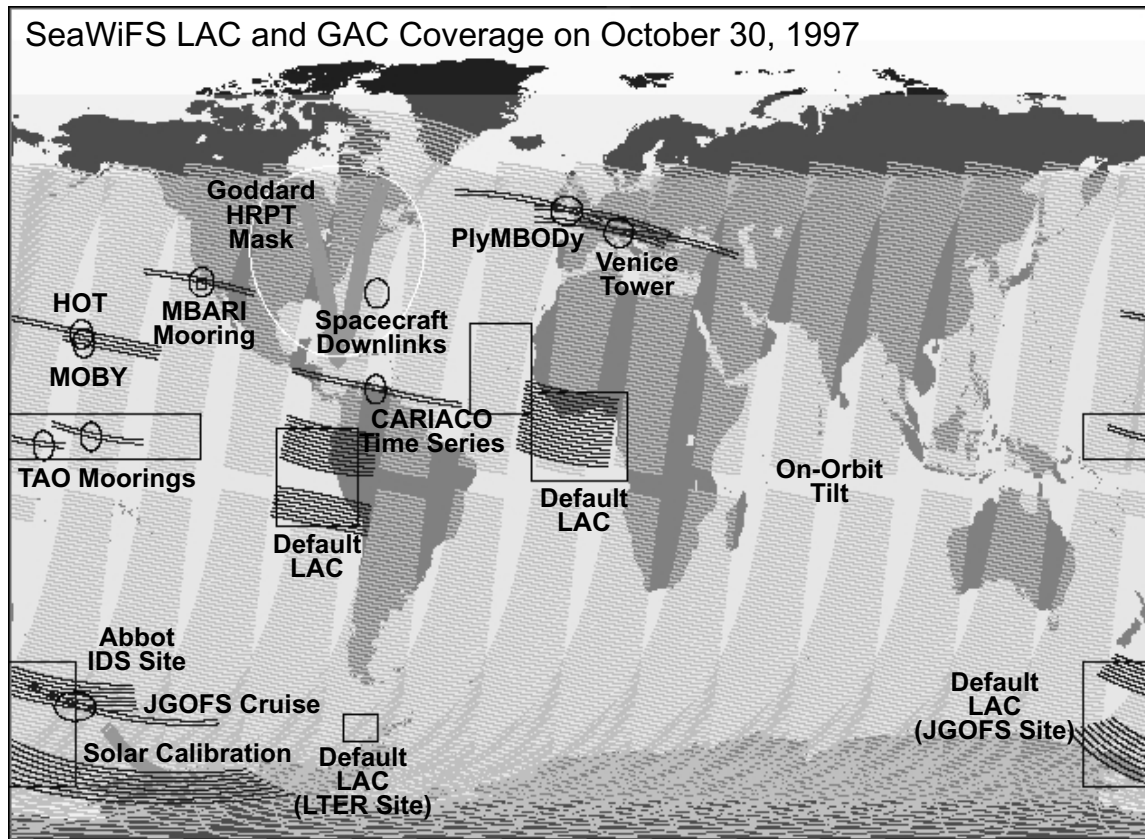† SIMBIOS URL: `http://simbios.gsfc.nasa.gov`

Fig. 2. A typical daily SeaWiFS onboard LAC data collection schedule.

4. Sun glint correction algorithm (Wang and Bailey 2000);

5. Surface whitecap correction (Robinson et al. 2000);

6. Various atmospheric correction algorithm improvements (Wang 2000 and Siegel et al. 2000);

7. Absorbing aerosol detection (Hsu et al. 2000);

8. Out-of-band corrections to L_W values (Wang et al. 2000);

9. $K(490)$ algorithm (Mueller 2000); and

10. Improved chlorophyll a algorithms (O'Reilly et al. 2000).

These improvements were incorporated in the third reprocessing.

Other potential improvements were evaluated, but not incorporated. For instance, the Rayleigh radiance model was compared to other models, some with Earth curvature effects included. No significant differences were found for solar zenith angles that were less than 70°. In addition, the bidirectional reflectance algorithm of Morel and Gentili (1996) was tested, but the use of the algorithm was deferred until certain improvements could be implemented. In addition, a different solar spectrum was tried, but it yielded almost identical results as the current spectrum, because the vicarious calibration compensates for the differences.

As further improvements and new products are defined, annual reprocessings are anticipated; the CVT will continue to work with the Data Processing Element on how processing efficiency can be maximized as the SeaWiFS data set grows.

Chapter 2

Cloud-Top Radiance Analysis for SeaWiFS
Bilinear Gain Knee Calibration

ROBERT E. EPLEE, JR., AND FREDERICK S. PATT
SAIC General Sciences Corporation
Beltsville, Maryland

ABSTRACT

The distribution of cloud-top radiances in the vicinity of the knees of the SeaWiFS bilinear gains are used to determine the saturation counts for the ocean detectors more precisely than is possible based on prelaunch calibration data alone. Although the adjusted knee counts have little effect on the ocean data, they should significantly improve the determination of the radiances of thin dust and clouds in the vicinity of, and above, the knees.

2.1 INTRODUCTION

An examination of histograms of cloud-top radiances observed by SeaWiFS shows anomalous distributions of radiances in the vicinity of the knee of the bilinear response for each SeaWiFS band. These anomalous distributions are observed in HRPT, LAC, and GAC images. Typical histograms for HRPT images, which are plotted for each band in Fig. 3, show unexpected discontinuities in the distribution of radiances in the vicinity of the knees: there are fewer pixels at the knee radiances than expected from the number of points with radiances below and above the knees. These discontinuities in the radiance distribution would give rise to errors in the retrieved radiances of thin dust and thin clouds, as measured by SeaWiFS.

Each SeaWiFS band has three ocean detectors with high radiometric sensitivity and low saturation radiances, and one cloud detector with low radiometric sensitivity and high saturation radiances. During the collection of ocean data, SeaWiFS averages the output from the four detectors within each band. The knees in the response occur where the ocean detectors saturate. Figure 4 shows bilinear response for bands 1–8 in the vicinity of the knees. A plot of the biliner response of band 1 over the full dynamic range of the instrument is shown in Fig. 8 of Johnson et al. (1999).

The discontinuities in radiance in the vicinity of the knees of the bilinear response are caused by uncertainties in determining the output counts at which saturation occurs for the ocean detectors. The prelaunch radiometric calibration of SeaWiFS was performed in the laboratory at four radiance levels, which were either below or above the knee radiances (Johnson et al. 1999). Sunlight reflected from cloud tops provides a continuum of radiances in the vicinity of the knees. The CVT has undertaken an analysis of the distribution of cloud-top radiances measured by SeaWiFS to make a more precise determination of the saturation counts for the ocean detectors than is possible based on the prelaunch calibration data alone.

2.2 DETERMINING KNEE COUNTS

The CVT can adjust the counts at which saturation occurs for each detector in the SeaWiFS calibration model by changing the offsets used in computing the counts-to-radiance conversion factors from the detector gains (Darzi et al. 1995). The CVT performed the adjustment for a given band with a *trial-and-error* approach, where the offsets for each detector were changed individually and the resulting radiance distribution was examined. The goal of these adjustments was to improve the distribution of radiances in the vicinity of the knees for each band. The final offsets were those which yielded the smoothest radiance distrubutions at the knees. Because SeaWiFS only collects ocean data for gain 1, this knee calibration can only be performed at this gain.

Figure 3 also shows the radiance distributions resulting from the modified knees for bands 2–8. For each of these bands, the distribution for the modified knees is an improvement over the original distribution. A correction could not be determined for band 1 because a one count adjustment of the saturated counts for this band resulted in a poorer radiance distribution. Figure 4 shows the locations of the modified knees for each band.
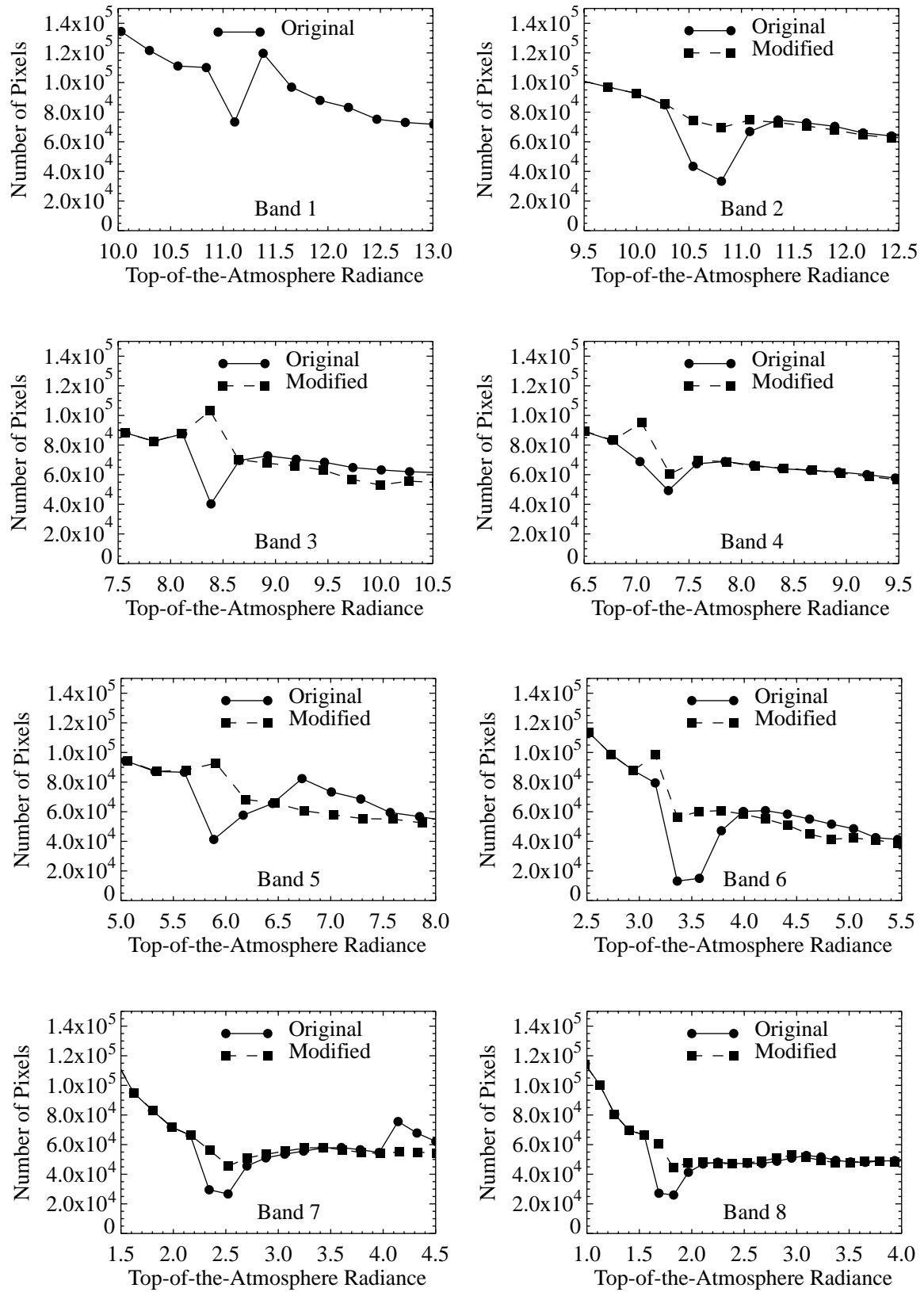
Fig. 3. Histograms of radiance distributions in the vicinity of the knees in the bilinear radiometric response.
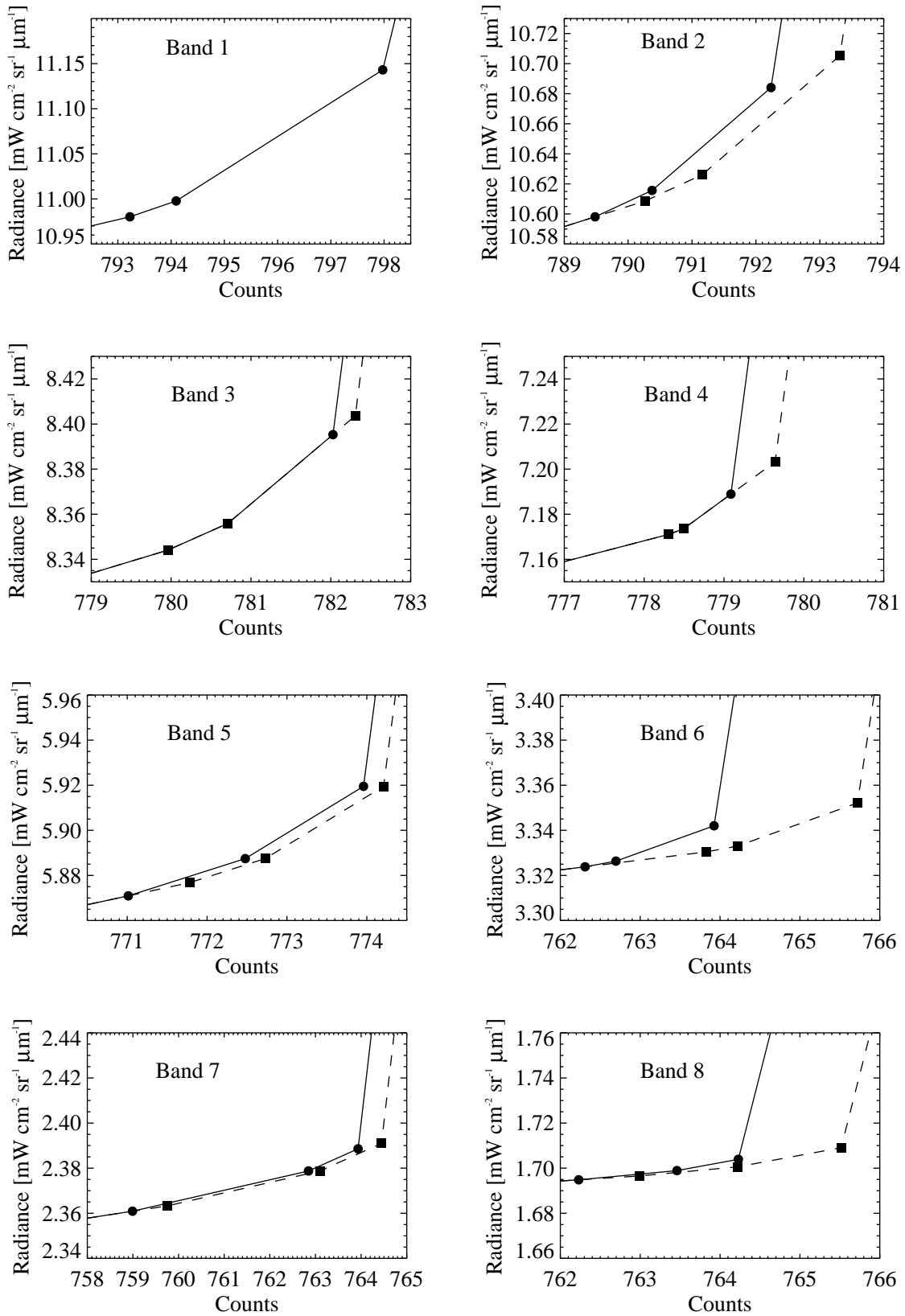
Fig. 4. SeaWiFS bilinear radiometric response in the vicinity of the knees.

Table 3. Knees of the original SeaWiFS bilinear gains for gain 1.

Band	Knee 1		Knee 2		Knee 3		Saturation	
	Radiance	Counts	Radiance	Counts	Radiance	Counts	Radiance	Counts
1	10.98	793.23	11.00	794.10	11.14	797.98	60.69	1002.25
2	10.60	789.48	10.62	790.37	10.68	792.24	68.85	1004.50
3	8.344	799.96	8.356	780.71	8.395	782.03	69.46	1002.25
4	7.171	778.31	7.174	778.50	7.189	779.09	67.10	1002.75
5	5.871	771.01	5.887	772.48	5.920	773.96	67.19	1001.25
6	3.324	762.31	3.326	762.70	3.342	763.93	57.05	999.75
7	2.361	758.99	2.379	762.85	2.389	763.93	43.64	1000.25
8	1.695	762.23	1.699	763.46	1.704	764.23	34.94	1002.75

Table 4. Knees of the modified SeaWiFS bilinear gains for gain 1.

Band	Knee 1		Knee 2		Knee 3		Saturation	
	Radiance	Counts	Radiance	Counts	Radiance	Counts	Radiance	Counts
1	10.98	793.23	11.00	794.10	11.14	797.98	60.69	1002.25
2	10.61	790.27	10.63	791.16	10.71	793.31	68.85	1005.50
3	8.344	799.96	8.356	780.71	8.404	782.31	69.46	1002.50
4	7.171	778.31	7.174	778.50	7.203	779.64	67.10	1003.25
5	5.877	771.78	5.887	772.73	5.920	774.21	67.19	1001.50
6	3.330	763.83	3.333	764.22	3.352	765.72	57.05	1001.50
7	2.363	759.75	2.379	763.10	2.391	764.45	43.64	1000.75
8	1.697	762.99	1.701	764.22	1.709	765.52	34.94	1004.00

The change in location of the knee radiances and counts for each band is also shown by comparing Tables 3 and 4, which list the radiance and counts at the three knees before and after the adjustments of the offsets. The changes in the saturated counts at the knees are from 0.0–1.8 counts, with a mean of 0.6 counts. The typical change in the radiance for a given instrument output below the knee is 0.1%, which is within the uncertainty of the instrument calibration (Johnson et al. 1999). The typical change in the radiance above the knee is 0.8%, which again is within the uncertainty of the instrument calibration (Johnson et al. 1999). The changes in the above-the-knee radiances should improve the determination of dust and absorbing aerosol masks for SeaWiFS (Hsu 2000). The offsets for the modified knee locations have been incorporated into the SeaWiFS calibration table which will be used for the third reprocessing of SeaWiFS data.

2.3 DISCUSSION

By using the distribution of cloud-top radiances in the vicinity of the knees of the SeaWiFS bilinear gains, the CVT made more precise determinations of the knee counts than were possible from the prelaunch calibration data. While the adjusted knee counts have little effect on the ocean data, they should significantly improve the determination of the radiances of thin dust and clouds in the vicinity of, and above, the knees.

Chapter 3

Lunar Data Analysis for SeaWiFS Calibration

ROBERT E. EPLEE, JR., AND ROBERT A. BARNES
SAIC General Sciences Corporation
Beltsville, Maryland

ABSTRACT

The SeaWiFS CVT uses monthly lunar calibrations to monitor the long-term stability of the radiometric calibration of SeaWiFS. The time series of lunar observations are used to compute time correction factors for the SeaWiFS bands, which are incorporated into the calibration table. The response of band 7 has decreased by 3.4%, the response of band 8 has decreased by 9.9%, and the response of bands 1–6 have decreased by less than 1%, over the course of the mission. The calibration table will be updated as required by the on-orbit performance of the instrument.

3.1 INTRODUCTION

The SeaWiFS CVT uses on-orbit calibration data to monitor the radiometric stability of the SeaWiFS bands over the course of the mission. Monthly lunar are used calibrations to track the long-term stability of the radiometric calibration of SeaWiFS. The time series of lunar calibrations are used to compute any time correction factors required to maintain a stable radiometric sensitivity for each of the SeaWiFS bands over the course of the mission. The lunar data analysis techniques and preliminary results were previously discussed by Barnes et al. (1998 and 1999a) and by Barnes and McClain (1999). This chapter describes how these techniques are used to generate the time corrections for the SeaWiFS calibration table.

The time correction factors are defined in the SeaWiFS level-1b calibration equation (discussed in detail in Johnson et al. 1999):

$$
\begin{aligned}
L_S(\lambda) \;=\; & \big(C_{\text{out}}(\lambda) \;-\; C_{\text{dark}}(\lambda)\big)\, K_1(g,d,\lambda) \\
& \times\, \big(1 + K_2(\lambda)\,(T \;-\; T_{\text{ref}})\big)\, K_3(\text{pxl},\lambda) \\
& \times\; M(\text{ms},\lambda)\,\alpha(\lambda)\,\big(\beta(\lambda) \;+\; \gamma(\lambda)\,(t - t_0) \\
& +\; \delta(\lambda)\,(t - t_0)^2\big),
\end{aligned}
\tag{1}
$$

where:

λ is the wavelength;

L_S is the calibrated at-sensor radiance;

C_{out} is the counts from sensor output data;

C_{dark} is the dark count from sensor output data;

K_1 is the counts-to-radiance conversion factor (calibration coefficient);

g is the gain;

d is the detector;

K_2 is the detector temperature-dependent correction factor;

T is the detector temperature from sensor output data;

T_{ref} is the reference temperature ($20°$C);

K_3 is the scan modulation correction;

pxl is the pixel number along scan line;

M is the half-angle mirror side correction factor;

ms is the mirror side (a or b);

α is the vicarious gain;

β is the constant term in temporal correction;

γ is the linear (in time) term in temporal correction;

δ is the quadratic (in time) term in temporal correction;

t is the time tag of sensor output data; and

t_0 is the reference time for temporal correction.

The reference time for the temporal correction is the time tag of the first SeaWiFS on-orbit image, which was obtained on 4 September 1997 at 162630 UTC. The current design of the SeaWiFS level-1b algorithm allows for a multisegment quadratic time correction.

3.2 LUNAR CALIBRATIONS

Lunar calibrations are performed once per month when the moon is at a phase angle (ϑ) of approximately $7°$. This phase angle is chosen to maximize the illuminated surface of the moon while minimizing the opposition effect, i.e., the increase in brightness of sunlight diffusely reflected from a
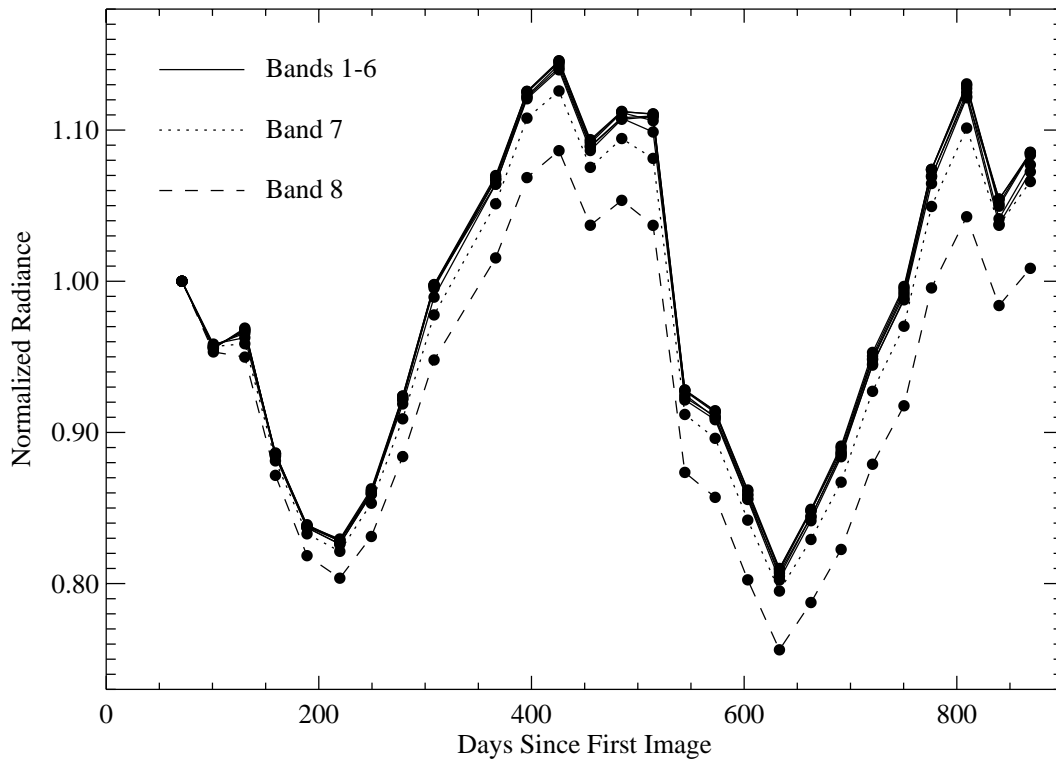
Fig. 5. Disk-integrated lunar radiances, normalized to the first calibration.

particulate surface near zero phase. Operational considerations, such as a conflict of the lunar measurement with a midnight data downlink, will require that the measurements be moved on occasion to different phase angles or from before full phase to after full phase.

SeaWiFS operates in a sun-synchronous orbit, crossing the equator from north to south at local noon. In normal operation, the spacecraft is maintained in a nadir orientation, using pitch-axis momentum wheels for attitude control, with a spacecraft pitch rate of $360°$ per orbit (about $0.06°$ per second). For lunar measurements, the rotation rate of the momentum wheels is increased and the spacecraft is pitched in the opposite direction at a rate of approximately $0.15°$ per second. The maneuver is started after the spacecraft crosses the South Pole and is timed so that SeaWiFS will view the moon as the spacecraft ground track crosses the sublunar point. At the end of the maneuver, when the spacecraft again points toward the Earth, the pitch rate is returned to normal. During the maneuver, SeaWiFS is oriented so that it scans across the lunar surface from west to east in celestial coordinates.

Because the moon appears to be a stationary object during the SeaWiFS measurements, the number of scan lines in lunar calibration depends on the pitch rate of the instrument and the apparent size of the moon. The pitch rate causes SeaWiFS to oversample the moon, resulting in approximately 26 scan lines of the moon in a typical lunar image that has a diameter of approximately 7 pixels.

For the calibration data analysis, disk-integrated spectral radiances are computed for each band from the lunar images. Prelaunch modeling of simulated lunar images showed that disk-integrated spectral radiances produce more consistent results than those computed for one or a few pixels from the center of the lunar image (Woodward et al. 1993). In this analysis, the disk-integrated radiances are summed over all pixels in the lunar image whose brightness is greater than 1% of the peak brightness in the image.

The time series of disk-integrated radiances for the first 27 lunar calibrations (spanning 798 days from 14 November 1997 through 21 January 2000) are plotted in Fig. 5. The radiances in each band have been normalized by the value at the first calibration to show the relative changes in the instrument response as functions of time. Much of the variation in these time series is due to the changing observing geometry of the individual calibrations. Normalization of the calibration data for the observing geometry will be discussed in the next section.

3.3 NORMALIZING FACTORS

Although the surface of the moon remains unchanged over the lifetime of SeaWiFS, the radiance from the moon varies with the geometry of the observations. As a result, the disk-integrated lunar radiances are normalized to a common viewing geometry for incorporation into a lunar calibration time series. These normalizing factors are

Table 5. Lunar calibration observing geometry. The notation $\boxed{\text{A}}$ indicates the calibration was after zero phase; $\boxed{\text{B}}$ indicates before zero phase. The symbol Δt_0 is the time (in days) since the first image.

Calibration	Year	Date		Δt_0	D_{SM} [AU]	$D_{\text{IM}}(R_{\text{M}})$	ϑ [degrees]	N_{M}
1	1997	14 Nov.	$\boxed{\text{A}}$	71.26	0.991602	0.939681	6.75	25.63
2		14 Dec.	$\boxed{\text{A}}$	100.83	0.986812	0.967318	7.03	25.35
3	1998	13 Jan.	$\boxed{\text{A}}$	130.39	0.986119	0.996159	5.45	24.57
4		10 Feb.	$\boxed{\text{B}}$	159.19	0.989545	1.01474	6.65	24.29
5		12 Mar.	$\boxed{\text{B}}$	188.89	0.996419	1.03299	6.72	23.62
6		12 Apr.	$\boxed{\text{A}}$	219.75	1.00516	1.03719	6.66	24.14
7		11 May	$\boxed{\text{B}}$	249.38	1.01283	1.02474	7.10	25.75
8		10 Jun.	$\boxed{\text{A}}$	278.87	1.01790	1.00304	6.43	26.19
9		10 Jul.	$\boxed{\text{A}}$	308.36	1.01919	0.975564	5.70	26.69
10		5 Sep.	$\boxed{\text{B}}$	366.31	1.01050	0.932589	6.52	27.81
11		5 Oct.	$\boxed{\text{B}}$	395.73	1.00238	0.915500	6.69	28.47
12		4 Nov.	$\boxed{\text{A}}$	425.84	0.994060	0.910064	6.55	28.16
13		4 Dec.	$\boxed{\text{A}}$	455.33	0.988037	0.920501	7.03	27.24
14	1999	2 Jan.	$\boxed{\text{A}}$	484.89	0.985745	0.942602	6.73	28.29
15		1 Feb.	$\boxed{\text{A}}$	514.38	0.987825	0.970323	4.88	26.79
16		2 Mar.	$\boxed{\text{A}}$	544.20	0.993771	1.00182	7.38	26.34
17		31 Mar.	$\boxed{\text{B}}$	572.73	1.00158	1.01719	7.01	25.65
18		1 May	$\boxed{\text{A}}$	603.38	1.01015	1.03724	6.92	25.62
19		30 May	$\boxed{\text{A}}$	633.21	1.01647	1.03694	7.95	25.46
20		29 Jun.	$\boxed{\text{A}}$	662.83	1.01928	1.02351	7.25	25.94
21		27 Jul.	$\boxed{\text{B}}$	691.21	1.01814	1.01103	6.82	26.15
22		26 Aug.	$\boxed{\text{B}}$	720.76	1.01317	0.984094	6.72	26.81
23		25 Sep.	$\boxed{\text{B}}$	750.32	1.00553	0.954810	6.83	26.78
24		24 Oct.	$\boxed{\text{B}}$	776.21	0.997086	0.929820	7.25	27.78
25		22 Nov.	$\boxed{\text{B}}$	809.28	0.989973	0.913459	6.66	27.78
26		23 Dec.	$\boxed{\text{A}}$	839.72	0.985987	0.912118	9.83	28.80
24		24 Oct.	$\boxed{\text{B}}$	776.21	0.997086	0.929820	7.25	27.78
25		22 Nov.	$\boxed{\text{B}}$	809.28	0.989973	0.913459	6.66	27.78
26		23 Dec.	$\boxed{\text{A}}$	839.72	0.985987	0.912118	9.83	28.80
27	2000	21 Jan.	$\boxed{\text{A}}$	869.13	0.986489	0.924960	8.61	29.02

based, in large part, on the positions of the spacecraft, Earth, sun, and moon computed by the SeaWiFS navigation algorithms. The observing geometries for the lunar calibrations considered in this analysis are provided in Table 5. Using these values, five normalizing factors are calculated. These normalizing factors are discussed in detail in Barnes et al. (1998 and 1999a). The implementation of these normalizing factors is discussed here.

The first normalizing factor (N_1) corrects to a common sun–moon distance and varies as $1/R^2$, where R is the distance between two bodies. The sun–moon distance (D_{SM}) is normalized to 1 Astronomical Unit (AU†):

$$N_1 = \left[\frac{D_{\text{SM}}}{\text{AU}}\right]^2. \quad (2)$$

---

† $1\,\text{AU} = 149.59787066 \times 10^6\,\text{km}$.

The second normalizing factor (N_2) corrects to a common SeaWiFS–moon distance and varies as $1/R^2$. The SeaWiFS–moon distance (D_{IM}) is normalized to the mean radius of the lunar orbit ($R_{\text{M}} = 384401\,\text{km}$):

$$N_2 = \left[\frac{D_{\text{IM}}}{R_{\text{M}}}\right]^2. \quad (3)$$

The third normalizing factor (N_3) is the illuminated fraction of the lunar surface (f_1) as a function of phase angle. This factor is a linear function of the phase angle, with the lunar surface fully illuminated at 0° phase, half illuminated at 90° phase, and dark at 180° phase. This function is given as:

$$f_1(\vartheta) = a_0 + a_1\vartheta, \quad (4)$$

where $a_0 = 1.0$ and $a_1 = -1/180$. Because the nominal phase angle of the lunar calibrations is 7°, the illuminated

area of the lunar surface is normalized to the illuminated area at 7°:

$$N_3 = \frac{f_1(7°)}{f_1(\vartheta)}$$
$$= \frac{173.0°}{180.0° - \vartheta}. \quad (5)$$

The fourth normalizing factor (N_4) compensates for the oversampling of the lunar image during the calibration. As discussed previously, the oversampling is a function of the pitch rate and the apparent size of the moon. Because the spacecraft does not have the use of its horizon sensors during the lunar pitch maneuver, there is increased noise in the pitch rate calculated from the attitude control system during the maneuver. As a result, the pitch rate is determined from the number of scan lines in the lunar image. The number of scan lines is computed from the maximum extent between the points whose brightness is 1% of the peak brightness in the image. For a given calibration, these distances are averaged over the eight bands. Because the number of scan lines in the lunar calibrations range from 23–29, these numbers are normalized to a common value of 25 scan lines. To compensate for the variation in the apparent size of the moon in the images, the number of scan lines is normalized to a common SeaWiFS–moon distance of the mean radius of the lunar orbit. The resulting normalizing factor is:

$$N_4 = \frac{25.0/N_M}{D_{IM}/R_M}, \quad (6)$$

where N_M is the mean number of scan lines in the lunar image.

The fifth normalizing factor (N_5) corrects for changes in the brightness or reflectance of the moon with phase angle. The moon has a non-uniform particulate surface with large-scale regional variations in reflectance. The nonlambertian change in the overall reflectance of the lunar surface with phase angle can be approximated by Hapke's bidirectional reflectance equation (Hapke 1986). Helfenstein and Veverka (1987) used Hapke's equation and a set of six empirically-derived constants, to provide a curve of disk-integrated reflectance versus phase angle for the moon. This curve is plotted in Fig. 6. A quadratic function has been fit to this curve to provide an interpolation between the data points (f_2). This interpolation scheme is limited to phase angles between 4° and 10°, using the function:

$$f_2(\vartheta) = b_0 + b_1\vartheta + b_2\vartheta^2, \quad (7)$$

where $b_0 = 1.2872531 \times 10^{-1}$, $b_1 = -6.7007694 \times 10^{-3}$, and $b_2 = 2.1625472 \times 10^{-4}$. The normalizing factor is computed relative to the value at 7°, the nominal phase angle of the lunar calibrations:

$$N_5 = \frac{f_2(7°)}{f_2(\vartheta)}$$
$$= \frac{0.092414408}{b_0 + b_1\vartheta + b_2\vartheta^2}, \quad (8)$$

The SeaWiFS lunar calibrations to date have occurred at phase angles of 4.8–9.8°, so the normalizing factor has been applied over a narrow range of phase. There are indications that the variation in lunar reflectance with phase angle has a wavelength dependence, which will be discussed in subsequent sections. There is also evidence that the moon is brighter before full phase than after (Kieffer and Anderson 1998). If this evidence is verified, the brightness asymmetry would have an effect of 0.5–1.0% on the value of N_5. Approximately 40% of the lunar measurements to-date were made before full phase.

The overall normalizing factor for each lunar measurement is the product of the five individual factors. This multiplicative factor is applied to the disk-integrated lunar radiances for each of the eight SeaWiFS bands. For the lunar calibrations to-date, the value of the overall normalization factor has ranged from 0.783–1.10, with a mean value of 0.924. The time series of radiances normalized to the common viewing geometry are plotted in Fig. 7.

The phase angle is the most important of the geometric angular parameters for SeaWiFS lunar measurements. The variation of the integrated lunar radiance with phase angle is much stronger than any variation with libration angle. For libration changes, the loss of visible lunar surface from one side of the moon is balanced by the gain of visible surface on the other side. For disk-integrated spectral radiances over the course of several months to several years, libration is not expected to have a major effect on the slope of the time series, but is expected to increase the scatter in the data. The overall contribution of libration to the SeaWiFS lunar time series remains unknown and is not corrected in this analysis.

3.4 PHASE ANGLE CORRECTIONS

Two trends are apparent in the plots shown in Fig. 7. The first is a systematic variation in the data from one calibration to the next that probably arises from an incomplete normalization to a common viewing geometry rather than from instrumental effects. The fact that the data for bands 1–6 track each other supports this reasoning. The second trend is a decrease in the radiometric response of bands 7 and 8 with time.

The time series can be corrected for the incomplete normalization over viewing geometry by a second normalization based on a subset of the SeaWiFS bands. Barnes et al. (1998) based this second normalization on the values for band 5, while Barnes et al. (1999a) based the normalization on the average of the values for bands 1–6. After 23 lunar calibrations, however, the consistency among these bands is less than it was for the data sets in Barnes et al. (1999a). Barnes and McClain (1999) show that bands 3 and 4 appear to be changing the least among these bands, so the mean value of these bands at each calibration is used as the second normalization of the calibration time series. The radiances with the second normalization applied are plotted in Fig. 8. Identical results are obtained
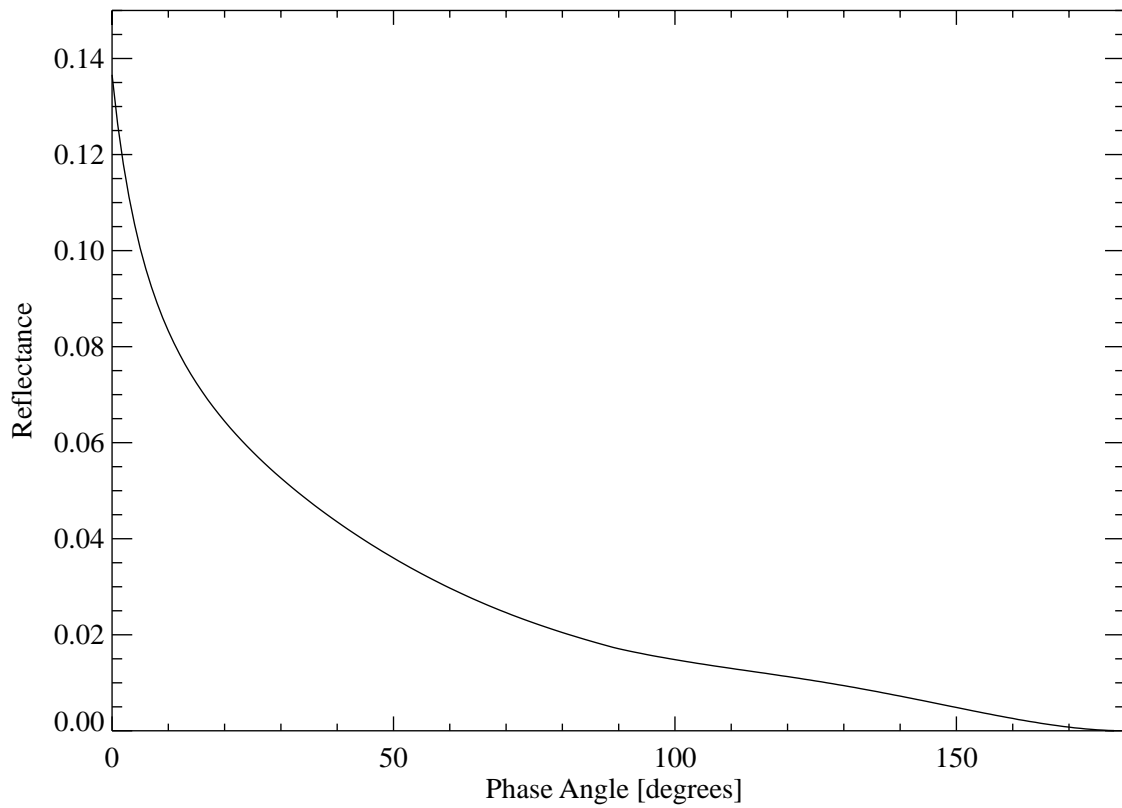
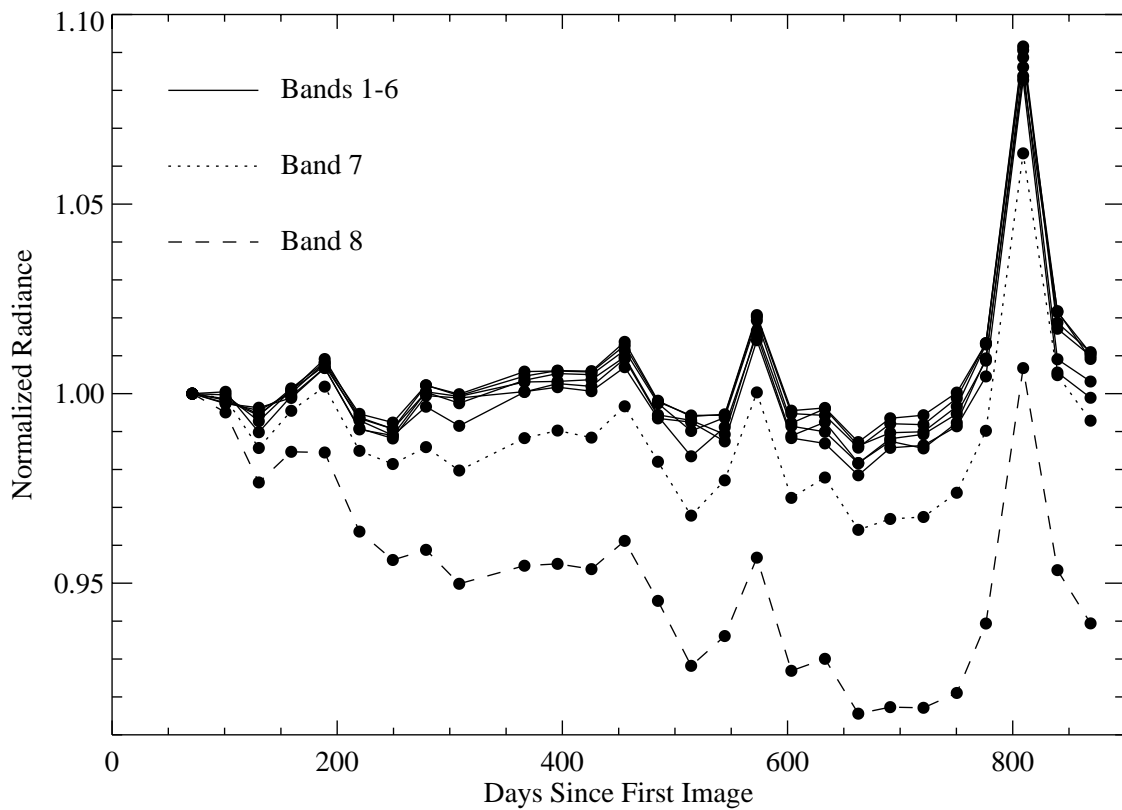**Fig. 6.** Disk-integrated reflectances versus phase angle.

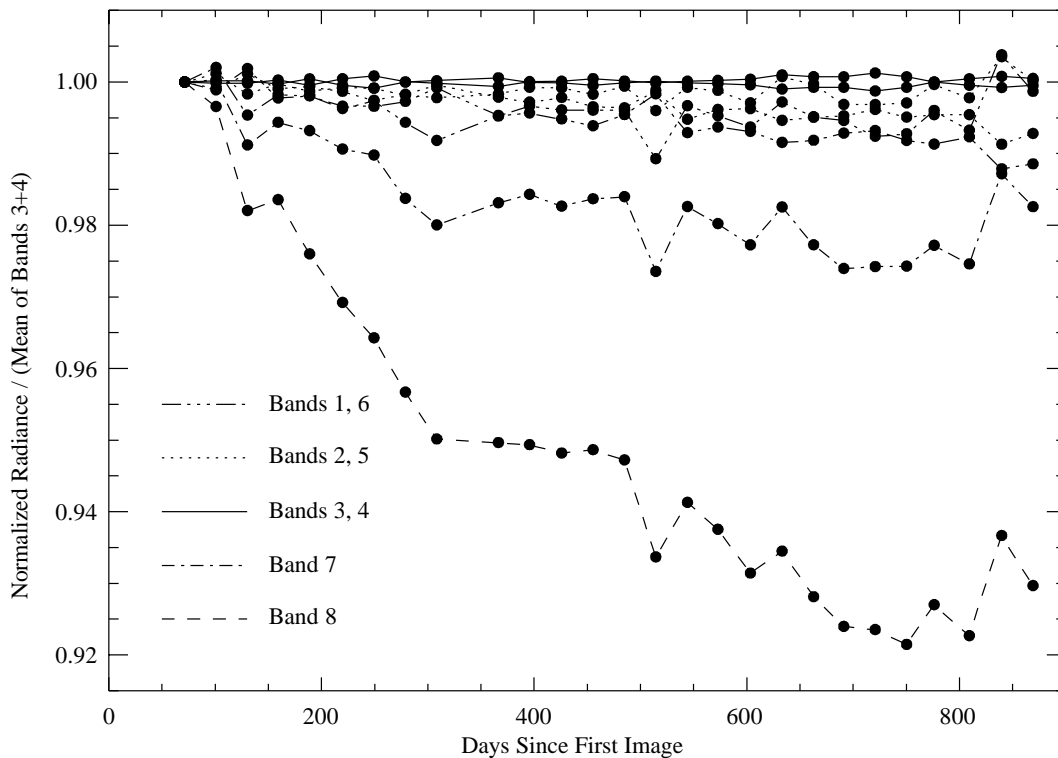**Fig. 7.** Disk-integrated lunar radiances, normalized to a common viewing geometry.

Fig. 8. Disk-integrated lunar radiances, normalized to the first calibration and the mean of bands 3 and 4.

if the disk-integrated radiances are normalized to the first observation in each band and to the mean for bands 3 and 4 for each calibration. Examining Fig. 8 shows that the radiometric responses for bands 1–6 have changed slightly over the course of the mission, while the response for band 7 is down approximately 2.5% and the response for band 8 is down approximately 8%. It should be noted that calibrations 3, 9, and 15 occurred at phase angles of less than 6° and that calibrations 19, 26, and 27 occurred at phase angles of 8° or more.

The change in lunar reflectance with phase angle from Helfenstein and Veverka (1987) is monochromatic. The measurements used as a basis for their lunar reflectance model were made at wavelengths from 360–1,060 nm (Lane and Irvine 1973). Helfenstein and Veverka (1987) used the average of those measurements (over wavelength) to create a single, best-fit lunar reflectance curve at an undefined wavelength, presumably near 500 nm. The deviations of the low and high phase angle calibrations shown in Fig. 8 appear to vary in magnitude as a function of wavelength, indicating that wavelength-dependent phase angle effects are still present in the data. Barnes and McClain (1999) derived an empirical wavelength-dependent phase angle correction from the lunar calibration data that minimizes these deviations. Barnes and McClain (1999) only used the data points for calibrations 3, 9, and 15 to compute the corrections, while the implementation described here uses all 27 calibrations to compute the corrections.

The method for calculating the correction is as follows. For each band, a regression line is calculated from the nor-

malized calibration data to determine the change in the output of the band with time. The low and high phase angle points are excluded from the calculations. Two piecewise fits are computed for each of bands 1–6: one quadratic and one linear. Three piecewise fits are computed for bands 7 and 8: two quadratic and one linear. For each band, the fractional differences between the measured calibration data points and the computed trend lines (f_3) are computed as functions of the phase angles of the measurements:

$$f_3(\lambda, \vartheta) \;=\; \frac{L_m(\lambda, \vartheta) \;-\; L_c(\lambda, \vartheta)}{L_c(\lambda, \vartheta)}, \qquad (9)$$

where L_m is the measured radiance and L_c is the computed radiance. These differences are plotted in Fig. 9, along with linear fits to the differences. The slopes of these fits, $c_1(\lambda)$, are the wavelength-dependent phase angle correction factors. Examination of the plots in Fig. 9 shows there is a correlation between the differences and the phase angles over the entire range of phase angles. This is the reason that the implementation of the wavelength-dependent phase angle correction uses all 27 calibrations in computing the correction factors.

The sixth normalizing factor (N_6) for the lunar data is computed relative to the nominal phase angle of 7°:

$$N_6 \;=\; 1.0 \;-\; c_1(\lambda)(\vartheta \;-\; 7.0°). \qquad (10)$$

The correction factors for each band are given in Table 6. Values of N_6 are typically in the range of 0.987–1.010 for
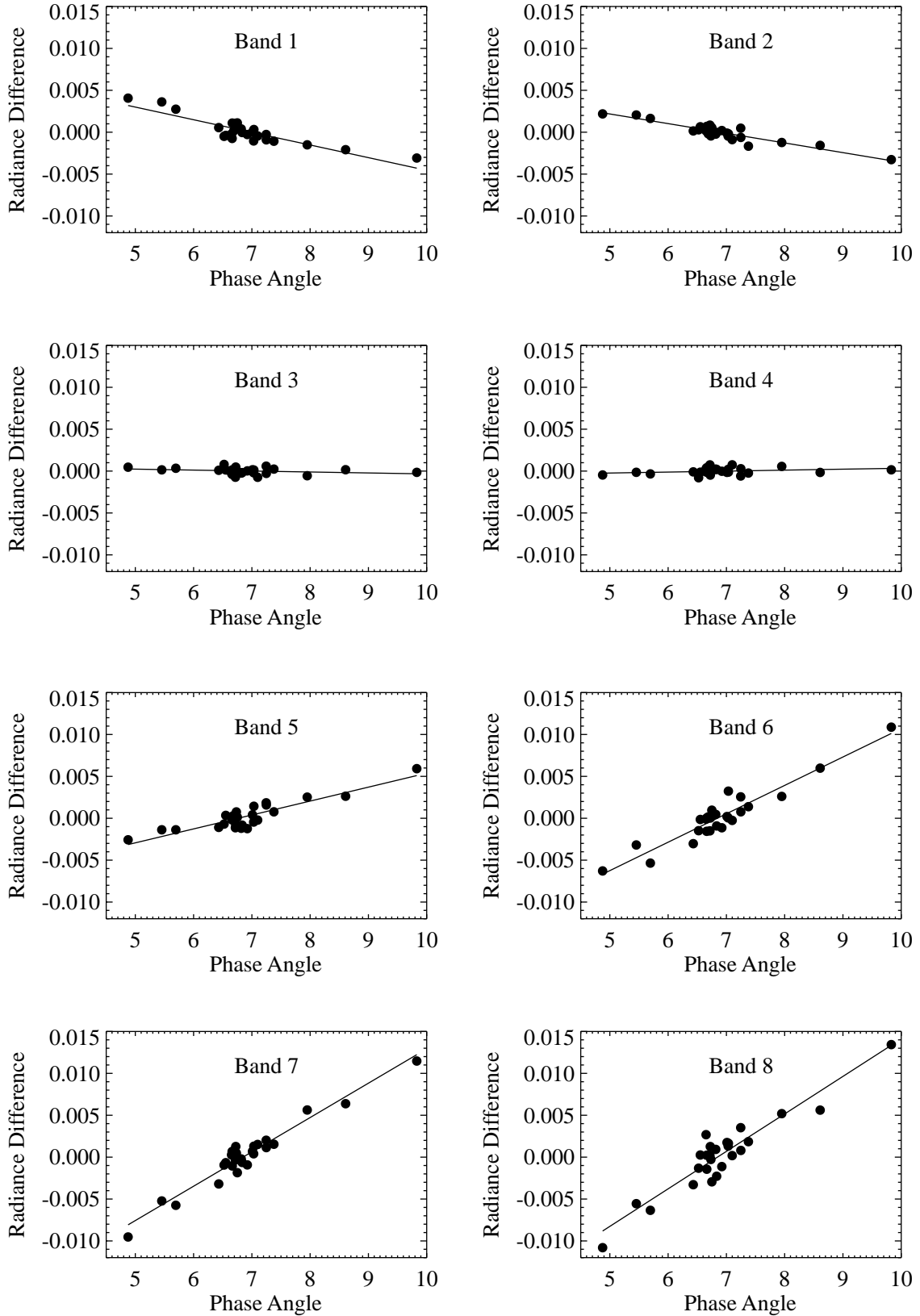
Fig. 9. Differences in measured and computed disk-integrated lunar radiances.

the observations. Because these factors are wavelength-dependent, these effects cannot be removed from the calibration data by normalizing to the mean of bands 3 and 4.

Table 6. Wavelength-dependent phase angle correction factors.

Band No.	λ [nm]	Correction Factor c_1 $(1/\vartheta)$
1	412	-0.0015091569
2	443	-0.0011531493
3	490	-0.00011397443
4	510	0.00011441961
5	555	0.0016632741
6	670	0.0033899319
7	765	0.0041000855
8	865	0.0044748836

N_6 is the final normalization applied to the lunar calibration data as part of the series of normalizations discussed in Sect. 3.3. The lunar data, with this correction applied, is then normalized by the mean values for bands 3 and 4. The resulting time series are plotted in Fig. 10. Comparing Fig. 10 with Fig. 8 shows that the wavelength-dependent phase angle correction considerably reduces the scatter in the time series. The time series for bands 1–6, with an expanded vertical scale, are plotted in Fig. 11.

3.5 LUNAR TIME CORRECTIONS

The CVT used the lunar calibration time series shown in Figs. 10 and 11 to compute time correction factors for bands 1, 2, 5, 6, 7, and 8. The group used linear and quadratic fits to the lunar measurements to compute the changes in response of those bands with time. There is no lunar calibration information prior to the first lunar calibration, which was obtained on day 71 after the first on-orbit SeaWiFS image was obtained. Consequently, the data for each band were renormalized from the plots in Figs. 10 and 11 so that the intercepts of the fits have values of unity at the time of the first image. The fits were sampled at the time of the solar calibrations to facilitate comparison of the lunar and solar calibration data.

The renormalized calibration time series for bands 1–6 are plotted in Fig. 12. For each of these bands, a single linear fit yields the best estimate of the change in response of the band with time. These fits are also plotted in Fig. 12. Bands 3 and 4 do not show any change in response over the course of the mission. The responses of the other bands are down: band 1 is down by 0.9%, band 2 is down by 0.5%, band 5 is down by 0.3%, and band 6 is down by 0.8%. Even though these changes are small, they could produce noticeable effects in the water-leaving radiances retrieved from the SeaWiFS ocean data, particularly for bands 1 and 6.

The renormalized calibration time series for all eight bands are plotted in Fig. 13. The changes in response of bands 7 and 8 can be estimated by fits of two piecewise quadratic functions and one piecewise linear function. These functions are also plotted in Fig. 13. This figure also shows the linear fits for bands 1–6. Examining Fig. 13 shows that the change in response for bands 7 and 8 is 3.4% and 9.9%, respectively, over the course of the mission.

The time correction factors for bands 1, 2, 5, 6, 7, and 8 are computed from the inverses of the fits for these bands. There is a single correction for bands 1, 2, 5, and 6 and three piecewise corrections for bands 7 and 8. The single linear corrections for bands 1, 2, 5, and 6 and the piecewise linear correction for bands 7 and 8 are used to extrapolate the time corrections for these bands in time beyond the date of the last lunar calibration. These time correction factors provide a stable radiometric response for each of the SeaWiFS bands over the course of the mission. These factors are incorporated into the SeaWiFS calibration table, which is updated as required by the on-orbit performance of the instrument.

3.6 DISCUSSION

The CVT is continuing to investigate possible causes of the change in response of the SeaWiFS bands with time. A comparison of the lunar calibration data with the solar calibration data shows that the changes in response of bands 7 and 8 appears in both the lunar and solar data sets. Figure 14 shows the ratio of band 7 to band 8 computed from the solar measurements, as derived by Eplee et al. (2000), superimposed on the ratio computed from the lunar measurements plotted in Fig. 13. The solar ratio was normalized to have the same value as the lunar ratio on day 71—the day of the first lunar calibration.

The ratio of the functions fitted to the bands 7 and 8 lunar data is also plotted in Fig. 14. The plots show that the lunar and solar data are consistent and that the piecewise functions fitted to the lunar data are consistent with the observations. The deviation of the solar ratio from the lunar ratio prior to the first lunar calibration is caused by changes that occurred in the reflectance of the solar diffuser early in the mission (Eplee et al. 2000). The agreement between the lunar band 7:8 ratio and the solar band 7:8 ratio shows that the changes in response for bands 7 and 8 arise from changes in the instrument itself, and not from artifacts in either the lunar or solar data analyses.

One scenario for the changes in response of bands 7 and 8 is as follows. The long wavelength limit for the quantum efficiency of silicon photodiodes is about 1 m. At these wavelengths, near infrared photons penetrate the surface of the material to the point that the response of the diode to short-term changes in radiant flux is compromised. It is generally believed that, over extended periods of exposure, these long wavelength photons can also cause a degradation of the diode material. Engineers at the Santa Barbara
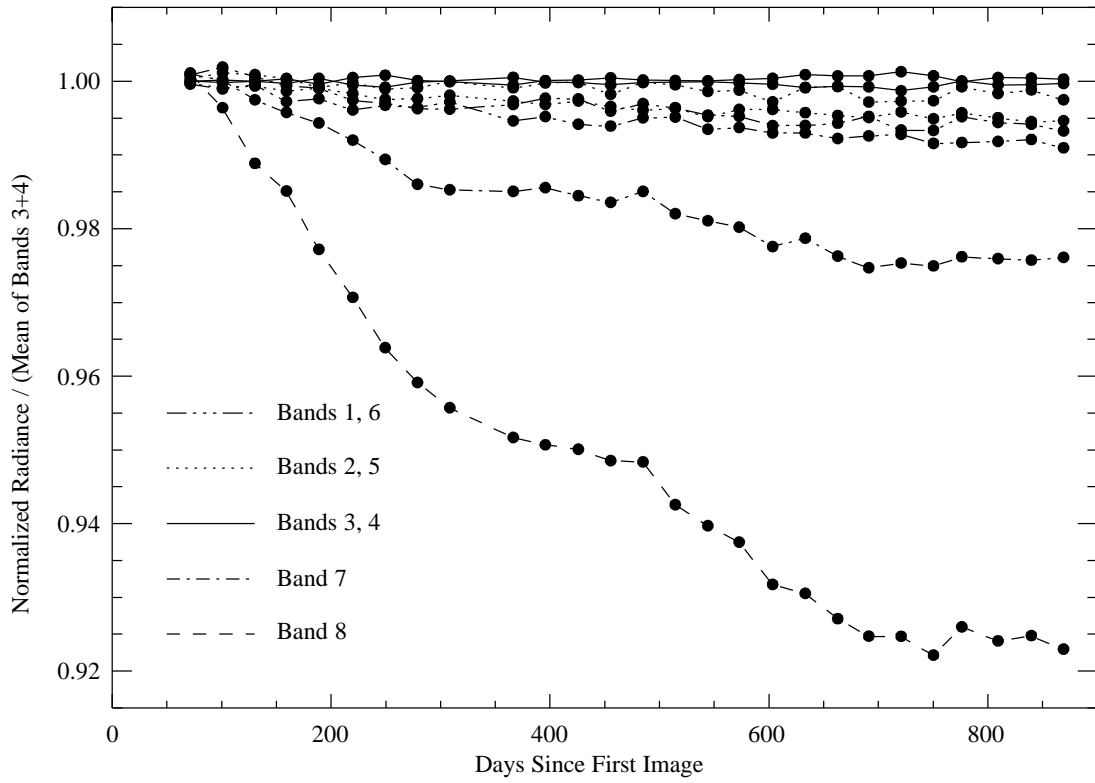
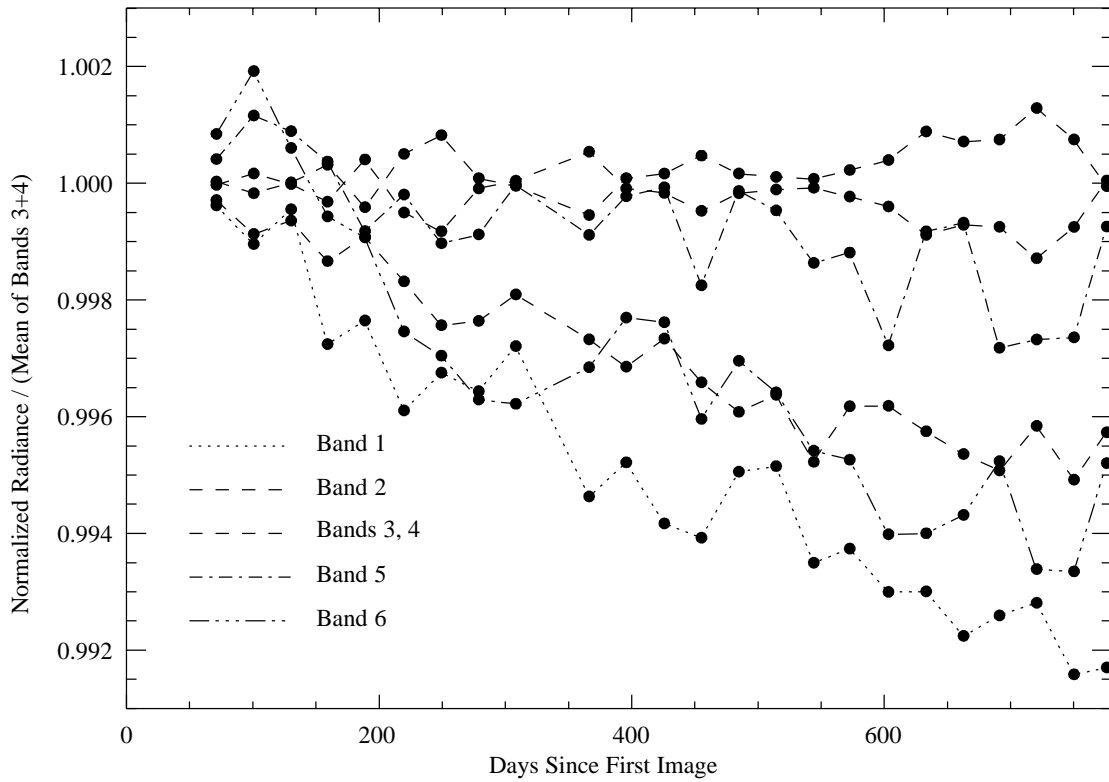**Fig. 10.** Lunar calibration time series for bands 1–8.
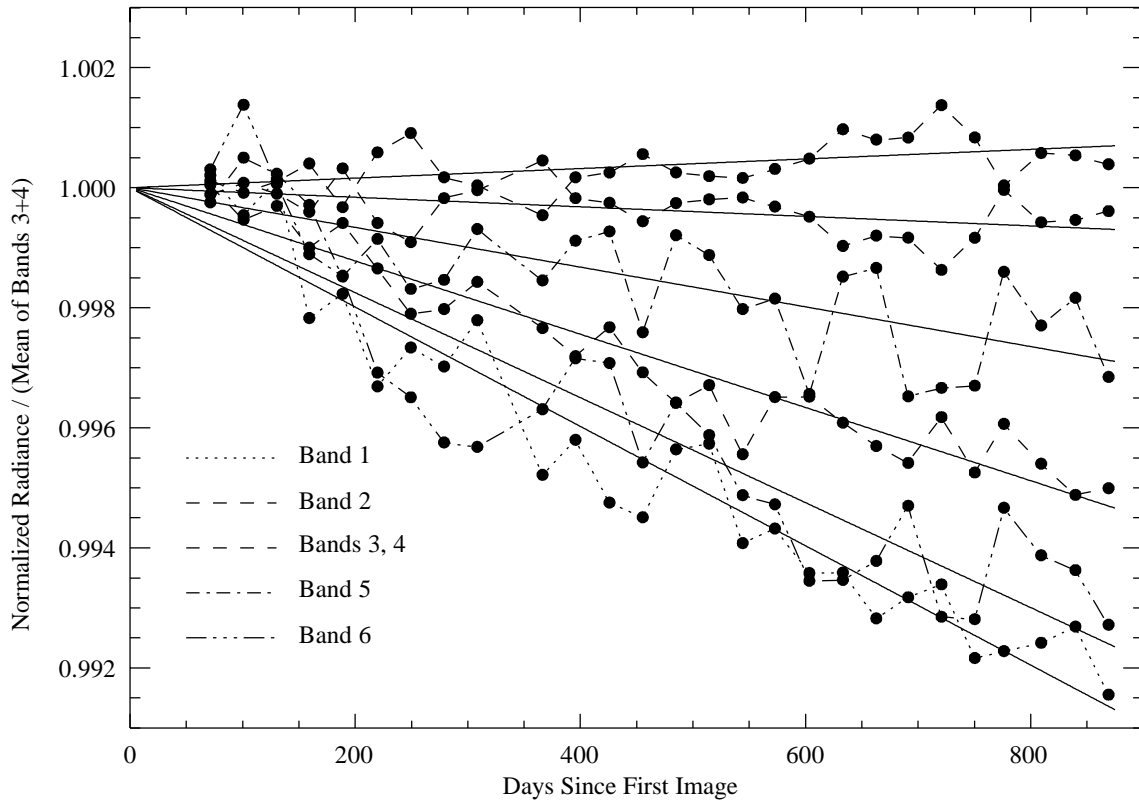

Fig. 11. Lunar calibration time series for bands 1–6.

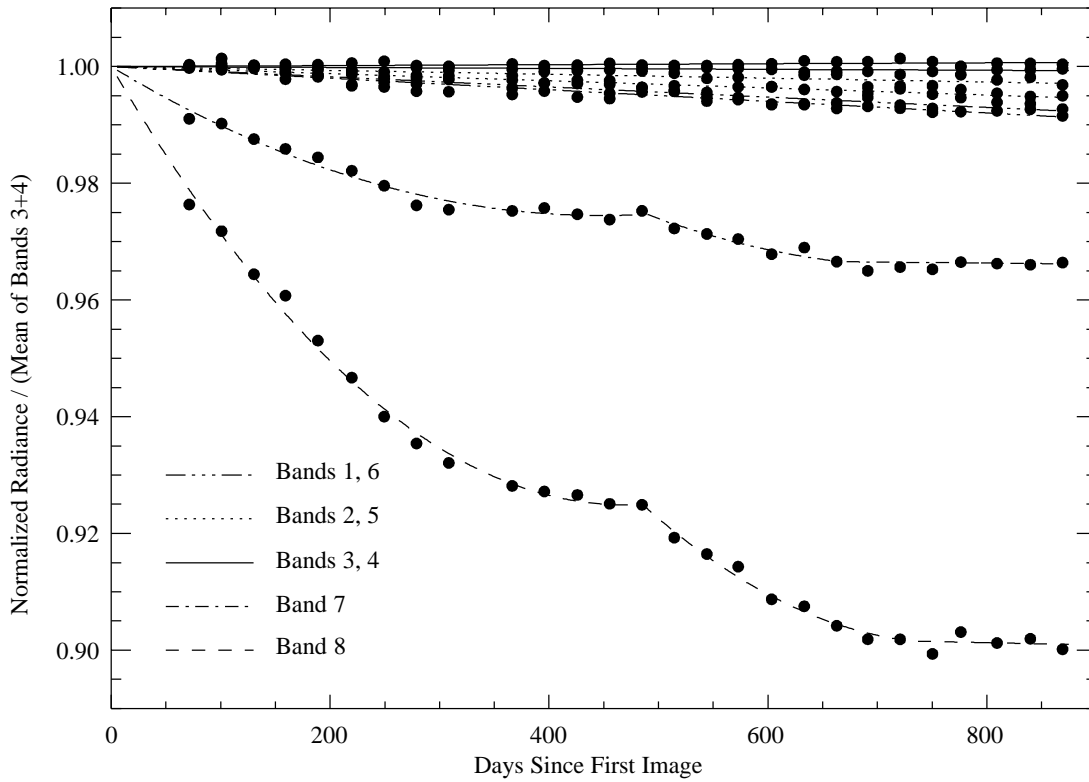**Fig. 12.** Lunar calibration time series with linear fits for bands 1–6.

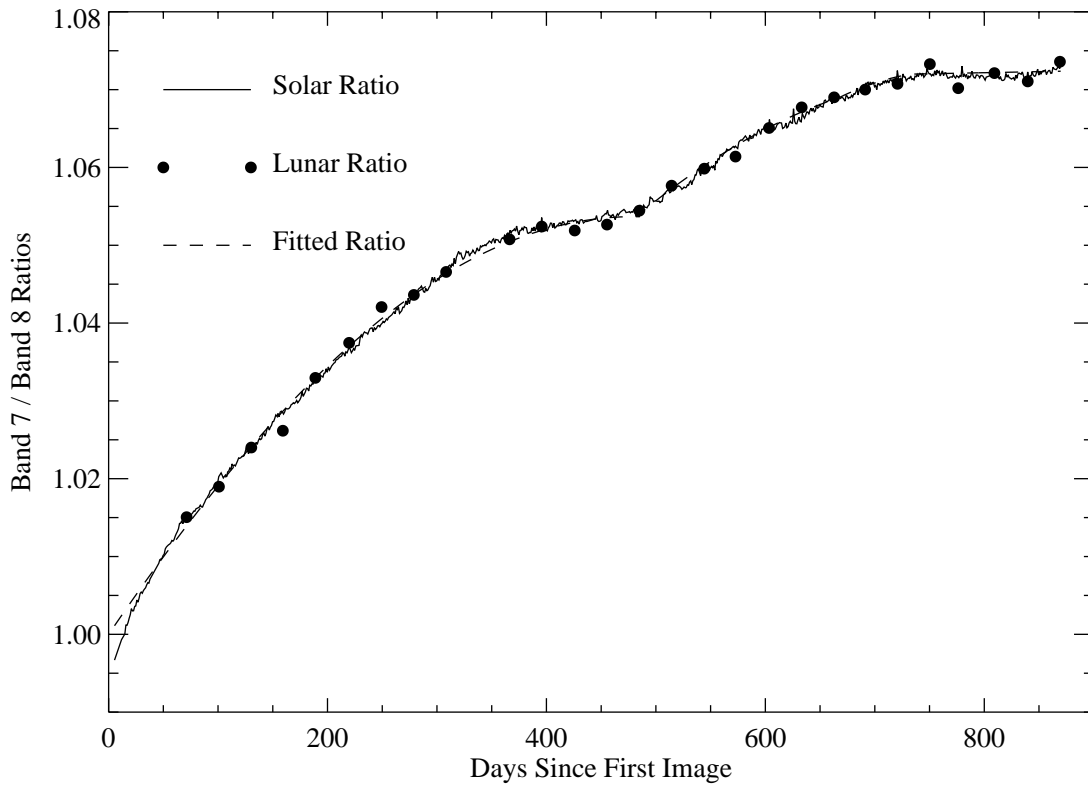**Fig. 13.** Lunar calibration time series with linear fits for bands 1–8.

Fig. 14. Lunar and solar calibration band ratios for bands 7 and 8.

Research Center, the manufacturer of SeaWiFS, call this process "annealing." The smaller change in response for bands 5 and 6 may be due to the same process, just at shorter wavelengths.

The changes in the response of bands 1 and 2 require another scenario. Eplee et al. (2000) showed that the reflectance of the SeaWiFS solar diffuser is decreasing with time, presumably due to photolyzed organic materials (outgassed from the spacecraft) condensing onto the surface of the diffuser. These materials preferentially absorb sunlight at shorter wavelengths, so the degradation of the diffuser reflectance decreases with increasing wavelength. Such yellowing of the diffuser was expected, based on experience with CZCS. The SeaWiFS primary mirror is located behind an aperture in its rotating telescope housing, so it is not exposed to space in the manner of the solar diffuser. It is possible that the effects of the yellowing of the primary mirror are just now becoming observable.

Chapter 4

Solar Data Analysis for SeaWiFS Calibration

ROBERT E. EPLEE, JR., ROBERT A. BARNES,
AND FREDERICK S. PATT
SAIC General Sciences Corporation
Beltsville, Maryland

ABSTRACT

Daily solar calibrations are used to monitor the short-term variability in the radiometric response of SeaWiFS in between the monthly lunar calibrations. The time series of solar observations show the effects of both the degradation of the reflectance of the solar diffuser and the change in response of the instrument. The ratio of the band 7 time series to the band 8 time series, which minimizes the effects of the diffuser degradation, shows that the change in response of bands 7 and 8 in the solar data tracks the change observed in the lunar data.

4.1 INTRODUCTION

The SeaWiFS CVT uses on-orbit calibration data to monitor the radiometric stability of the SeaWiFS bands over the course of the mission. Daily solar calibrations are used to track the short-term variability in the instrument response in between monthly lunar calibrations. Daily detector and gain calibrations are also used to monitor the stability of the detectors and postdetector electronics within SeaWiFS. Preliminary solar data analysis results were previously discussed by Barnes et al. (1999a). This chapter describes how the solar, detector, and gain calibration data plus corresponding analysis techniques are used to monitor the performance of SeaWiFS on orbit.

4.2 SOLAR CALIBRATIONS

Solar calibrations are performed once per day when the spacecraft is over the South Pole. At this time, the rotation of the spacecraft causes the sun to rise and set over the solar diffuser aperture in the direction of the pitch of the spacecraft. The observations record sunlight reflected by the uniformly illuminated diffuser. For each solar calibration, the mean radiance is computed for all 8 bands over 3 pixels and 250 scan lines centered on the image of the illuminated diffuser. As the sun changes position in the sky over the course of a year, the incidence angle of the solar image on the diffuser changes in the direction that is perpendicular to the direction of the pitch. This is called the "azimuth angle" in the nomenclature of the SeaWiFS diffuser (Barnes and Eplee 1996). The azimuthal angles for the SeaWiFS solar measurements vary over a range of $-5°$ to $6°$ over the course of a year. The mean solar radiances are normalized to a common Earth–sun distance of one Astronomical Unit and are corrected for the seasonal variations in the azimuthal angle of the incident sunlight on the diffuser.

4.3 AZIMUTHAL CORRECTIONS

Ideally, the bidirectional reflectance distribution function (BRDF) of the diffuser would be used to correct for the seasonal cycle in the azimuthal angle of the sunlight. The BRDF for the SeaWiFS diffuser, however, was only determined for bands 4 and 8 under a limited set of viewing angles (Barnes and Eplee 1996). Barnes et al. (1999a) fitted the band 8 BRDF data to a second order polynomial curve with a value of unity at zero azimuth and a value of about 0.95 at $6°$ on each side of zero to compute an azimuthal angle correction for the solar data. The laboratory measurements are incomplete, and the analysis presented in this chapter underscores the importance of a detailed characterization of the diffuser's BRDF before launch.

An alternative approach for correcting the variation in the solar azimuthal angle on the diffuser has been developed and applied to the solar calibration data. This approach assumes that the BRDF of the SeaWiFS diffuser is 10% of the BRDF of a perfect lambertian diffuser (Barnes and Eplee 1996) and incorporates the cosine of the azimuthal angle. The wavelength dependence of the solar diffuser (f_4) BRDF is approximated by a rotation in azimuth as a function of wavelength. The resulting correction factors are:

$$f_4 = \frac{1.0}{1.0 - (1.0 - \cos(\varphi + \psi))/R_B}, \quad (11)$$

where: φ is the azimuthal angle of incident sunlight on the diffuser; ψ is the angle of rotation in azimuth, which is

a function of wavelength; and R_B is the ratio of SeaWiFS BRDF to lambertian BRDF, which equals 0.1 (Barnes and Eplee 1996). The rotation angles for the SeaWiFS bands, which have been empirically determined to minimize the residual seasonal variations in the solar calibration data, are listed in Table 7.

Table 7. Band-specific rotation angles for azimuthal angle correction.

λ	*Rotation Angle* [degrees]
412	0.8
443	0.7
490	0.7
510	0.7
555	0.6
670	0.5
765	0.3
865	0.0

With the addition of the wavelength-dependent rotation angles, the azimuthal angle corrections defined by (11) are mathematically equivalent to the polynomial fits employed by Barnes et al. (1999a). These adjustments are smaller than the 2° spacing of the measurements used to create the polynomial curve, and they are based on the assumption of small alignment differences for measurements of the diffuser.

4.4 CALIBRATION TIME SERIES

The time series for the first 821 solar calibrations (spanning 864 days from 10 September 1997 through 22 January 2000) are plotted in Fig. 15. These data have been normalized to a common Earth–sun distance of 1 AU, but have not been corrected for the variation in the solar azimuthal angle. The radiances in each band have been normalized by the value at the first calibration to show the relative changes in the diffuser reflectance as functions of time. The time series of solar azimuthal angles, due to the seasonal variation in the position of the sun in the sky, is plotted in Fig. 16. The azimuthal angle corrections for the eight bands, computed using (11), are plotted in Fig. 17. These corrections have been applied to the solar calibration data plotted in Fig. 18.

Two trends are apparent in the time series shown in Fig. 18. The first is a degradation in the reflectance of the diffuser with time as photolyzed organic materials (outgassed from the spacecraft) condense onto the surface of the diffuser. These materials preferentially absorb sunlight at shorter wavelengths, so the degradation of the diffuser reflectance decreases with increasing wavelength. Because the correction for the variation in solar azimuthal angle on the diffuser is approximate, part of the change in diffuser reflectance with wavelength could be a residual BRDF effect. The second trend apparent in the data is the changes

in radiometric responses with time for bands 7 and 8 (discussed in detail in Eplee and Barnes 2000). The time series do not show any short-term variability in the response of the SeaWiFS bands.

Because the SeaWiFS atmospheric correction algorithm uses the ratio of radiances in band 7 to the radiances in band 8 for computing the aerosol radiance, and because the degradation in the diffuser reflectance decreases with wavelength, the ratios of the solar data for band pairs have been plotted (Fig. 19). These plots have also been normalized to the value of unity at the first calibration. Comparing the band pair ratios implies that if there were no degradation in the response of bands 7 and 8, the band 7:8 ratio should approach unity. The trend in the band 7:8 ratio evident in the plot arises from the change in the response of the two bands.

The solar and lunar calibration time series for bands 7 and 8 are plotted simultaneously in Fig. 20. Comparing the solar and lunar data for the two bands provides an estimate of the degradation of the diffuser reflectance that is independent of wavelength.

Figure 21 shows the ratios of solar data for bands 7 and 8 superimposed on the ratio from the lunar calibration data (Eplee and Barnes 2000). The solar ratio has been normalized to have the same value as the lunar ratio on day 71, the day of the first lunar calibration. The plots show that the solar and lunar data are consistent and that the degradation in the responses of bands 7 and 8 is not an artifact of the solar diffuser or of the degradation in the diffuser reflectance. The plots also show that the corrections for the variation in the azimuthal angle (f_4) for bands 7 and 8 yields data that are consistent with observations which are independent of the solar diffuser.

Time correction factors have been computed for bands 1, 2, 5, 6, 7, and 8 from the lunar calibration data (Eplee and Barnes 2000). These correction factors are applied to the solar calibration data plotted in Fig. 22 and to the solar calibration band ratios plotted in Fig. 23. The time series in Fig. 23 shows that the time corrections for bands 7 and 8 are stable to within 0.2% over the course of the mission.

4.5 DETECTOR CALIBRATIONS

Detector calibrations are performed once per day, typically two orbits after the solar calibration, using a variation of the solar calibration procedure. During the detector calibrations, observations of the illuminated solar diffuser are collected individually for the four detectors in each band. Figure 24 shows the time series of the detector calibrations for band 7, and Fig. 25 shows the time series of detector calibrations for band 8. These plots show that the changes in response of the individual detectors in bands 7 and 8 are consistent and track the drifts of the bands as a whole. The changes in response of bands 7 and 8 are not due to changes in individual detectors within either band.
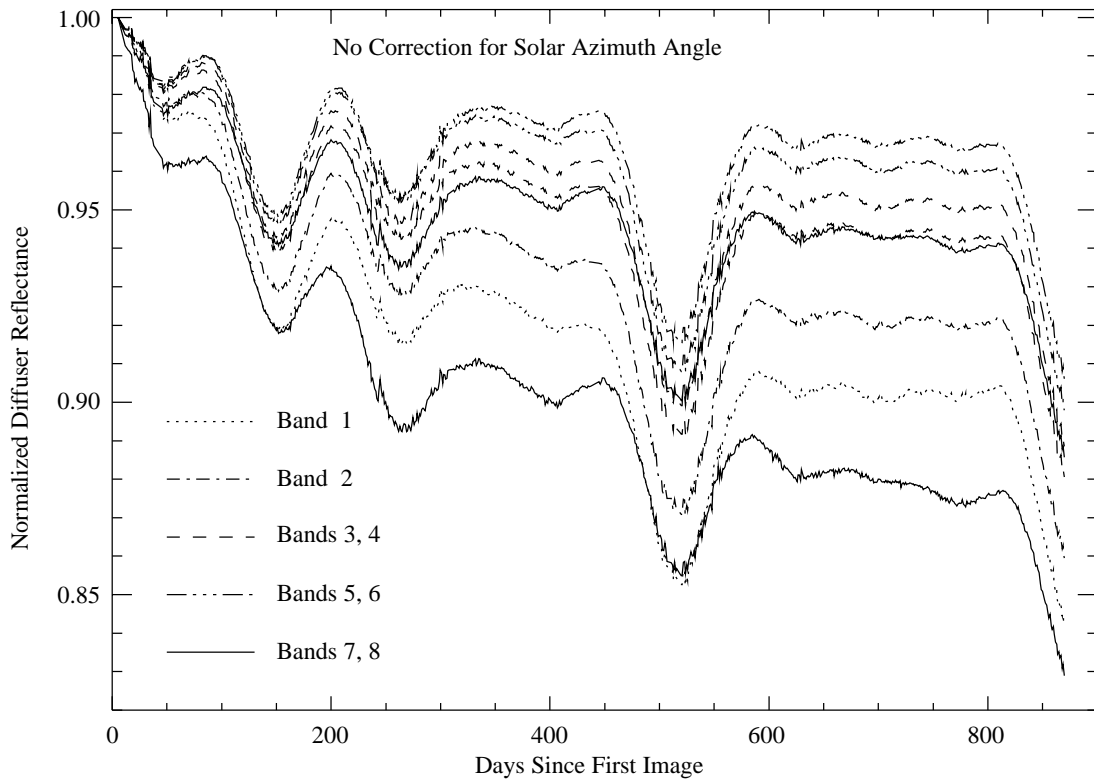
Fig. 15. Solar calibration diffuser reflectances.
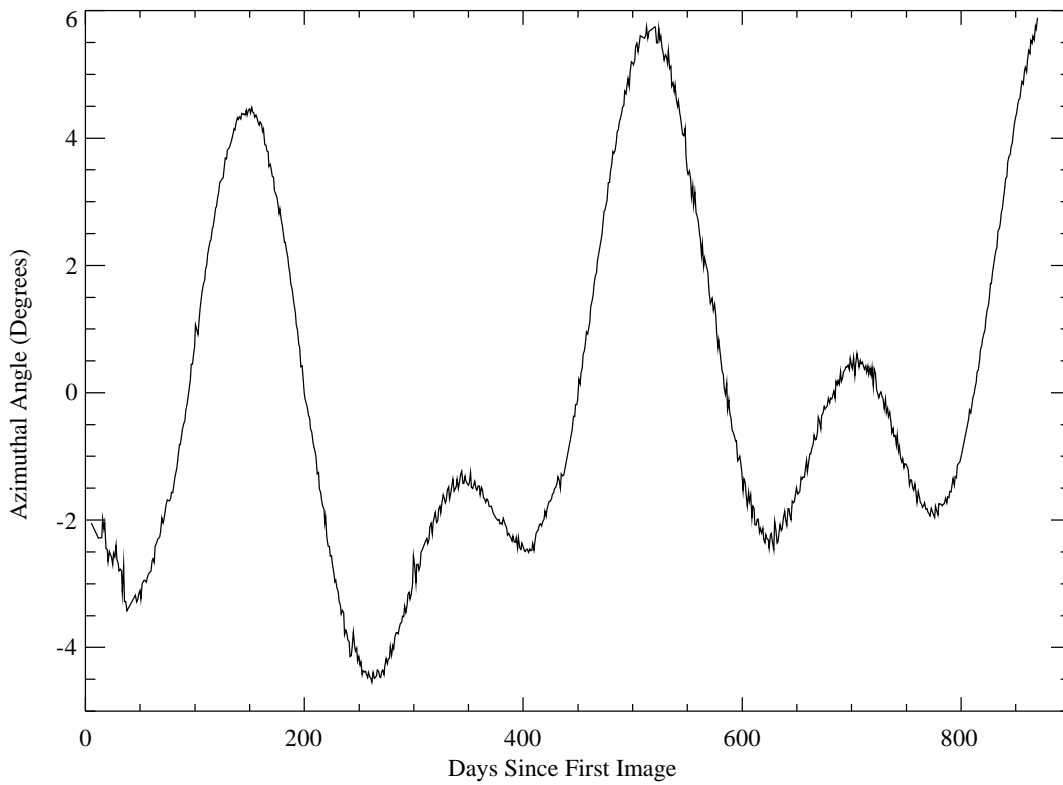

Fig. 16. Azimuthal angles of the image of the sun on the solar diffuser.

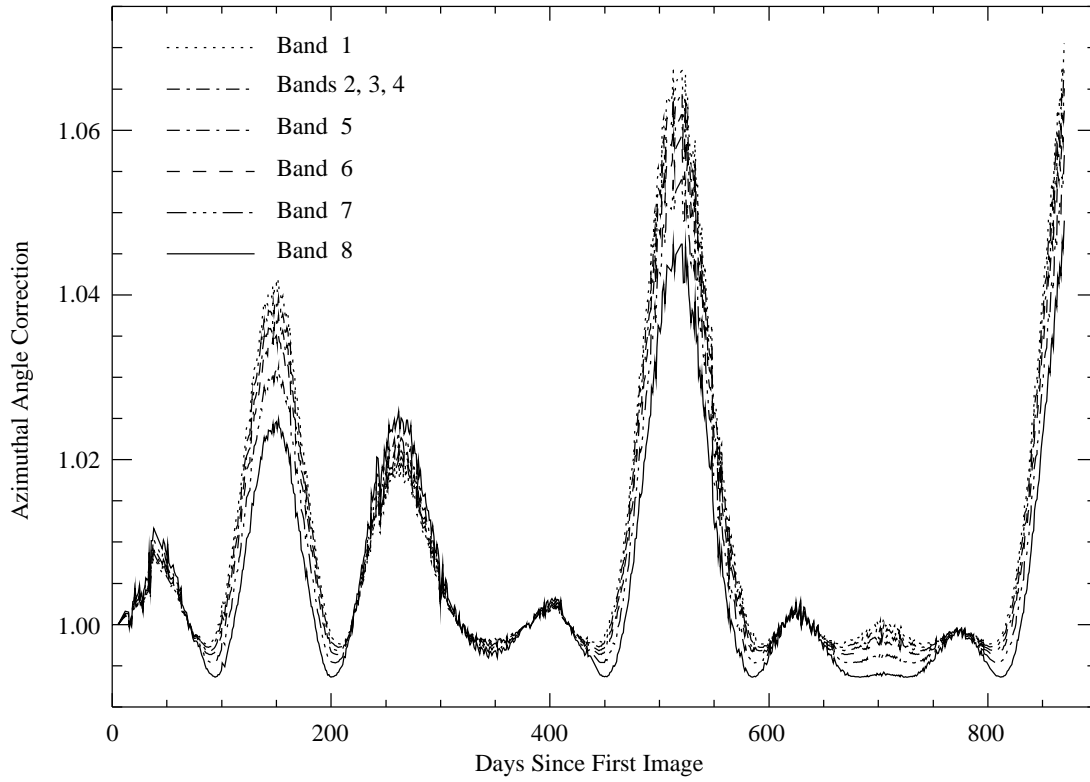**Fig. 17.** Solar azimuthal angle correction factors.
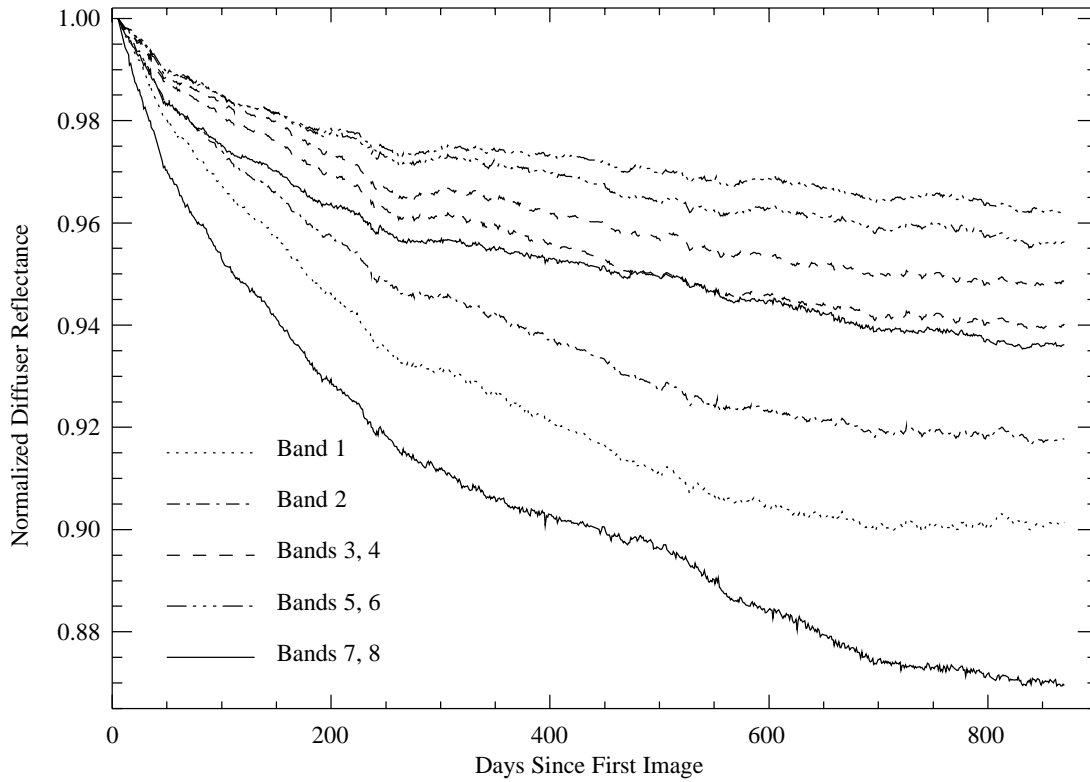
Fig. 18. Solar calibration diffuser reflectances, corrected for azimuthal angles.

Fig. 19. Solar calibration band ratios.

Fig. 20. Solar and lunar calibration time series for bands 7 and 8.

Fig. 21. Solar and lunar calibration band ratios for bands 7 and 8.

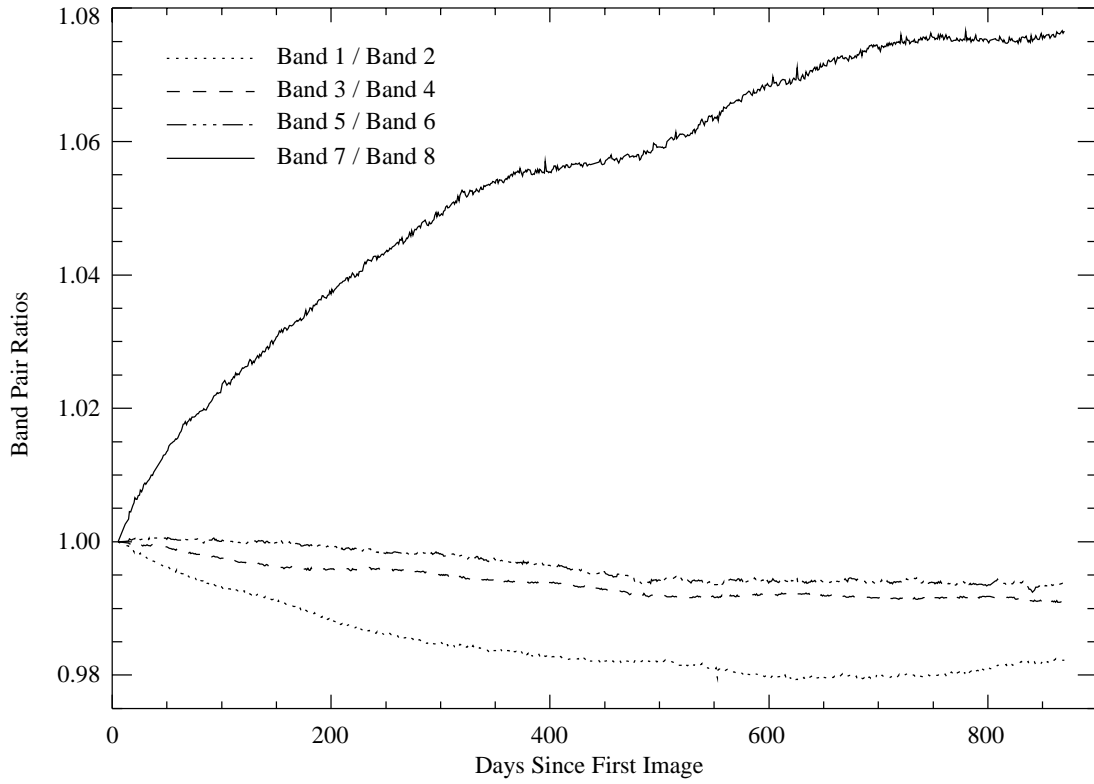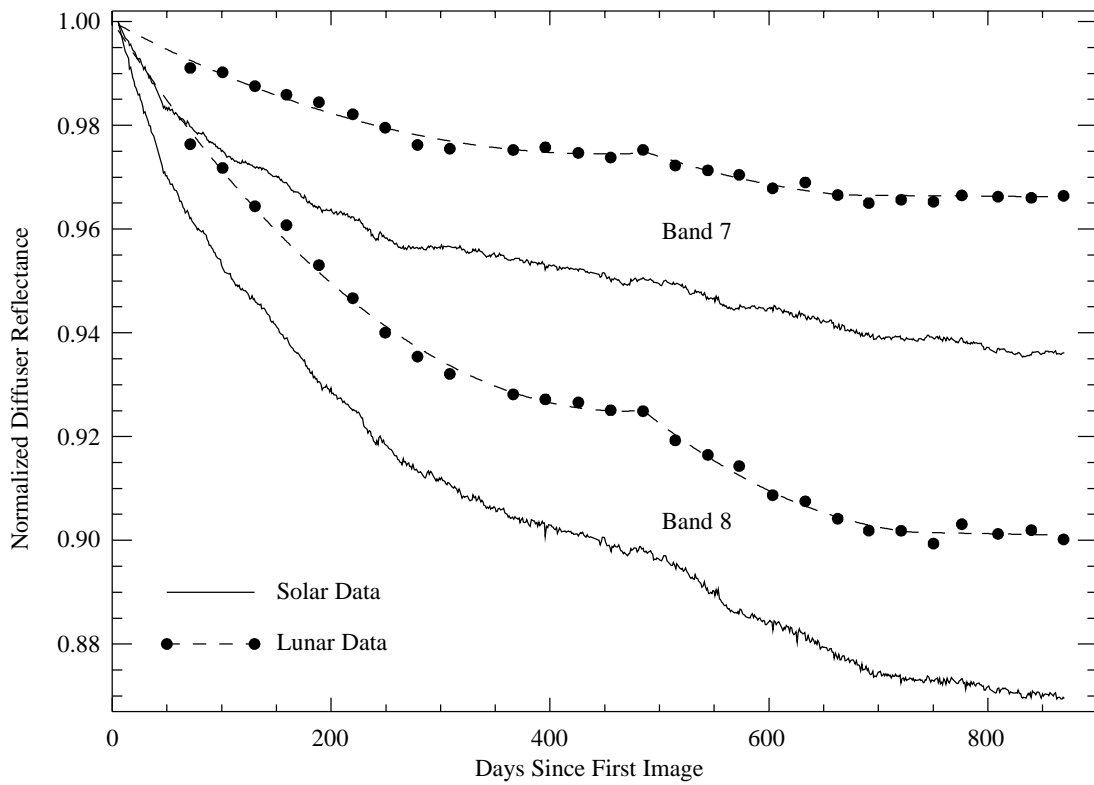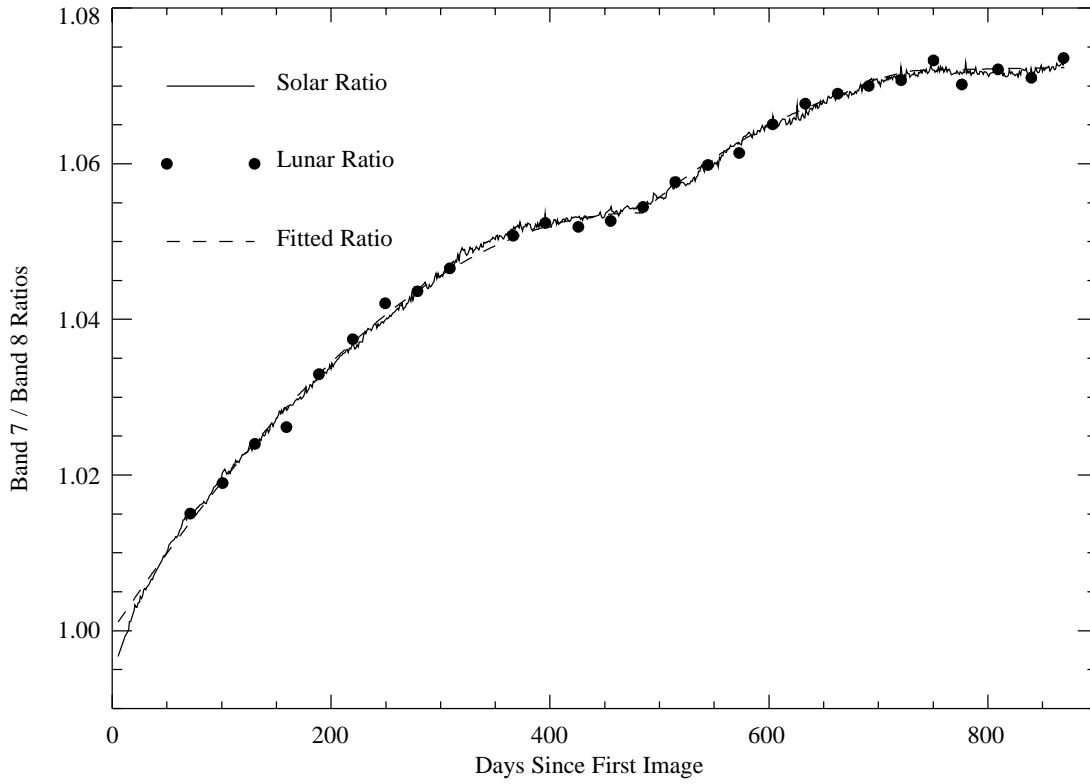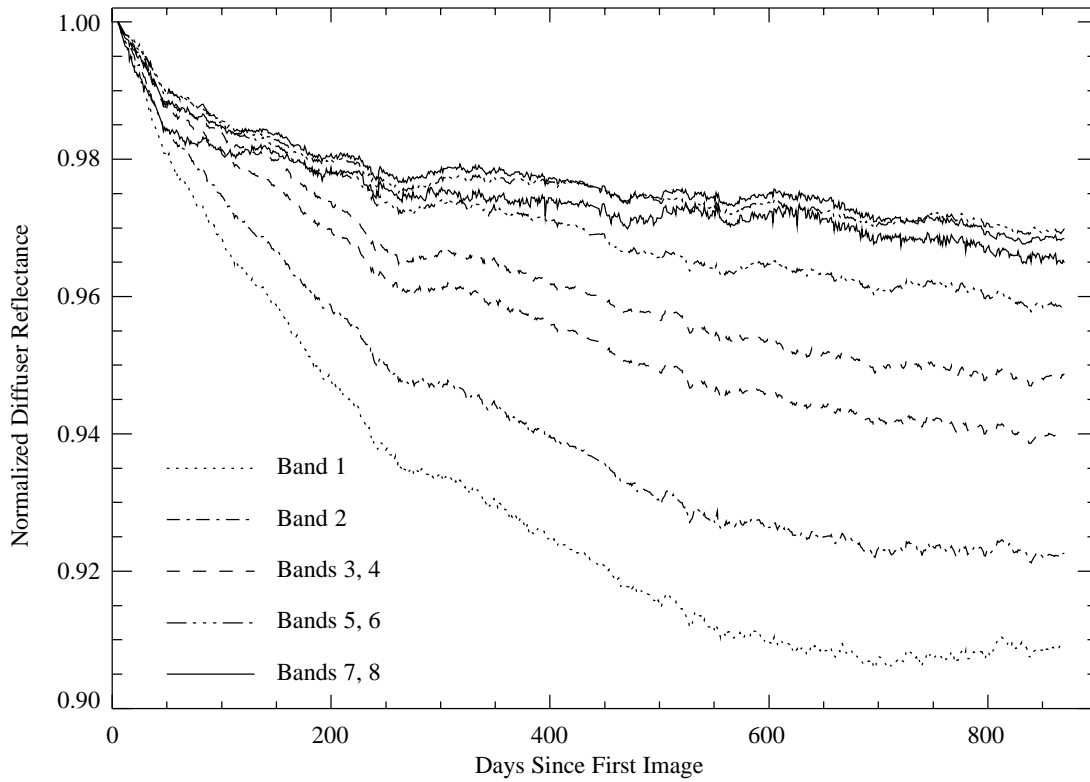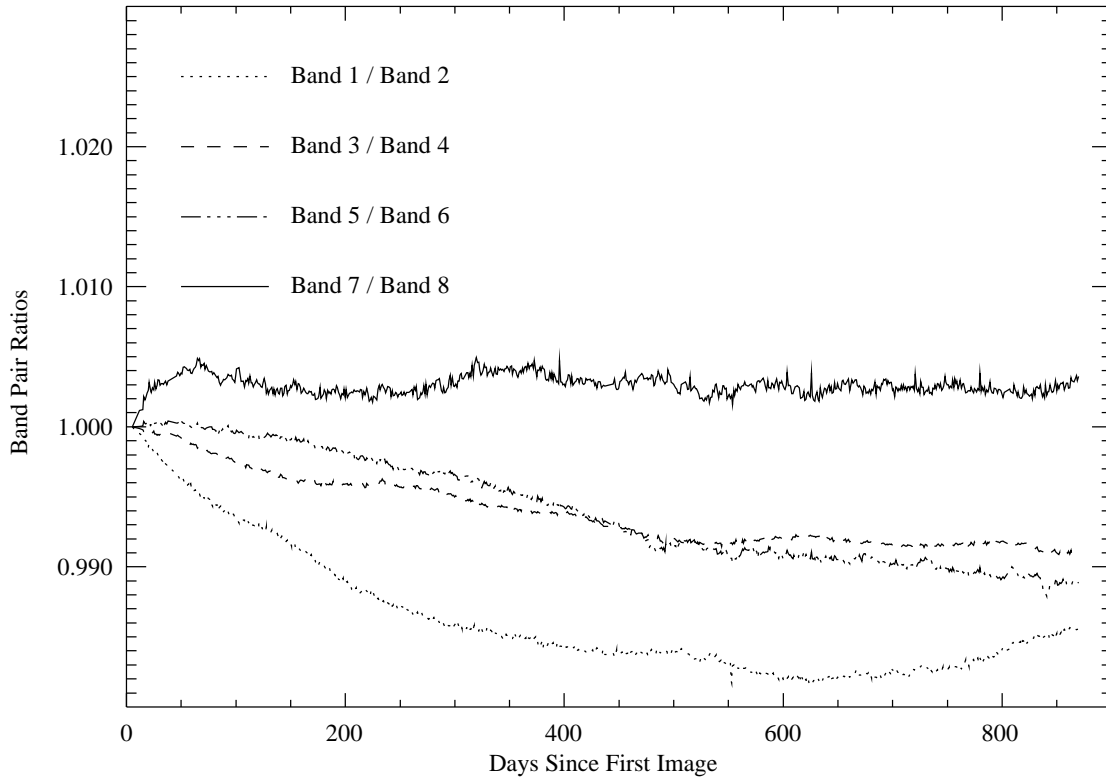**Fig. 22.** Solar calibration diffuser reflectances with time corrections applied.

Fig. 23. Solar calibration band ratios with time corrections applied.
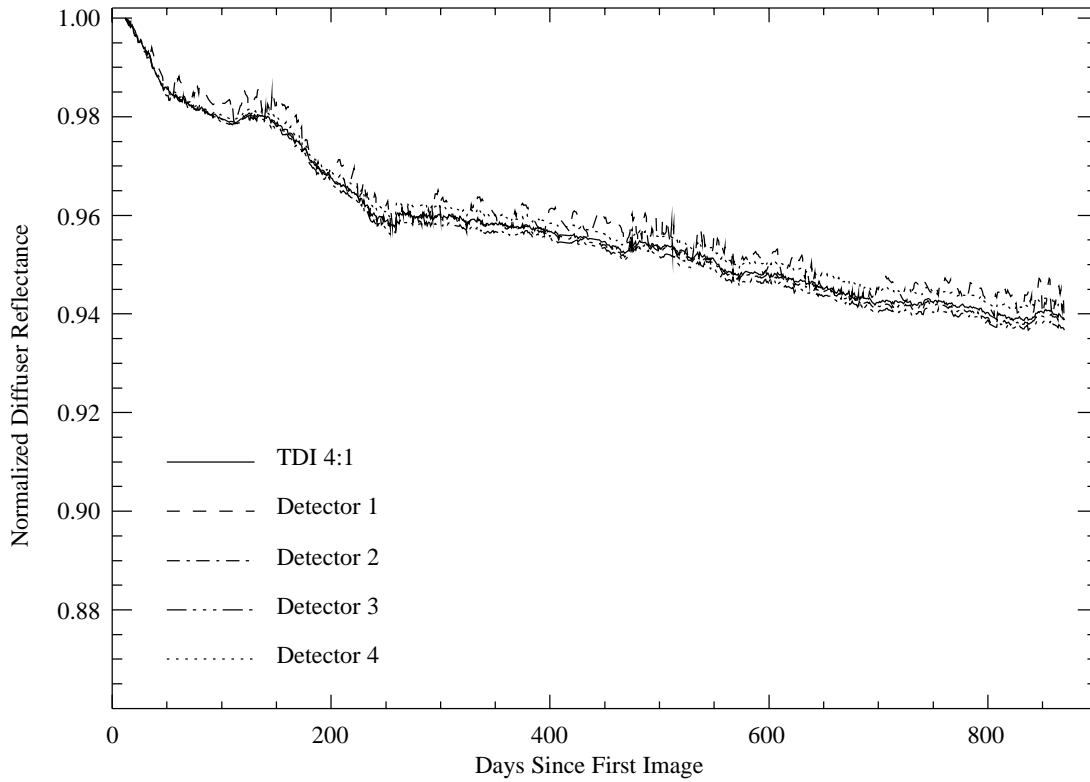

Fig. 24. Detector calibration time series for band 7.

Table 8. SeaWiFS prelaunch gains relative to Gain 1.

Band No.	Detector No.	Gain 1	Gain 2	Gain 3	Gain 4
1	1	1.00000	1.01562	1.00506	1.01046
	2	1.00000	1.98647	1.32275	1.68180
	3	1.00000	1.98621	1.32010	1.68059
	4	1.00000	1.99245	1.31944	1.67965
2	1	1.00000	1.99157	1.31919	1.68193
	2	1.00000	1.98408	1.31888	1.68100
	3	1.00000	1.98892	1.31722	1.68275
	4	1.00000	1.02419	1.00806	1.01613
3	1	1.00000	1.05087	0.999861	1.03091
	2	1.00000	1.98867	0.894868	1.68113
	3	1.00000	1.98857	0.896848	1.68113
	4	1.00000	1.99015	0.895656	1.67992
4	1	1.00000	1.99007	0.786856	1.68143
	2	1.00000	1.98781	0.788264	1.68176
	3	1.00000	1.98821	0.788229	1.68360
	4	1.00000	1.04348	0.985507	1.02899
5	1	1.00000	1.04412	0.985294	1.02941
	2	1.00000	1.99080	0.641401	1.59637
	3	1.00000	1.98940	0.643069	1.59636
	4	1.00000	1.98948	0.641937	1.59425
6	1	1.00000	1.99099	0.362975	0.662879
	2	1.00000	1.98762	0.364917	0.665017
	3	1.00000	1.99050	0.364214	0.665150
	4	1.00000	1.03333	0.966673	0.979392
7	1	1.00000	1.04918	0.966610	0.968238
	2	1.00000	1.98794	0.310052	0.575541
	3	1.00000	1.98864	0.312990	0.575752
	4	1.00000	1.99055	0.310930	0.576902
8	1	1.00000	1.99170	0.260256	0.498881
	2	1.00000	1.98912	0.261251	0.499517
	3	1.00000	1.99130	0.259961	0.498223
	4	1.00000	1.04110	0.958904	0.972603

Table 9. SeaWiFS on-orbit gains relative to Gain 1.

Band No.	Detector No.	Gain 1	Gain 2	Gain 3	Gain 4
1	1	1.00000	1.01384	1.00474	1.01070
	2	1.00000	1.98483	1.32261	1.68071
	3	1.00000	1.98667	1.31367	1.67983
	4	1.00000	1.99250	1.31748	1.67960
2	1	1.00000	1.99404	1.31923	1.67573
	2	1.00000	1.98330	1.31885	1.68066
	3	1.00000	1.99005	1.31212	1.68243
	4	1.00000	1.02201	1.00803	1.01613

Table 9. (cont.) SeaWiFS on-orbit gains relative to Gain 1.

Band No.	Detector No.	Gain 1	Gain 2	Gain 3	Gain 4
3	1	1.00000	1.04317	0.999249	1.02541
	2	1.00000	1.96727	0.895505	1.68115
	3	1.00000	1.99016	0.893043	1.68186
	4	1.00000	1.99132	0.896420	1.68058
4	1	1.00000	1.99264	0.787118	1.67559
	2	1.00000	1.98548	0.787691	1.68128
	3	1.00000	1.98929	0.785179	1.68326
	4	1.00000	1.04064	0.985578	1.02899
5	1	1.00000	1.03909	0.984992	1.02914
	2	1.00000	1.98856	0.642293	1.59672
	3	1.00000	1.99075	0.640013	1.59658
	4	1.00000	1.99070	0.643690	1.59483
6	1	1.00000	1.99330	0.363494	0.666026
	2	1.00000	1.98551	0.365785	0.668350
	3	1.00000	1.99166	0.362301	0.665366
	4	1.00000	1.03082	0.966881	0.980609
7	1	1.00000	1.04439	0.955551	0.967513
	2	1.00000	1.98649	0.311277	0.579590
	3	1.00000	1.98952	0.311649	0.575681
	4	1.00000	1.99139	0.314473	0.576669
8	1	1.00000	1.99373	0.260326	0.503102
	2	1.00000	1.98696	0.262634	0.503937
	3	1.00000	1.99227	0.258170	0.498930
	4	1.00000	1.03832	0.959105	0.972930
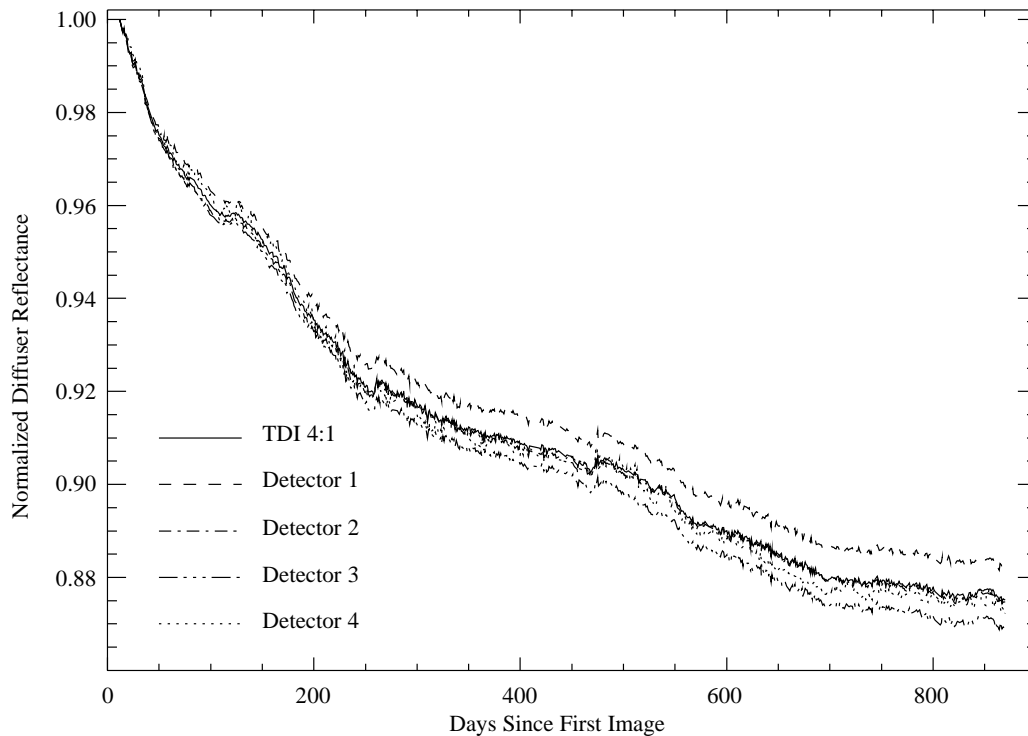
Fig. 25. Detector calibration time series for band 8.

4.6 GAIN CALIBRATIONS

Gain calibrations are performed once per day, typically immediately following the solar calibrations, and are used to track the stability of the four gains of each detector in all eight bands. During the calibration, a square-wave electronic pulse is applied to the postdetector electronics during a portion of the SeaWiFS scan when the detectors are not illuminated. The gain of the detectors is varied over the duration of the pulse. The ratios of the output from the detectors at each gain, relative to the output for the unity gain, are the gain ratios. The gain ratios, computed from the on-orbit calibration pulse data, have been stable over the course of the mission and are consistent with the ratios measured during the prelaunch instrument recalibration (Johnson et al. 1999). The prelaunch ratios are shown in Table 8 and the on-orbit ratios are shown in Table 9. A comparison of the two shows the gain ratios are stable to within 0.1%, which eliminates the postdetector electronics as a cause for changes in the response of bands 7 and 8.

4.7 DISCUSSION

Despite the degradation of the solar diffuser reflectance with time, the SeaWiFS solar calibration data show the same changes in radiometric responses of bands 7 and 8 that were first observed in the lunar calibration data. This change in response is not caused by any artifacts in the solar data analysis. The solar data show no short-term variations in the response of the SeaWiFS bands between lunar calibrations. Because of the degradation of the diffuser reflectance, the small drifts in the response of bands 1, 2, 5, and 6, which were observed in the lunar data, are not visible in the solar data.

The analyses of the on-orbit detector and gain calibration data imply that the source of the changes in the radiometric response of bands 7 and 8 is found either prior to the detectors in the optical path of the instrument, or it is the result of a change that occurs simultaneously to all four detectors in each band.

Chapter 5

Vicarious Calibration of SeaWiFS Band 7

Wayne D. Robinson
SAIC General Sciences Corporation
Beltsville, Maryland

Menghua Wang
University of Maryland Baltimore County
Baltimore, Maryland

Abstract

A technique for vicariously calibrating the gain in the SeaWiFS band 7 is described in this chapter, as well as the details of its implementation. The technique has been found to provide a consistent estimate of the gain over the life of the SeaWiFS Project.

5.1 INTRODUCTION

This chapter describes the current method used to vicariously determine the gain factor to apply to the band 7 SeaWiFS radiances. Because of their negligible water-leaving radiance components, band 7, at 765 nm, is used in combination with band 8 at 865 nm to determine the aerosol optical properties of the air column (Gordon and Wang 1994b), from which the aerosol radiances in the remainder of the SeaWiFS bands can be deduced. Determining the band 7 gain properly is important so that all the other bands can be calibrated and used properly.

The problem of vicarious calibration of ocean color sensors was discussed by Gordon (1998), who proposed the following requirements for achieving a good calibration:

1. The calibration should be made in a cloud-free air mass with a maritime aerosol having an optical thickness of less than 0.1, and

2. The water-leaving radiances must be uniform over the area in question.

In the case of band 7 (and 8), these requirements should be easily met, as long as highly turbid or high chlorophyll concentration waters are avoided and clear areas are selected. Many of the quantities that need to be measured to properly perform the calibration are available in the form of SeaWiFS radiances and ancillary data. Specific knowledge of the aerosol type is not available, but this uncertainty is reduced by using a region where the aerosol properties are well known.

Section 5.2 investigates the theory behind the calibration of band 7, Sect. 5.3 examines the validity of assuming band 8 has the correct calibration, and Sect. 5.4 discusses the technique for evaluating the gain in more detail, using the measurements available to the SeaWiFS Project. The results and conclusions of these analyses are presented in Sects. 5.5 and 5.6.

5.2 THEORY

Gordon and Wang (1994a) derived a value, ϵ, based on the single scattering aerosol reflectance, ρ_{as}:

$$\epsilon(\lambda, 865) = \frac{\rho_{as}(\lambda)}{\rho_{as}(865)}, \qquad (12)$$

which is a constant for any one type of aerosol atmosphere. Computations of ϵ have been made for a variety of aerosol types including oceanic, maritime, coastal, and tropospheric, and at a variety of relative humidities: 50, 70, 90, and 99%. SeaWiFS bands 7 and 8 were chosen so that the $\epsilon(765, 865)$ could be computed. The equation for upwelling radiance through a clear atmosphere over the ocean at the top of the atmosphere (TOA) is:

$$\begin{aligned} L_t(\lambda) = {} & L_r(\lambda) + L_a(\lambda) + L_{ra}(\lambda) \\ & + T(\lambda) L_g(\lambda) + t(\lambda) L_f(\lambda) \\ & + t(\lambda) L_W(\lambda), \end{aligned} \qquad (13)$$

where $L_t(\lambda)$ is the total upwelling radiance, $L_r(\lambda)$ is the Rayleigh radiance, $L_a(\lambda)$ is the radiance arising from aerosol scattering, $L_{ra}(\lambda)$ is the radiance arising from the interaction of molecular and aerosol scattering, $T(\lambda)L_g(\lambda)$ is the glint radiance arising from the specular reflection of the sun off the water surface, $t(\lambda)L_f(\lambda)$ is the radiance from foam (or whitecaps), and $t(\lambda)L_W(\lambda)$ is the water-leaving

radiance. Note that $T(\lambda)$ is the direct transmittance and $t(\lambda)$ is the diffuse transmittance of the atmosphere. $L_r(\lambda)$ can be determined accurately with a knowledge of the surface pressure (Gordon et al. 1988). Areas where the sun glint is significant can be predicted and avoided by viewing away from the point of specular reflection. The whitecap radiance can be well estimated at low wind speeds (Gordon and Wang 1994b) and can be avoided at higher wind speeds as the wind field is an available product. $L_W(\lambda)$ at the 765 and 865 nm bands of SeaWiFS can be considered to be zero in nonturbid, low chlorophyll waters; thus, (13) can be simplified for bands 7 and 8 to:

$$L_t(\lambda) - L_r(\lambda) - t(\lambda)L_f(\lambda) = L_a(\lambda) + L_{ra}(\lambda). \quad (14)$$

Gordon and Wang (1994a) determined a relationship between the $L_a(\lambda) + L_{ra}(\lambda)$ terms and the single scattering radiance, $L_{as}(\lambda)$, for the aforementioned aerosol models; thus, because $L_r(\lambda)$ and $t(\lambda)L_f(\lambda)$ are known, the total radiance for bands 7 and 8 can be used in (12) to derive ϵ.

Over open ocean areas, it can be assumed that a maritime aerosol is usually present and, thus, such a site has a known ϵ value. For sites like this, it is then possible to determine the gain in band 7 through a process of adjusting the gain until (12) produces a maritime ϵ value.

5.3 BAND 8 ACCURACY

The basic method described in Sect. 5.2 can be applied to SeaWiFS observations to determine the gain for band 7. Before this method is described, a tacit assumption is made that the gain in band 8 is already correct, but if it is not, the band 7 gain can absorb any small offsets in the band 8 gain. In fact, band 8 does have a laboratory calibration (Johnson et al. 1999) and should be reasonably close to the correct value (Barnes et al. 1999b); however, the calibration can change as a result of the stresses associated with launch. Also, the calibration being performed is not strictly an absolute calibration, but a vicarious calibration which includes a calibration of the sensor and the processing algorithms as a whole. Studies of the errors introduced by gain errors (Gordon 1998, Wang and Franz 2000) indicate that this assumption introduces only minor errors. An analysis of the error introduced in the band 7 calibration due to an incorrect band 8 calibration is presented here.

If the single-scattering approximation is used, the ϵ value used in the band 7 gain calculation can be expressed as:

$$\epsilon(765, 865) \approx \frac{[L_t(765)\,G_7 - L_r(765)]\,F_0(865)}{[L_t(865)\,G_8 - L_r(865)]\,F_0(765)}, \quad (15)$$

where G_7 and G_8 are the gain factors for bands 7 and 8, and $F_0(\lambda)$ is the solar irradiance. Assuming that the band

7 gain can compensate for any errors in the band 8 gain, then (15) can be rewritten as

$$\epsilon(765, 865) = \frac{[L_t(765)\,G_{7:8} - L_r(765)]\,F_0(865)}{[L_t(865) - L_r(865)]\,F_0(765)}, \quad (16)$$

where $G_{7:8}$ is the combined gain used as the band 7 gain in this analysis. If $L_r(\lambda)$ is small, then

$$G_{7:8} = \frac{G_7}{G_8}, \quad (17)$$

and the assumption would work perfectly; however, $L_r(\lambda)$ is significant relative to $L_t(\lambda)$.

By converting (15) into the form of (16), the actual value of $G_{7:8}$ is seen to be:

$$G_{7:8} = G_7\,h + \frac{L_r(765)}{L_t(765)}\,(1 - h), \quad (18)$$

where h is a shorthand notation for

$$h = \frac{L_t(865) - L_r(865)}{L_t(865)\,G_8 - L_r(865)}. \quad (19)$$

The actual value of $G_{7:8}$ is not of interest, but the amount of variation, specifically, the standard deviation in $G_{7:8}$, i.e., $\sigma(G_{7:8})$, for the normal range of SeaWiFS data is important. This would indicate the error to be expected in the gain applied to band 7 for an average SeaWiFS pixel.

$G_{7:8}$ was evaluated for a typical GAC pass of data using a nominal band 7 gain (G_7) of 0.95, and values of G_8 ranging from 0.95–1.05 , i.e., band 8 gain changes of from -5% to $+5\%$. For the 11,778 pixels that could be processed to get L_{WN} data, the $\sigma(G_{7:8})$ is shown in Table 10.

Table 10. Error in the band 7 gain. Column 1 is the actual gain in band 8 for which a gain of 1 is assumed. Column 2 is the error in the band 7 gain expected (i.e., an extra source of noise) and is a result of assuming the band 8 gain is 1.

G_8	$\sigma(G_{7:8})$
0.95	0.00205
0.98	0.00179
0.99	0.00091
1.01	0.00094
1.02	0.00191
1.05	0.00489

The error in the present estimate of band 7 gain is 0.008 (Sect. 5.5), so unless the error in the band 8 gain is large, 5% or more, this error is probably acceptable at this time. If the gain in band 8 needs to be changed, tests indicate that a 3% increase (or decrease) in the band 8 gain requires a corresponding band 7 increase (or decrease) of 2.2% to get the same ϵ value.
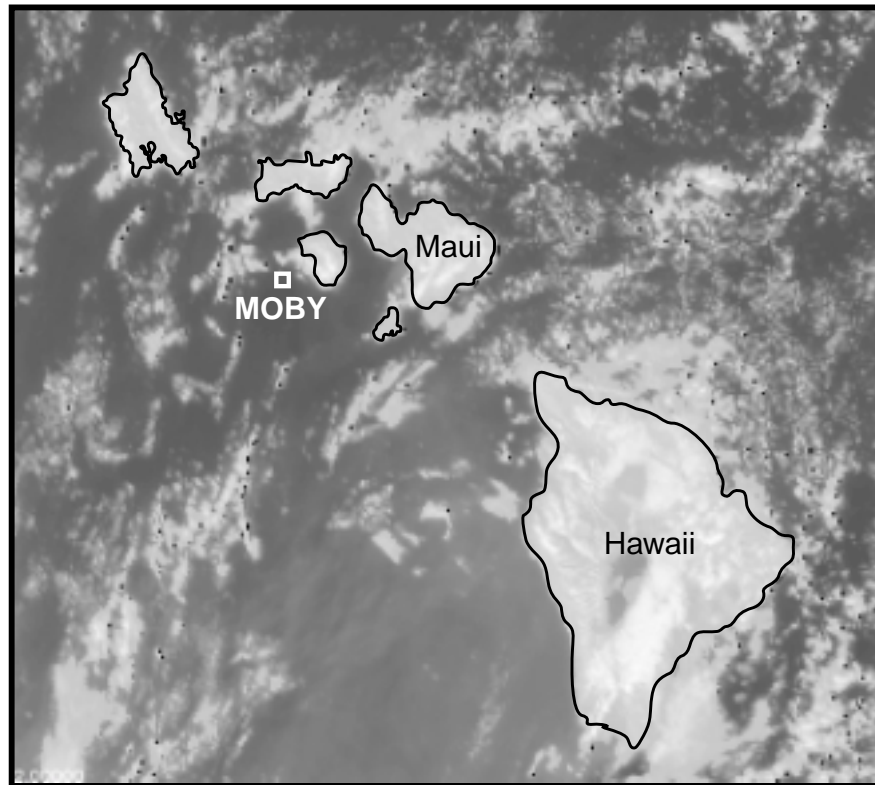
Fig. 26. An image of the Hawaiian Islands showing the location of the MOBY site used to derive the band 7 gain. The islands of Hawaii, Maui, Molokai, Lanai, and Oahu are visible in the image with a black outline of their coasts. The white box shows the 3×3 pixel area centered on the MOBY location at 20.828°N and 157.19°W.

5.4 CALIBRATION METHOD

This study was conducted with SeaWiFS data taken at the MOBY site located west of the Hawaiian island of Lanai (Fig. 26). The site is in the open ocean and has a consistent maritime aerosol type. This region was also chosen because it has had good coverage by the full, 1 km resolution LAC data throughout the mission and it coincides with the area where the vicarious calibration of the other bands is done (Eplee and McClain 2000).

The choice of the MOBY site allowed the use of 724 LAC data sets for the study. Such a large number makes it possible to be more selective of the atmospheric conditions in each observation and still retain a large sample of observations. The site was chosen to have a square area of 3×3 LAC pixels, which are averaged together to determine the ϵ value for that observation. The ϵ values found in good pixels are averaged and then matched against the expected maritime ϵ value. The gain in band 7 that produces this ϵ value is the gain determined for that observation.

Although the region for this study was selected to have a constant maritime aerosol value, this still leaves four maritime models to choose from with varying humidity conditions. If there was a measure of the aerosol value at the site, the exact maritime model could be determined. The humidity is available in the ancillary data but there may be little correspondence between the actual humidity and the aerosol model based on that humidity. So, in this study, the ϵ value used for the site is the average of the ϵ values from the four maritime models.

The computation of ϵ is performed by running the Sea-WiFS operational level-2 program. Some changes are made in the standard flagging controls to ensure that only very clear sites are used. First, the cloud albedo threshold is changed from 1.1 to 0.9 so that more stringent cloud screening is used to ensure the selection of cloud-free pixels. The following pixel exclusion conditions are also added: a satellite zenith angle limit of 56°, a solar zenith angle limit of 70°, and a mask of pixels containing excessive stray light. Also note that the calibration table used in the processing has had the time dependence in bands 7 and 8 removed (Eplee and Barnes 2000). The result of the level-2 processing is a 3×3 field of ϵ values and other parameters. The unmasked parameter values are averaged to produce an observation for that site and data set. The averaged ϵ value is used to match the four-model maritime ϵ value.

Additional screening tests are applied to the observations. Observations are considered only if more than five of the points remained unmasked. This screen is designed so that a relatively large clear region is used for each observation and to reduce the effects of noise by averaging a number of LAC pixel values of ϵ. Tests were run to see
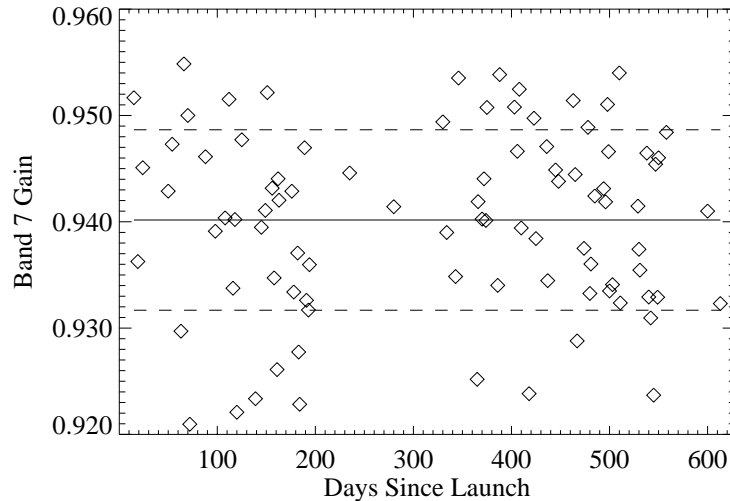
Fig. 27. The gain in band 7 plotted as a function of the number of days since the start of SeaWiFS operations on 4 September 1997. The solid line is at the mean gain 7 value and the dashed lines are 1σ away from the mean.
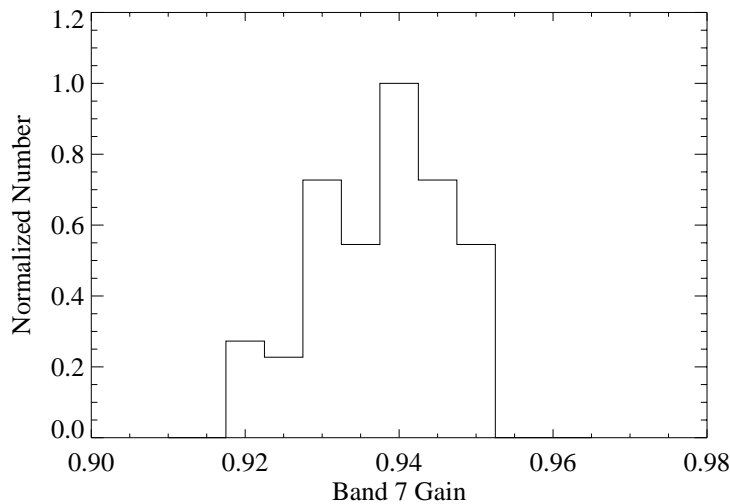

Fig. 28. A histogram of the distribution of band 7 gain at the MOBY site.

if a requirement of 100% of the points would reduce the error in the band 7 gain; it did not, instead however, it significantly reduced the number of usable observations.

In the processing, the effect of whitecap radiance is accounted for using a relationship between the wind speed and the whitecap radiance (Gordon and Wang 1994a). The data used to derive this relationship shows a wide variance as the wind speed increases. In addition, during some tests, it was found that there may be a weak correlation between wind speed and the band 7 gain. Considering this, another screen is imposed on the observations that keeps only the observations where the wind speed is less than $8\,\mathrm{m\,s^{-1}}$.

The clear air screening was improved using the criteria of Gordon (1998) on the aerosol optical thickness. Only observations having an aerosol optical thickness less than

0.1 are used to determine the band 7 gain. A low limit of 0.03 is also imposed on all of the observations. A final screen is imposed on the observations to remove any statistically bad observations. The standard deviation of the band 7 gain is derived for the remaining observations and any observations that are more than 2σ away from the mean are discarded.

5.5 RESULTS

The technique described above is applied to available SeaWiFS LAC data using the operational level-2 processing program. Figure 27 is a plot of the band 7 gain determined for the MOBY site as a function of the number of days since SeaWiFS became operational. Out of

the 724 LAC data sets covering the Hawaii area, 89 data sets satisfy the screening tests; the mean band 7 gain is 0.940 ±0.008. The error in the band 7 gain of less than 1% translates into errors in the normalized water-leaving radiance in the other bands of well below 10% (Gordon 1998). This assumes that there is no vicarious calibration of the other bands. The vicarious calibration should compensate for any possible gain 7 errors. Figure 28 shows the histograms of the band 7 gain at the MOBY site.

5.6 CONCLUSIONS

A technique for calibrating the gain in SeaWiFS band 7 was derived in accordance with the requirements set out by Gordon (1998) and using the resources available to the SeaWiFS Project. A reasonably good estimate of the band 7 gain was made for the current data. This method will be applied as new calibration points and algorithm improvements become available.

Chapter 6

MOBY Data Analysis for the Vicarious Calibration of SeaWiFS Bands 1–6

ROBERT E. EPLEE, JR.
SAIC General Sciences Corporation
Beltsville, Maryland

CHARLES R. MCCLAIN
NASA Goddard Space Flight Center
Greenbelt, Maryland

ABSTRACT

The CVT performs the vicarious calibration of SeaWiFS by comparing normalized water-leaving radiances retrieved from SeaWiFS imagery with contemporaneous measurements of normalized water-leaving radiances from MOBY. This is a system-level calibration that incorporates the performance of both the sensor and the atmospheric correction algorithm. The vicarious gains for bands 1–6 depart from unity over a range of approximately 1–4%, depending on the band, which is consistent with the uncertainty in the prelaunch calibration of SeaWiFS.

6.1 INTRODUCTION

Variations in the radiometric response of the eight SeaWiFS bands with time, and uncertainties in the atmospheric correction algorithm, require a mission-long vicarious calibration program to monitor the performance of the sensor system, instrument plus atmospheric correction algorithm (Evans and Gordon 1994), to meet the radiometric constraints on the ocean color data set (McClain et al. 1992 and 1998). The temporal stability of the on-orbit calibration of the instrument is monitored with a time series of lunar calibration data (Eplee and Barnes 2000). The CVT is using data from MOBY (Clark et al. 1997), deployed off of Lanai, Hawaii, for the vicarious calibration of SeaWiFS bands 1–6.

The CVT performed the vicarious calibration of SeaWiFS by comparing normalized water-leaving radiances, L_{WN} (Gordon and Clark 1981), measured by MOBY with L_{WN} retrieved by SeaWiFS from contemporaneous overflight images of the buoy site. The vicarious calibration process adjusts the prelaunch calibration gains to minimize the difference between the SeaWiFS and MOBY L_{WN} in bands 1–6. Because no methodology has been developed to vicariously calibrate bands 7 and 8, the gains for these bands are adjusted to optimize the atmospheric correction in the vicinity of MOBY (Robinson and Wang 2000).

The vicarious calibration is independent of the time correction derived from the lunar calibrations (Eplee and Barnes 2000). The CVT has derived a set of system gains which, when applied to the SeaWiFS calibration, yields values for L_{WN} measured by SeaWiFS and MOBY that agree to better than 1%. These gains are defined in a simplified version of the SeaWiFS level-1b calibration equation:

$$
\begin{aligned}
L_S(\lambda) \ = \ & \big(C_{\text{out}}(\lambda) - C_{\text{dark}}(\lambda)\big)\, K_1(g, d, \lambda) \\
& \times \ K_2(\lambda)\, \alpha(\lambda) \Big[\beta(\lambda) \ + \ \gamma(\lambda) \\
& \times \ (t - t_0) \ + \ \delta(\lambda)\, (t - t_0)^2 \Big],
\end{aligned}
\tag{20}
$$

where:

   λ is the wavelength of measurement;

   L_S is the calibrated at-sensor radiance;

  C_{out} is the counts from sensor output data;

C_{dark} is the median value of dark count from sensor output data;

   K_1 is the counts to radiance conversion factor (calibration coefficient);

   g is the gain;

   d is the detector;

   K_2 is the additional calibration factors;

   α is the vicarious gain;

   β is the constant term in temporal correction;

   γ is the linear (in time) term in temporal correction;

   δ is the quadratic (in time) term in temporal correction;

t is the time tag of sensor output data; and

t_0 is the reference time for temporal correction.

The reference time for the temporal correction is the time tag of the first SeaWiFS on-orbit image, which was obtained on 4 September 1997 at 162630 UTC. The full level-1b calibration equation is presented in Eplee and Barnes (2000).

In some of the SeaWiFS level-1a data sets, the dark count for particular scan lines may have spuriously high values. In addition, the dark count radiance for some bands is midway between two digitization levels. These two effects can give rise to a *striping* effect in the level-2 products. To avoid this striping, the median value of the dark counts for each band over each scene is computed and subtracted from each scan line in the scene.

The determination of the temporal correction factors is presented in Eplee and Barnes (2000) and discussed in Barnes et al. (1999a). The vicarious calibration strategy employed by the CVT assumes that the temporal corrections to the instrument calibration yield stable top-of-the-atmosphere radiances from SeaWiFS. This paper discusses the current strategy employed by the CVT to determine the vicarious gains, α, for each band.

6.2 NEAR-INFRARED CALIBRATION

Because open ocean reflectances are low ($\approx 2\%$), approximately 90% of the top-of-the-atmosphere signal observed by SeaWiFS over the oceans is due to Rayleigh scattering of sunlight and to aerosol radiance within the atmosphere. The SeaWiFS atmospheric correction algorithm must remove this atmospheric signal to yield the water-leaving radiances.

The atmospheric correction algorithm estimates the aerosol radiance L_A (which is equal to $L_a + L_{ra}$), for bands 7 and 8, and extrapolates L_A in the other SeaWiFS bands using the ratio of L_A in band 7 to that in band 8 (Gordon and Wang 1994a). This ratio is called ϵ [$\epsilon(765, 865)$]. Currently, the vicarious gain for band 8 is defined to be unity.

The calibration of band 7 is accomplished by adjusting the gain for band 7 so that the ϵ value has the expected value for a set of open-ocean scenes in the vicinity of MOBY. This procedure is discussed in Robinson and Wang (2000). The gain for band 7 derived for the vicarious calibration discussed here is 0.946.

6.3 VISIBLE BAND CALIBRATION

In performing the vicarious calibration, the CVT has produced a match-up data set of simultaneous observations of L_{WN} from SeaWiFS and MOBY observations. The current vicarious calibration data set contains 125 matchups spanning a 906 day time range from 19 September 1997 through 13 March 2000.

6.3.1 SeaWiFS Data Selection

The SeaWiFS observations are mean water-leaving radiances (L_W) computed for 3×3 pixel regions centered on the pixel containing MOBY, where at least five pixels in the region pass the exclusion criteria:

a) Land;

b) Clouds and ice;

c) Sun glint;

d) Stray light;

e) Total radiance above the knee of the bilinear gain;

f) Low water-leaving radiance in band 5;

g) Atmospheric correction algorithm failure;

h) Scan angle greater than 45°;

i) Satellite zenith angle greater than 56°;

j) Solar zenith angle greater than 70°;

k) Turbid water;

l) Coccolithophore; and

m) Aerosol optical depth in band 8 greater than 0.1.

These criteria are based on standard quality control masks and flags, computed on a pixel-by-pixel basis. It should be noted that some of these criteria are not directly applicable to observations obtained around MOBY, such as turbid water and coccolithophores, but are included to maintain consistency with other SeaWiFS match-up analyses such as Bailey et al. (2000). Sun glint in the SeaWiFS scenes can be interpreted by the atmospheric correction algorithm as aerosol radiance. To avoid sun glint contamination of the match-up data, an upper limit of 0.1 is set on the aerosol optical depth in band 8 for valid SeaWiFS retrievals. The imposition of this limit results in the loss of several match-up scenes during the summer.

Alternative statistical measures to the mean value (which have been considered for determining the optimum value of L_W in a scene), include the median value of the pixels, the value of the central pixel, and the mode of the pixels. The median value can be affected by outliers. Because the standard deviation of the mean is typically small, the central pixel does not provide a better value than the mean. The mode may provide the best estimate of L_W, but it is difficult to compute for nine pixels. Consequently, the mean value is used in the vicarious calibration.

The mean L_W are converted to L_{WN} for the match-up comparison as discussed in Sect. 6.3.3. The time series of mean SeaWiFS L_{WN} values for the match-up scenes are plotted in Fig. 29. The primary source of noise in the plots is the variation in the atmospheric correction of the SeaWiFS data.

6.3.2 MOBY Data Selection

MOBY measures downwelling irradiances and upwelling radiances over the wavelength range of 340–900 nm at a

subnanometer resolution with two spectrometers coupled by a dichroic beamsplitter. The beamsplitter gives the blue spectrometer a bandpass of 340–600 nm and the red spectrometer a bandpass of 630–900 nm. The potential for stray light is greatly reduced by splitting the visible spectrum at the beginning of the water absorption region, because most of the short wavelength energy is diverted from the entrance slit of the long wavelength spectrometer. The splitting also allows the spectrometers to be optimized, in terms of free spectral range and integration times, for the two distinctive spectral domains.

The MOBY observations are mean water-leaving radiances measured over 30 min. intervals centered on local noon, the satellite overpass time. In-water measurements are made at depths of 2, 5, and 9 m. These measurements are used to compute diffuse attenuation coefficients at each depth and, thus, to derive L_W at the surface. Surface irradiance (E_s) measurements are also made. For the MOBY spectra to be considered valid, the diffuse attenuation coefficients computed for each depth must be consistent with each other. The calibrated MOBY spectra are convolved with the SeaWiFS relative spectral response functions for use in the match-up analysis. The processed MOBY data for a given day includes L_W for bands 1–6 and E_s for bands 1–8. Estimates of E_s from the subsurface data are currently not provided.

High calibration accuracy for the MOBY data requires that the buoy in the water is swapped out for refurbishment and recalibration approximately every three months. To ensure continuous data, the MOBY Project maintains three buoys, one in the water and two undergoing refurbishment. The current vicarious calibration uses match-up data from seven MOBY deployments. The mean L_W is converted to L_{WN} for the match-up comparison as discussed in Sect. 6.3.3. The time series of MOBY L_{WN} are plotted in Fig. 30. The plots show that the MOBY data are stable from one deployment to the next.

Shortly after the launch of SeaWiFS, the above-water E_s detector on MOBY failed. The E_s measurements from MOBY for October and November of 1997 are invalid. This failure is one of the reasons that the CVT uses computed E_s rather than measured E_s for estimating MOBY L_{WN} values in the match-up comparisons of the vicarious calibration.

6.3.3 Match-Up Analysis

In performing the vicarious calibration, the CVT evaluated matchups of L_{WN} between SeaWiFS and MOBY. Initially, SeaWiFS retrievals of L_{WN} were compared with L_{WN} computed from MOBY measurements of L_W and E_s:

$$L_{WN}(\lambda) = \frac{L_W(\lambda, \theta_0)}{E_s(\lambda, \theta_0)} F_0(\lambda), \qquad (21)$$

where F_0 is the solar constant and θ_0 is the solar zenith angle. Because of problems with the E_s measurements,

such as the detector failure mentioned above, this approach was not used in the match-up analysis.

For the match-up analysis, normalized water-leaving radiances were computed from the SeaWiFS retrievals of L_W and from the MOBY measurements of L_W by using the atmospheric diffuse transmittance, $t(\lambda)$:

$$L_{WN}(\lambda) = \frac{L_W(\lambda, \theta_0)}{\cos(\theta_0)\, t(\lambda)}. \qquad (22)$$

The definition for $t(\lambda)$ is:

$$t(\lambda) = \exp\left[\frac{-\left(0.5\tau_r(\lambda) + \tau_{oz}(\lambda) + K_a\right)}{\cos(\theta_0)}\right], \qquad (23)$$

where:

- τ_r is the computed Rayleigh optical thickness;
- τ_{oz} is the ozone optical thickness from the SeaWiFS ancillary data; and
- K_a is the aerosol effects (0.0054) estimated for an aerosol optical thickness of 0.1 and the maritime aerosol model for 90% relative humidity.

The approximation of the aerosol effects with a value independent of wavelength is made because L_A has only a weak dependence on wavelength for the maritime aerosol model. SeaWiFS retrievals of L_{WN} can be compared directly with the L_{WN} computed from the MOBY data using (22). The vicarious calibration, however, is based on the computation of L_{WN} from L_W using (22) for both SeaWiFS and MOBY to minimize the uncertainties due to the approximations made in (22).

As a check on the L_{WN} match-up analysis, the comparisons were also performed for L_W. Because the MOBY observations are centered on the satellite overpass times, the L_W match-ups yielded essentially the same results at the L_{WN} matchups, with equivalent levels of noise in the data.

In performing the vicarious calibration, the vicarious gains, $\alpha(\lambda)$ in (20), were adjustd to optimize the agreement between the L_{WN} retrieved by SeaWiFS with the L_{WN} measured by MOBY in each band. To avoid any residual seasonal variations in solar illumination, the ratios of the SeaWiFS values to the MOBY values ($L_{WN}^{S:M}$) were computed in each band for each scene. Because the distribution of the ratios of L_{WN} is more log-normal than normal, the vicarious gains were adjusted until the geometric mean of the ratios for each band was essentially unity.

The results of the vicarious calibration, shown in Table 11 and plotted in Fig. 31 as functions of time, were derived using an atmospheric correction algorithm which incorporates the near-infrared reflectance correction of Siegel et al. (2000). Other estimators of the $L_{WN}^{S:M}$ over the match-up scenes were considered (i.e., the arithmetic mean, the median, and the mean of the center quartiles), but the use
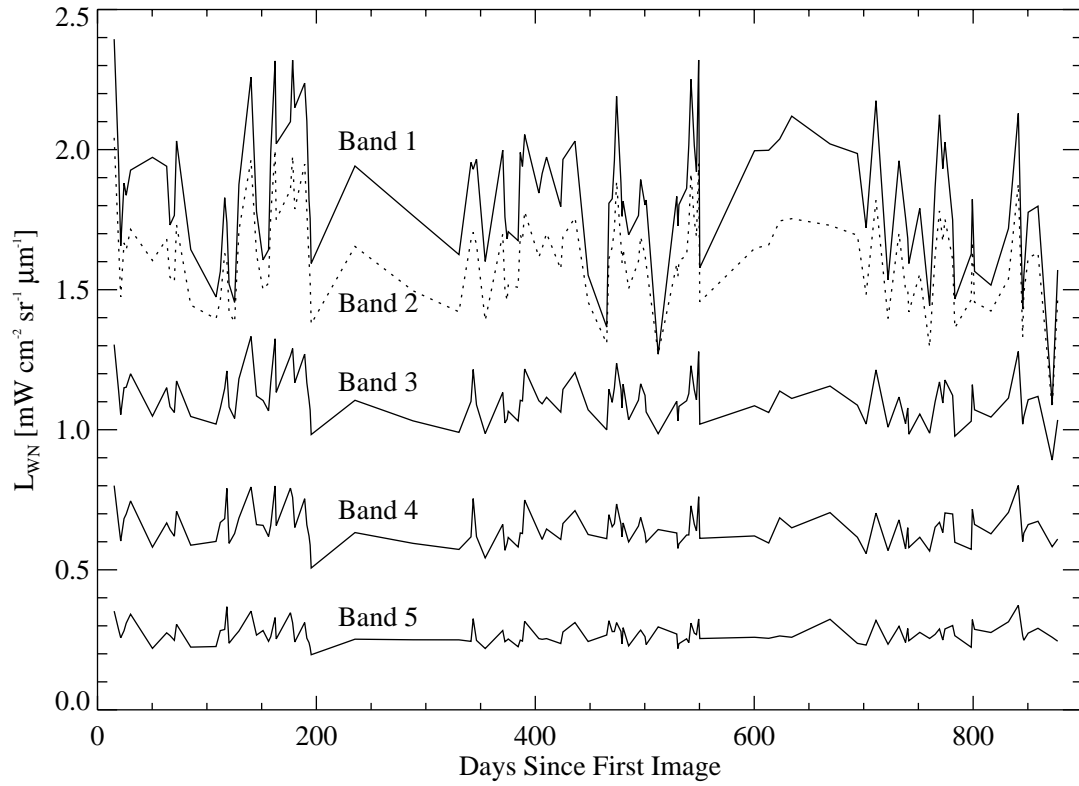
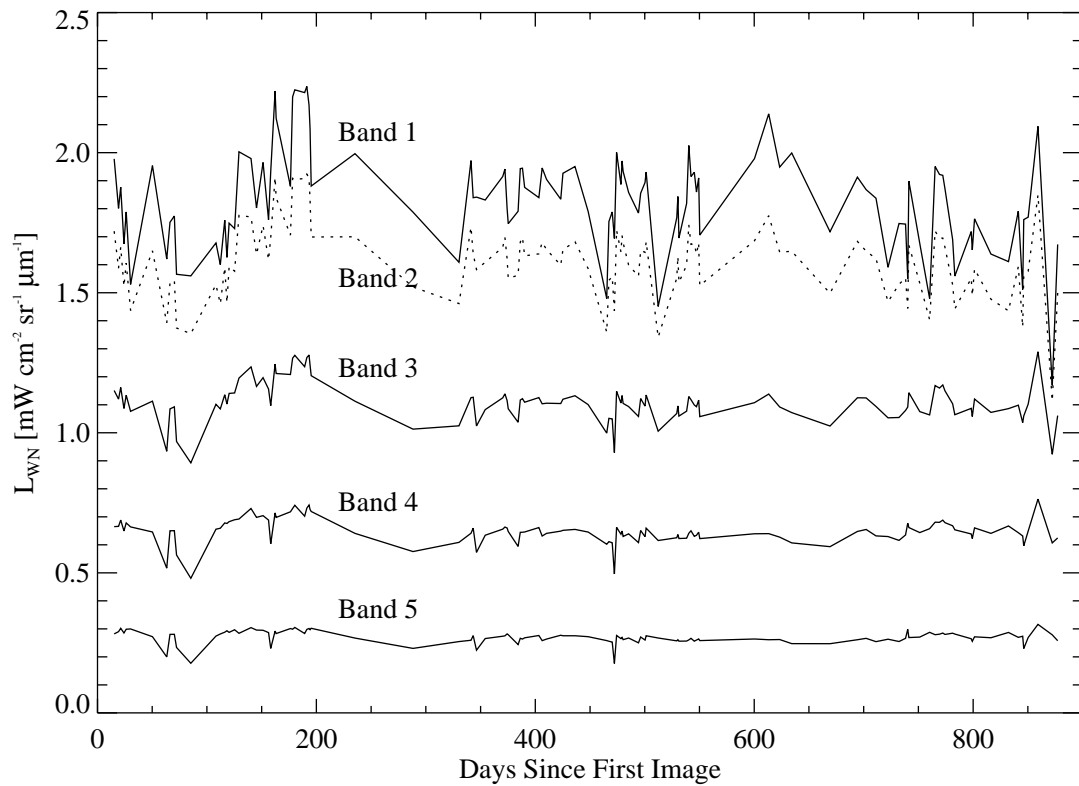**Fig. 29.** SeaWiFS normalized water-leaving radiances for match-up scenes.

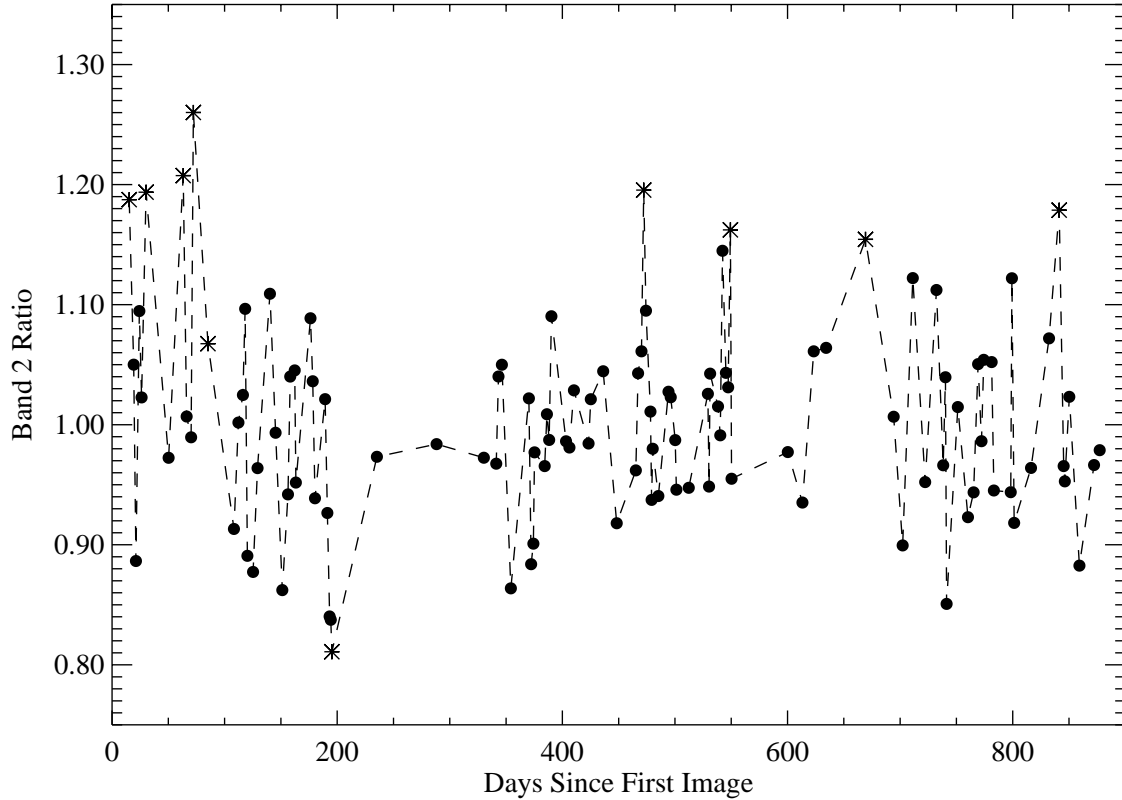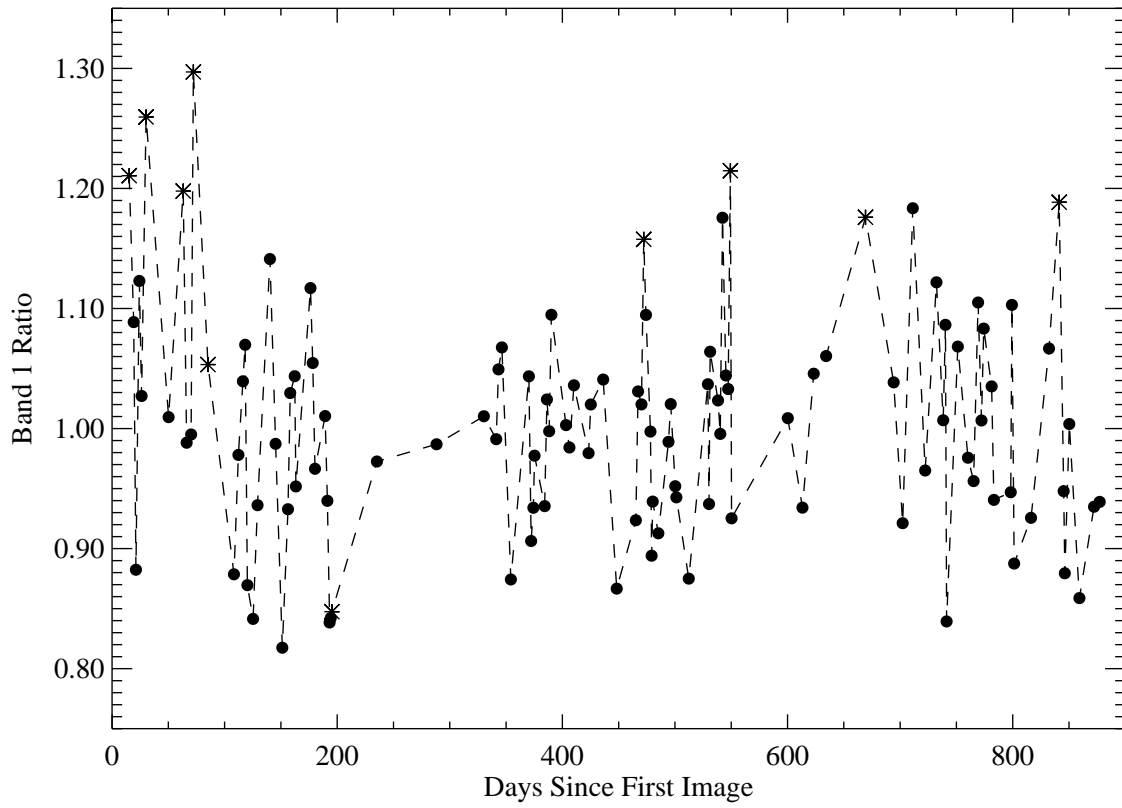**Fig. 30.** MOBY normalized water-leaving radiances for match-up scenes.

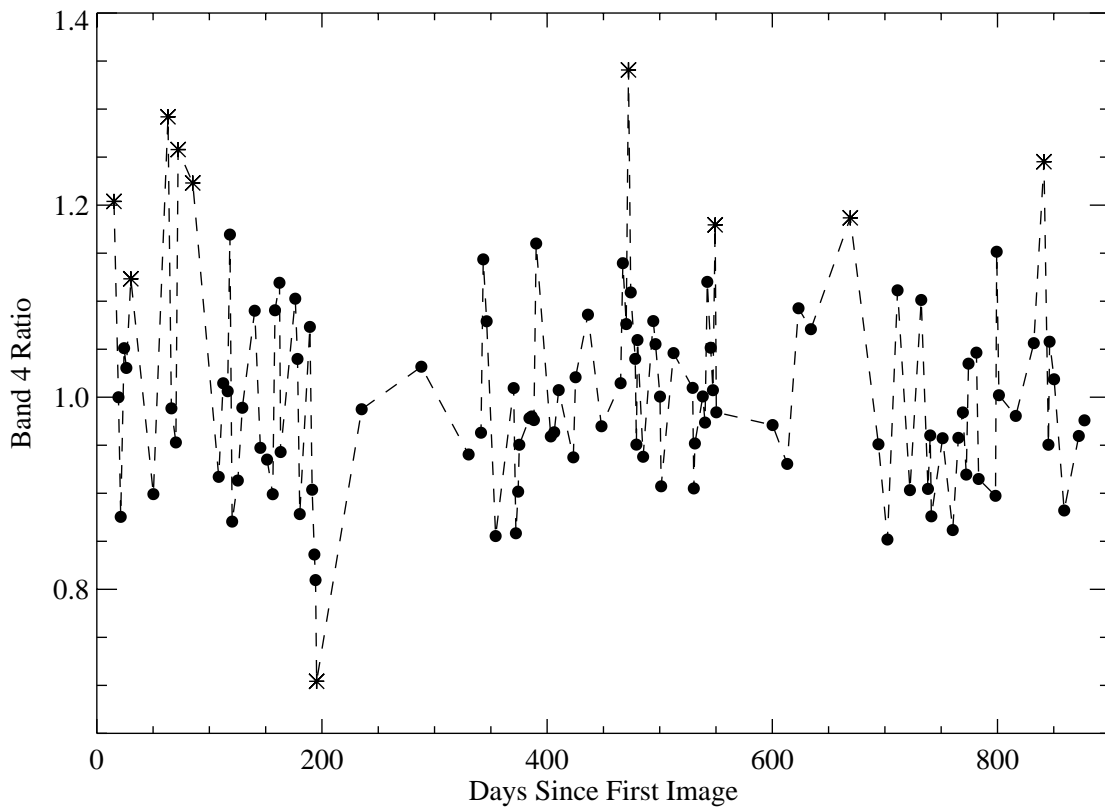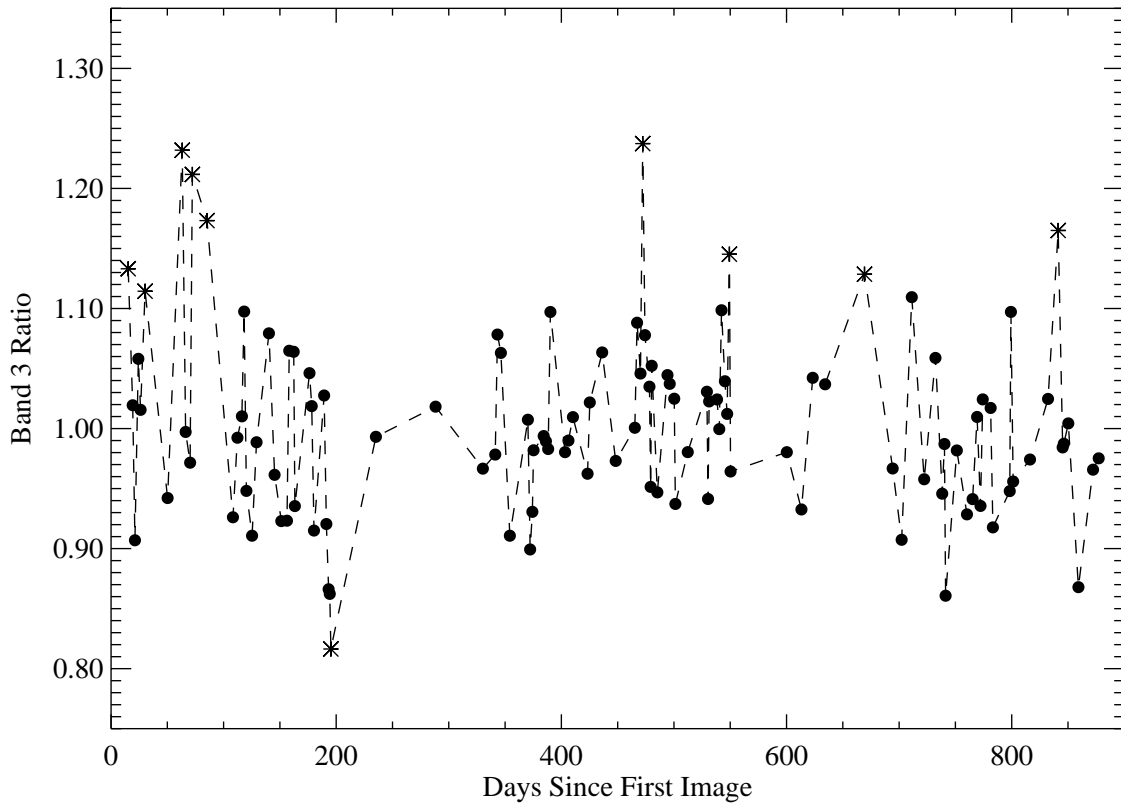**Fig. 31.** Vicarious calibration matchups versus time.

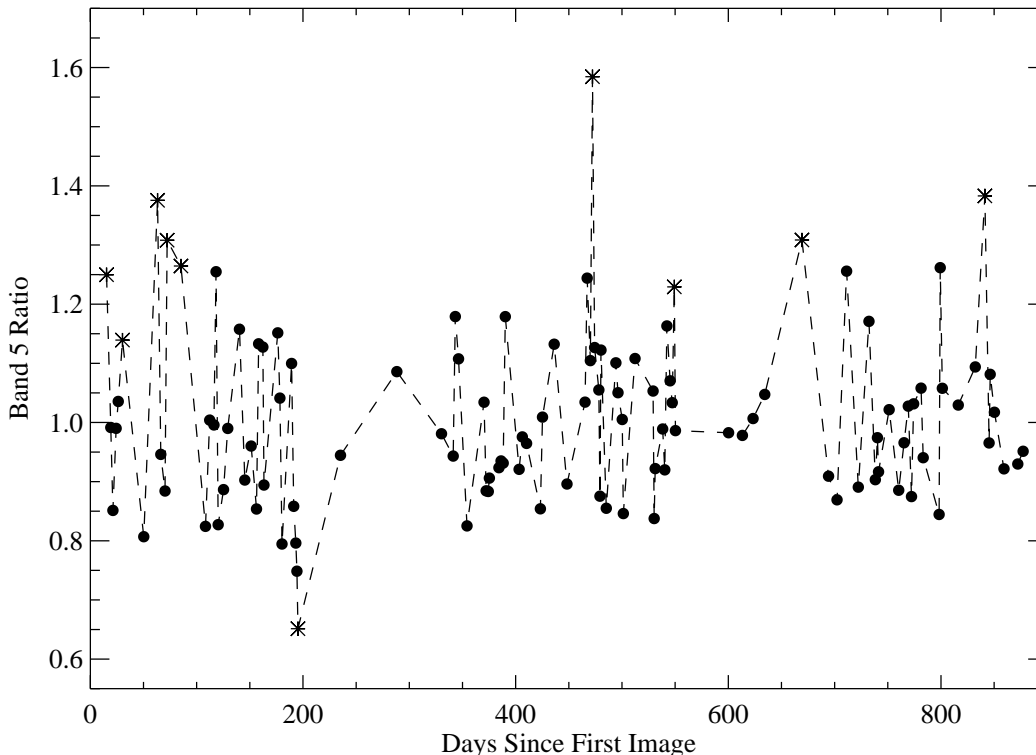**Fig. 31. (cont.)** Vicarious calibration matchups versus time.

Fig. 31. (cont.) Vicarious calibration matchups versus time.

Table 11. Results of the SeaWiFS vicarious calibration. The MOBY and SeaWiFS radiances are in units of $mW\,cm^{-2}\,sr^{-1}\,\mu m^{-1}$.

λ [nm]	MOBY Radiance	SeaWiFS Radiance	Mean Ratio (SeaWiFS/MOBY)	Vicarious Gain
412	1.8263525	1.8263380	0.9999204	1.00310
443	1.6133271	1.6133275	1.0000002	0.991158
490	1.1106925	1.1106931	1.0000005	0.959938
510	0.65016730	0.65016802	1.0000012	0.985839
555	0.27024732	0.27024714	0.99999934	0.993857
670	0.014412810	0.014454512	1.0069607	0.959650
765				0.946
865				1.000

of these other estimators had a negligible effect ($<0.1\%$) on the vicarious gains.

The vicarious calibration of band 6 is difficult because of the low values of L_{WN} in this band. Several of the Sea-WiFS scenes yield negative L_{WN} for band 6. Additionally, the calibration of MOBY over this band pass is problematic because of the crossover between the two spectrometers (D. Clark, pers. comm.). As a result, the matchups where negative L_{WN} values occurred for band 6 were excluded from the vicarious calibration.

Figure 31 shows a number of matchups that are *outliers*. These outliers are defined to be individual match-up data points for any of bands 1–5 that deviate from the mean ratio in that band by more than two standard de-

viations (2σ). The CVT has attempted to determine why the outlier matchups plotted in these figures deviate so far from the mean $L_{WN}^{S:M}$ ratios. The CVT has looked for correlations between the outliers and solar zenith angles, spacecraft zenith angles, aerosol optical depth, ϵ value, chlorophyll concentration, local wind speed, and ozone concentration without success. The use of the geometric mean in estimating the $L_{WN}^{S:M}$ ratios allows the outlier matchups to be included in the vicarious calibration.

The match-up time series plotted in Fig. 31, excluding the outlier matchups, do not show any trends with time, which indicate the time corrections applied to bands 1, 2, 5, 6, 7, and 8 do not have any significant residual errors. Earlier during the mission, a 0.5% error in the ratio of

bands 7:8 of gave rise to a discernable error in the match-up time series. The matchups will be discussed as functions of scan angle in Eplee and McClain (2000).

6.4 DISCUSSION

The departure of the vicarious gains for bands 1–6 from unity are the result of uncertainties in the atmospheric correction algorithm, uncertainties in the laboratory calibration of SeaWiFS, and uncertainties in the laboratory calibration of MOBY. The uncertainty in the SeaWiFS calibration, as estimated by the vicarious gains, ranges from 1–4% depending on the band. This result is consistent with the uncertainty derived from the prelaunch recalibration of SeaWiFS (Johnson et al. 1999) and with the uncertainty derived from the calibration transfer-to-orbit experiment (Barnes et al. 1999b).

The time series of $L_{WN}^{S:M}$ match-up values provides the CVT with a check on the time corrections applied to the individual bands. Currently, the time series show no significant residual errors. As the number of matchups increases with time, the accuracy of these checks will increase accordingly.

The latest set of vicarious gains should be applied to the SeaWiFS data in conjunction with the current SeaWiFS calibration table, which contains the temporal corrections for the instrument. The CVT will periodically update the vicarious calibration coefficients over the five-year SeaWiFS mission, e.g., at each reprocessing, as additional matchups become available.

Chapter 7

The Updated SeaWiFS Coccolithophore Algorithm

Wayne D. Robinson
SAIC General Sciences Corporation
Beltsville, Maryland

Abstract

A coccolithophore identification algorithm has been adapted to work reasonably well for SeaWiFS data containing coccolithophore blooms at a number of sites in the Bering Sea and the North Atlantic. Changes were made in the initial algorithm thresholds that resulted in considerable improvements in the detection of coccolithophores for some cases. Future studies should include additional conditions which were considered in the formulation of the original coccolithophore algorithm, but not considered here—red tides, sediments, whitings, and haze. Finally, a future study may want to re-examine the predictors that are employed to detect the coccolithophore signal. The SeaWiFS 443, 510, and 555 nm bands are slightly different than the CZCS bands used to derive the current predictors. In addition, SeaWiFS has bands at 412 and 490 nm, which CZCS did not have, and these might be useful in deriving a better set of predictors to detect coccolithophores and other water types.

7.1 INTRODUCTION

The algorithm for detecting coccolithophores in Sea-WiFS data was initially developed with the aid of CZCS measurements taken for various water conditions, including the presence of coccolithophores (Brown and Yoder 1994, and Brown 1995). The algorithm was developed by:

a) Empirically determining the spectral signatures of coccolithophore blooms and various common non-bloom conditions;

b) Deciding on feature *predictors*, i.e., spectral quantities which are correlated to the presence of coccolithophores, to be used in the algorithm; and

c) Establishing decision boundary values for each predictor which would allow the blooms to be spectrally distinguished from other conditions.

Predictors were derived from the normalized water-leaving (L_{WN}) radiances in three CZCS bands: 440, 550, and 520 nm and their ratios. Hereafter, the L_{WN} ratio constructed from band A divided by band B is indicated by L_B^A, e.g., the $L_{WN}(490)/L_{WN}(555)$ band ratio is represented by L_{555}^{490}. The following five predictors were employed in the classification algorithm:

1. $L_{WN}(440)$,

2. $L_{WN}(550)$,

3. L_{520}^{440},

4. L_{550}^{440},

5. L_{550}^{520}, and

6. $L_a(670)$ (Brown and Yoder 1994).

These predictors were incorporated into the SeaWiFS level-2 processing program to derive the coccolithophore flag for each image pixel (McClain et al. 1995 and Darzi 1998). When the first SeaWiFS-observed coccolithophore bloom was found in the Bering Sea (Vance et al. 1998), it was discovered that the algorithm was doing a poor job of identifying the bloom, which could clearly be seen in the true color imagery. The predictors were adjusted so that this case, and others during the same bloom, would be identified correctly.

In the months of April–July 1998, many coccolithophore bloom cases were observed in the North Atlantic and the Bering Sea. Comparisons of the coccolithophore flagged areas to the imagery showed that the algorithm was still not identifying part or all of these blooms.

The availability of more coccolithophore test cases and the poor performance of the algorithm on some of these scenes has prompted the re-examination of the coccolithophore algorithm. The work done to improve the algorithm is described here.

7.2 THE COCCOLITHOPHORE TEST

The coccolithophore detection algorithm was developed to identify coccolithophore blooms and separate their signal from those of clear water, red tide, haze, and sediments. Although it was hoped that the algorithm could distinguish *whitings*—suspended lime muds—from coccolithophores, the previous work (Brown 1995) was unable

to distinguish them at all. In addition, the algorithm had difficulty with sediment and atmospheric haze.

The coccolithophore identification tests shown in Table 12 use the aforementioned predictors to eliminate all conditions not caused by coccolithophores. Any remaining data are classified as coccolithophores.

Table 12. The test sequences to identify coccolithophores. The center column indicates the test on the SeaWiFS parameter or ratio, and the right column indicates the condition that exists if this test is true. If none of tests 1–6 are true, the data is considered to contain a significant amount of coccolithophores.

No.	Test	Condition(s)
1	$L_{WN}(550) < 0.8$	Clear water
2	$L_{WN}(440) < 1.1$	Clear water and possibly sediments
3	$L_{550}^{440} < 1.0$	Sediments and red tide
	$L_{550}^{440} > 2.0$	Haze
4	$L_{520}^{440} < 0.95$	Sediments
	$L_{520}^{440} > 1.5$	Haze
5	$L_{555}^{520} < 1.0$ or	Unknown
	$L_{555}^{520} > 1.6$	condition
6	$L_a(670) > 1.1$	Haze
7	Remaining points	Coccolithophores

Several comments should be made about the tests applied to the CZCS data and the thresholds that were used. The test with $L_a(670)$, the aerosol radiance at 670 nm, was added by Brown and Yoder (1994) as a test for haze contamination and was important for use with CZCS data because the CZCS atmospheric correction assumed a fixed aerosol type over an entire scene. This test should now be less critical as SeaWiFS processing corrects for haze on a pixel-by-pixel basis. The bands used for SeaWiFS are slightly different—443, 510, and 555 nm, with the corresponding normalized water-leaving radiances of $L_{WN}(443)$, $L_{WN}(510)$, and $L_{WN}(555)$—as compared to 440, 520, and 550 nm for CZCS (see Hooker et al. 1992 for CZCS and SeaWiFS descriptions).

In addition to the central wave numbers being different, the response functions of the bands are not the same for CZCS and SeaWiFS. To detect coccolithophores with SeaWiFS, it could be expected that some changes would have to be made, at least in the test thresholds if not in the predictors. It should also be expected that in comparisons of coccolithophore-laden waters with clear water, the first two tests (Table 12), which are mainly concerned with discriminating coccolithophores from clear water, should be the determining tests.

The initial tests of this algorithm with SeaWiFS data were done in the first month of operation. At that time, very little data were available containing coccolithophores.

When the algorithm was applied to an observed coccolithophore bloom in the Bering Sea (Vance et al. 1998) from 18 September to 3 October 1997, it was found that the above tests completely missed the identification of coccolithophores and identified neighboring clear water as having coccolithophores. It was assumed that the predictors remained valid and the test thresholds required adjustment.

By examining points in the clear and coccolithophore areas, the tests that determine a coccolithophore bloom were set to the following:

$$\begin{aligned} &\text{if } L_{WN}(555) \geq .81 \text{ and } L_{WN}(443) \geq 1.1 \text{ and} \\ &\quad L_a(670) \leq 1.1 \text{ and} \\ &\quad 0.60 \leq L_{555}^{443} \leq 0.90 \text{ and} \\ &\quad 0.90 \leq L_{555}^{510} \leq 1.20 \text{ and} \\ &\quad 0.60 \leq L_{510}^{443} \leq 0.90, \end{aligned} \quad (24)$$

then this is a coccolithophore pixel.

These were relatively radical changes, but they identified the coccolithophore bloom in the Bering Sea well (Figs. 32a–c), and served as the initial coccolithophore algorithm. With a lack of other cases at the time, these tests were adopted for operational processing as the best set possible.

7.3 TESTS ON NEW CASES

In the months of April–July 1998, a number of new coccolithophore cases appeared, especially in the North Atlantic. Poor performance of the mask in these Atlantic blooms and the availability of more test cases prompted these latest tests to improve the coccolithophore algorithm.

In this study, three cases are examined to aid in the improvement of the coccolithophore algorithm.

1. 20 September 1997 at 0014 UTC: This case is actually one of the original cases in the Bering Sea that was used to tune the thresholds for SeaWiFS data; it will be useful here to verify that the changes still apply to the previous cases.

2. 6 April 1998 at 1629 UTC: This is a coccolithophore bloom which occurred in the North Atlantic (57°W, 40°N).

3. 20 July 1998 at 0046 UTC: This is another bloom in the Bering Sea.

Images are shown of the first two cases (Figs. 32 and 33) to show the performance of the initial and revised algorithms.

Figure 32 shows the 20 September 1997 case. Figure 32a shows an image of the 443 nm level-1a data. This band was chosen because it does the best job of displaying the dark ocean, the bright clouds, and the hazy appearance of the coccolithophore signal. In true-color images, made by assigning the 670, 555, and 412 nm bands to red,
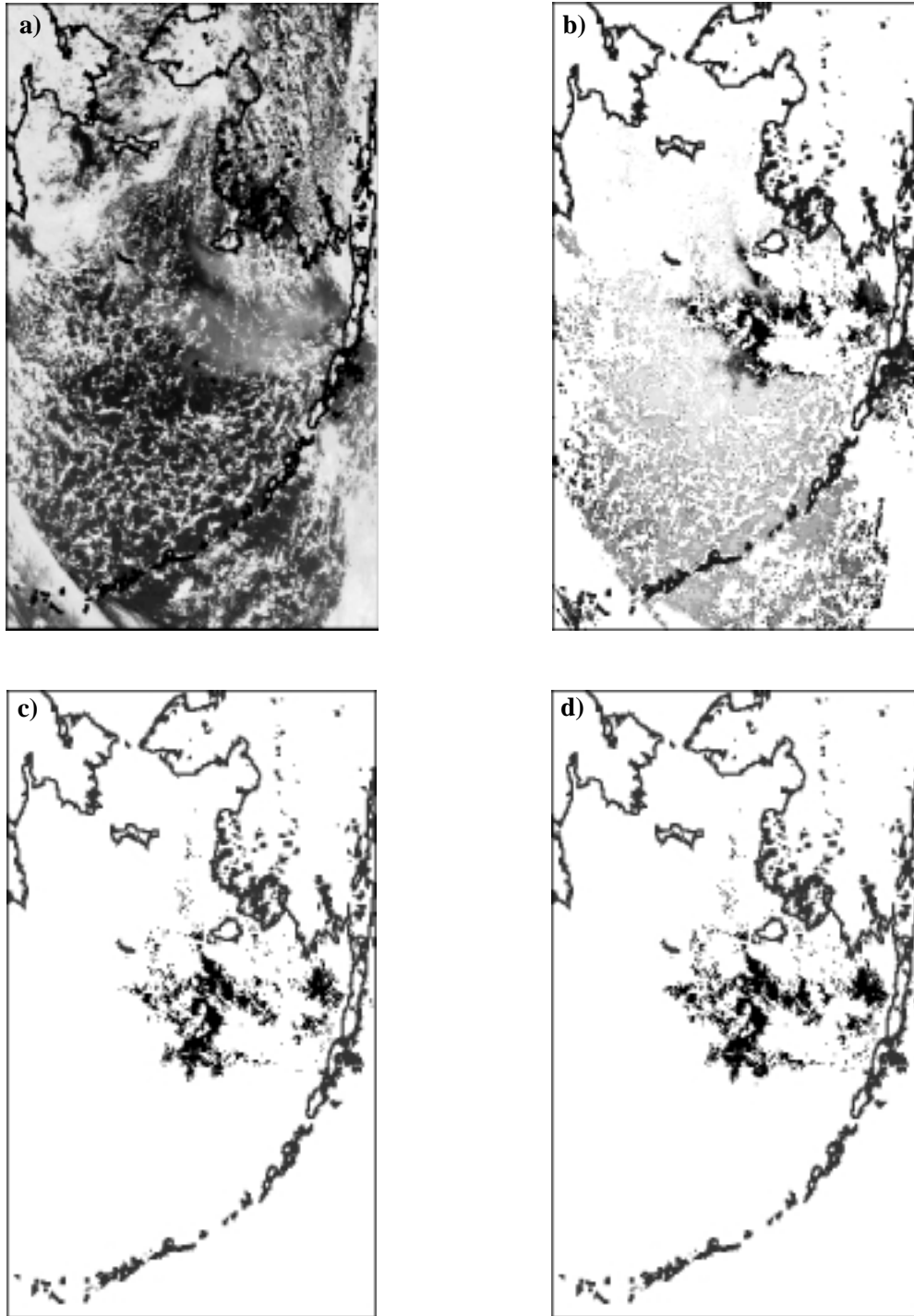
Fig. 32. Images of the coccolithophore bloom seen by the SeaWiFS 443 nm band in the Bering Sea on 20 September 1997 at 0014 UTC. **a)** The 443 nm radiances and an overlay of the coastlines of Alaska and Siberia are shown in black. **b)** The same band is shown with the grey scale inverted to make the coccolithophore area appear dark (the masked areas of clouds, land, and high radiances areas are shaded white, leaving the coccolithophore signal as a dark area in the center). **c)** The same scene as in panel **b** is given, but with the coccolithophore bloom identified by the initial coccolithophore identification algorithm in black. **d)** The coccolithophore is identified in black using the revised algorithm.

Fig. 33. The same as Fig. 32, but for a region of the North Atlantic at (57°W,40°N) on 6 April 1998 at 1629 UTC.
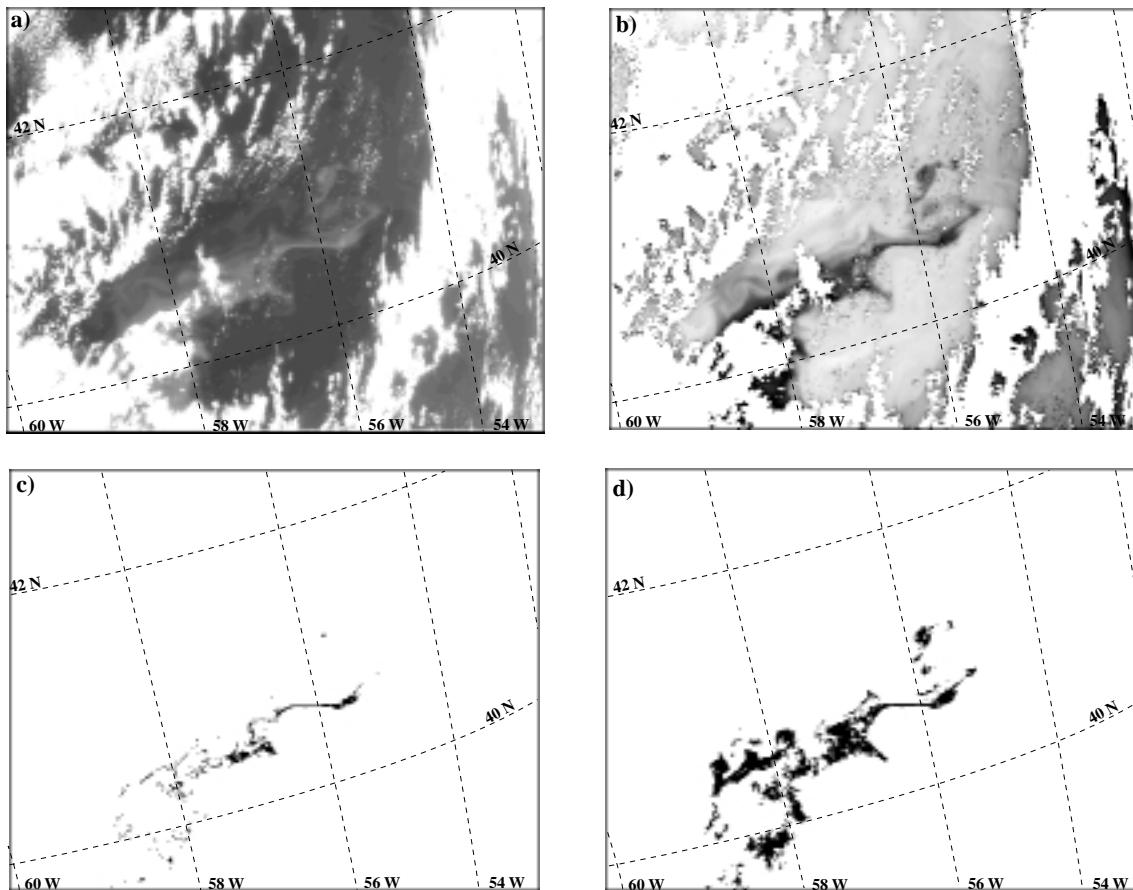
green, and blue respectively, this appears as a distinctly aquamarine region. Figure 32b is an enhanced version of Fig. 32a showing the coccolithophore signal as a darker area in the center of the image. The areas masked for land, high radiances, and clouds are shaded white. The masked region in the center of the coccolithophore bloom (white region) was caused by the unusually high radiances of the bloom. The radiances were so high that they were in the poor resolution portion of the SeaWiFS instrument's detector response (that is, above the *knee* in the instrument bilinear response), which is a masking condition. In Fig. 32c, the pixels the initial algorithm identified as having coccolithophores have been shaded black on a white background. It can be seen that the initial coccolithophore algorithm appears to handle most of the pixels containing coccolithophores (less the masked areas). This would be expected as this was one of the initial training sites.

A similar treatment is shown for the coccolithophore bloom in the Atlantic Ocean that occurred on 6 April 1998 (Figs. 33a–c). For this bloom, only a small fraction of the coccolithophore-affected pixels are identified by the initial algorithm (Fig. 33c). The coccolithophore flag did not work well on the 20 July 1998 case either, although it performed better than in the 6 April case.

Each of the six predictors were examined using selected pixels from the three cases above to determine why the coccolithophore test was not working well on the other cases. The six predictors examined were $L_{WN}(443)$, $L_{WN}(555)$, $L_a(670)$, L_{555}^{443}, L_{555}^{510}, and L_{510}^{443}. For each case, groups of points were selected from three regions of the images with about three observations per region. The first region contained pixels that were not affected by coccolithophores in clear water. The second region contained pixels that had visible coccolithophores, but were not identified by the algorithm as having coccolithophores, and the third had pixels correctly identified as having coccolithophores.

Figures 34a–f display each of the predictor values for the points from the three regions for the three cases considered. To aid in identification, the points are spread in the horizontal and marked with different symbols to separate the three regions: clear (with a diamond symbol); coccolithophore, but not identified (asterisk symbol); and coccolithophore identified (box symbol). The points are also spread horizontally to segregate observations from each of the three cases. In addition to the pixel values, solid horizontal lines are plotted to show the initial thresholds determined for SeaWiFS.
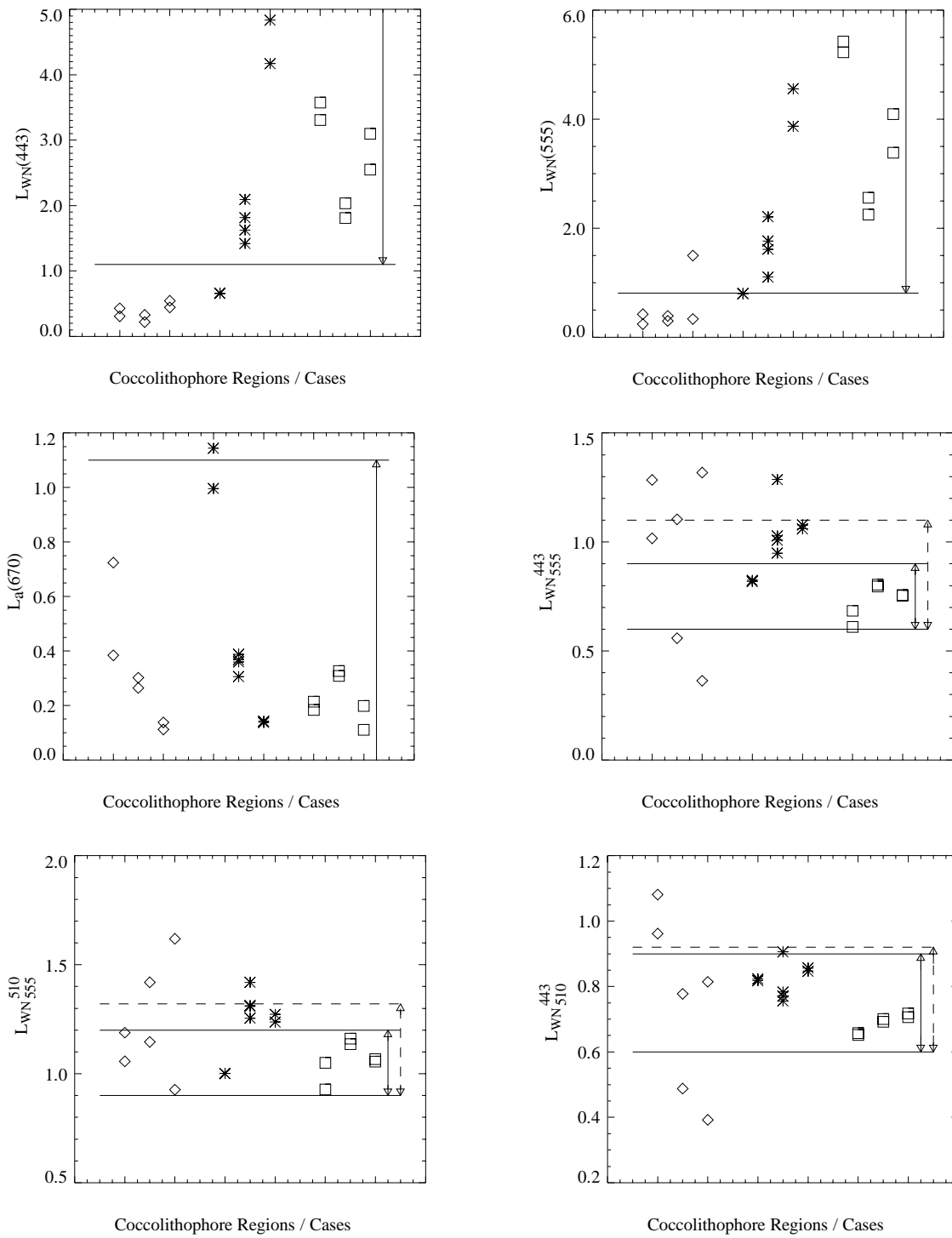
Fig. 34. Graphical plots of the six coccolithophore tests and SeaWiFS test pixels taken in clear waters (diamonds), coccolithophore waters that were not identified by the initial algorithm (asterisks) and coccolithophore waters that were identified by the initial algorithm (squares). The points were taken from three separate coccolithophore events: 20 September 1997 at 0014 UTC in the Bering Sea, 6 April 1998 at 1629 UTC in the North Atlantic, and 20 July 1998 at 0046 UTC in the Bering Sea. The solid horizontal lines indicate the initial test thresholds, while the dashed lines in panels **d, e,** and **f** show the revised high test thresholds. Each test for coccolithophores is positive in the range spanned by the arrow on the right side of the plot. The tests are for: **a)** $L_{WN}(443)$, **b)** $L_{WN}(555)$, **c)** $L_a(670)$, **d)** L_{555}^{443}, **e)** L_{555}^{510}, and **f)** L_{510}^{443}.

The tests for $L_{WN}(443)$ and $L_{WN}(555)$ (Figs. 34a–b) are functioning properly for all of the coccolithophore identified cases and for two of the three coccolithophore not-identified cases. The exception is the 20 September 1997 case, for which the coccolithophore identification already works well. The misidentified points from this case will not be considered as strongly in making revised thresholds because they could represent more complex conditions.

The test for $L_a(670)$ (Fig. 34c) also appears to be functioning well although it is clear that it is of little use in discriminating most of the pixels chosen. This is understandable considering the $L_a(670)$ test is used to remove pixels with high aerosol; the tests in this study use either clear or coccolithophore containing pixels.

The L_{555}^{443}, L_{555}^{510}, and L_{510}^{443} tests (Figs. 34d–f) failed to identify many of the misidentified coccolithophore pixels. In each of these tests, the misidentified pixels have values greater than the high threshold which was initially set. As with the $L_a(670)$ test, these tests show little discrimination between the clear-water and coccolithophore pixels because these tests are used to identify conditions that are not included in the present study (i.e., haze, red tides, and sediments).

High thresholds in the tests for L_{555}^{443}, L_{555}^{510}, and L_{510}^{443} are adjusted by consulting these plots, applying the values to the test cases, and then viewing the resulting masked pixels. The dotted horizontal line in Figs. 34d–f represent the value of the revised high thresholds.

The coccolithophore test with the modified thresholds becomes:

$$\begin{aligned}
&\text{if } L_{WN}(555) \geq .81 \text{ and } L_{WN}(443) \geq 1.1 \text{ and}\\
&L_a(670) \leq 1.1 \text{ and}\\
&0.60 \leq L_{555}^{443} \leq 1.10 \text{ and} \qquad\qquad (25)\\
&0.90 \leq L_{555}^{510} \leq 1.32 \text{ and}\\
&0.60 \leq L_{510}^{443} \leq 0.92,
\end{aligned}$$

then this is a coccolithophore bloom pixel.

The thresholds were increased in a conservative manner for the L_{555}^{443}, L_{555}^{510}, and L_{510}^{443} tests to correctly identify pixels in the test cases. These thresholds could be expanded more, but that should be done only when haze, sediment, and red tide test cases are included in the study.

Figures 32d and 33d show the results of the revised thresholds which do little to change the distribution of identified coccolithophores in the 20 September 1997 case (Fig. 32d), because the initial thresholds were properly identifying most of the coccolithophore pixels. The 6 April 1998 case (Fig. 33d) however, showed a significant improvement in coccolithophore identification. The revised threshold also improved the 20 July 1998 case. The present algorithm does not appear to misidentify clear water as having coccolithophores.

7.4 CONCLUSIONS

The coccolithophore identification algorithm of Brown (1995) has been adapted to work reasonably well for Sea-WiFS data containing coccolithophore blooms at a number of sites in the Bering Sea and the North Atlantic. In some of the newer cases found, the improvements in the testing thresholds have significantly increased the ability to detect coccolithophore blooms, although many aspects of the testing can be improved.

The coccolithophore algorithm was tuned to one case in the Bering Sea and subsequently improved with new cases; however, the number of cases needs to be increased in number and geographical location. This can be accomplished by searching the present data for more coccolithophore cases and by getting more cases from the new data. This study used only a limited number of observations to adjust the thresholds. Future studies may benefit from the use of a greater number of coccolithophore and clear-water observations.

The tests in this study only considered coccolithophore and clear-water conditions. This means that four out of the six testing conditions of the coccolithophore algorithm have not been investigated fully. Future studies should include additional conditions which were considered in Brown's study—red tides, sediments, whitings, and haze. The SeaWiFS Project is starting to compile examples of some of these other conditions.†

Finally, a future study may want to re-examine the predictors that are employed to detect the coccolithophore signal. The SeaWiFS 443, 510, and 555 nm bands are slightly different from the CZCS bands used to derive the current predictors. In addition, SeaWiFS has bands at 412 and 490 nm, which CZCS did not have, and these might be useful in deriving a better set of predictors to detect coccolithophores and other water types.

---

† Browse the calibration and validation image gallery web site at: `http://calval-2.gsfc.nasa.gov/calval/`.

Chapter 8

The SeaWiFS Atmospheric Correction Algorithm Updates

Menghua Wang

University of Maryland, Baltimore County
Baltimore, Maryland

Abstract

Modifications to the atmospheric correction algorithm for the third SeaWiFS reprocessing are described in this chapter. The updates include changes to the aerosol look-up tables, the atmospheric diffuse transmittance tables, the ocean whitecap computations, and the implementation of new Rayleigh radiance tables generated with a variety of ocean surface wind speeds. In addition, computation of a new SeaWiFS atmospheric product, the Ångström exponent, is described. These modifications significantly improve the SeaWiFS retrieval results.

8.1 INTRODUCTION

It is well known that atmospheric correction removes more than 90% of sensor-measured signals contributed from the atmosphere in the visible spectrum, and is the key procedure in ocean color imagery data processing. With the successful launch of SeaWiFS (McClain et al. 1998) on 1 August 1997 and its data processing since then, it is very important to periodically re-evaluate and update the SeaWiFS atmospheric corrections (Hooker et al. 1992).

The SeaWiFS atmospheric correction algorithm uses two near-infrared (NIR) bands (765 and 865 nm) to estimate the aerosol optical properties which are then extrapolated into the visible part of the spectrum (Gordon and Wang 1994a). The implementation of the algorithm was achieved using look-up tables for Rayleigh scattering, aerosol contributions, and the effects of the atmospheric diffuse transmittance. Ocean whitecap contributions at the SeaWiFS bands were estimated using a reflectance model. In this chapter, a brief overview of the SeaWiFS atmospheric correction algorithm is presented, and outlines are given of some updates and modifications in the aerosol look-up tables, the atmospheric diffuse transmittance tables, and computations of the whitecap contributions.

8.2 ALGORITHM

To better describe the SeaWiFS atmospheric correction algorithm and its implementation into the data processing system, the reflectance $\rho = \pi L/(F_0 \cos \theta_0)$ is defined, where L is the radiance in a given solar and viewing geometry, F_0 is the extraterrestrial solar irradiance, and θ_0 is the solar zenith angle. The SeaWiFS measured reflectance

at the TOA can be written as:

$$
\begin{aligned}
\rho_t(\lambda) \;=\; & \rho_r(\lambda) \;+\; \rho_a(\lambda) \;+\; \rho_{ra}(\lambda) \\
& +\; t(\lambda)\rho_f(\lambda) \;+\; t(\lambda)\rho_W(\lambda),
\end{aligned}
\tag{26}
$$

where $\rho_r(\lambda)$, $\rho_a(\lambda)$, and $\rho_{ra}(\lambda)$ are the contributions from multiple scattering of air molecules (Rayleigh scattering), aerosols, and Rayleigh-aerosol interactions, respectively; $\rho_f(\lambda)$ is the reflectance at the sea surface which arises from sunlight and skylight reflecting from foam (or whitecaps) on the surface (Gordon and Wang 1994b); and $\rho_W(\lambda)$ is the water-leaving reflectance, which is the desired quantity in ocean color remote sensing. The $t(\lambda)$ term is the atmospheric diffuse transmittance (Wang 1999, and Yang and Gordon 1997) which accounts for the effects of propagating water-leaving and whitecap reflectances from the sea surface to the TOA. The surface sun glint term has been ignored in (26).

Because more than 90% of the signal in the visible spectrum measured at the satellite altitude is contributed by the atmosphere and ocean surface effects—the first four terms in (26)—accurately removing these effects is crucial to the success of any ocean color remote sensing experiment. The SeaWiFS atmospheric correction algorithm (Gordon and Wang 1994a) uses the two SeaWiFS NIR bands centered at 765 and 865 nm to estimate the atmospheric effects and extrapolate these into the visible spectrum. Unlike Rayleigh scattering, which can be computed accurately, aerosol scattering is highly variable, and the effects of $\rho_a(\lambda) \;+\; \rho_{ra}(\lambda)$ in (26) on the imagery cannot be predicted *a priori*. The water-leaving reflectance at the two NIR bands, however, is usually negligible because of strong water absorption. The radiances measured at these

two NIR bands, therefore, are essentially the contributions from the atmosphere. For the two SeaWiFS NIR channels, (26) can be written as

$$\rho_t(\lambda) - \rho_r(\lambda) - t(\lambda)\rho_f(\lambda) = \rho_a(\lambda) + \rho_{ra}(\lambda). \qquad (27)$$

The effects of $\rho_a(\lambda) + \rho_{ra}(\lambda)$ interactions in the imagery, therefore, can be estimated at the two NIR bands from the sensor-measured radiances, the computed Rayleigh scattering reflectances, and the estimated whitecap contributions (Gordon and Wang 1994b). This quantity is then extrapolated and removed in the visible.

The extrapolation was achieved through a process of aerosol model selection based on an evaluation of the atmospheric correction parameters, $\epsilon(\lambda_i, \lambda_j)$. The latter is defined as (Gordon and Wang 1994a, and Wang and Gordon 1994):

$$\epsilon(\lambda_i, \lambda_j) \; = \; \frac{\rho_{as}(\lambda_i)}{\rho_{as}(\lambda_j)}, \qquad (28)$$

where $\rho_{as}(\lambda_i)$ and $\rho_{as}(\lambda_j)$ are the single scattering aerosol reflectances at wavelengths λ_i and λ_j, respectively. The λ_j value is usually taken as the longest NIR band (865 nm for SeaWiFS). The $\epsilon(\lambda_i, \lambda_j)$ value characterizes the spectral variation of the aerosol extinction coefficient which includes the aerosol optical thickness, single scattering albedo, and aerosol scattering phase function, thereby linking the value of $\epsilon(\lambda_i, \lambda_j)$ and the aerosol model.

The implementation of the atmospheric correction algorithm into the SeaWiFS data processing system was achieved through the use of look-up tables based on a large number of radiative transfer simulations (approximately 25,000) which use the aerosol models developed by Shettle and Fenn (1979). The main look-up tables contain information on the $\rho_a(\lambda) + \rho_{ra}(\lambda)$ values for various aerosol optical and microphysical properties (for a number of different aerosol models with a variety of aerosol optical thicknesses) along with solar and viewing geometries at the eight SeaWiFS spectral bands. The two other tables, which are much smaller in size, are the $\rho_r(\lambda)$ and $t(\lambda)$ tables.

To obtain the value of $\rho_W(\lambda)$ in (26), four quantities have to be estimated: a) $\rho_r(\lambda)$, b) the reflectance of $\rho_a(\lambda) + \rho_{ra}(\lambda)$, c) $t(\lambda)$, and d) $\rho_f(\lambda)$. In the following four sections, some updates are discussed for the aerosol look-up tables $\rho_a(\lambda) + \rho_{ra}(\lambda)$, the atmospheric diffuse transmittance tables, modifications in computing $\epsilon(\lambda_i, \lambda_j)$ when its value lies outside of the model range, and modifications in computing the foam reflectance contribution.

8.3 AEROSOL LOOK-UP TABLES

Before the reprocessing (prior to August 1998), the SeaWiFS aerosol look-up tables were generated using 12 aerosol models with 8 aerosol optical thicknesses (0.05, 0.1, 0.15, 0.2, 0.3, 0.4, 0.6, and 0.8) and various solar and viewing geometries. The 12 aerosol models are based on three aerosol types, maritime, coastal, and tropospheric, and four relative humidity (RH) values of 50, 70, 90, and 99. The maritime and tropospheric aerosol models are from Shettle and Fenn (1979), whereas the coastal model is derived from their works as described in Gordon and Wang (1994b). These aerosol models are believed to be representative of the aerosol optical properties over the ocean. Table 13 provides the 12 aerosol model names, model numbers, and their corresponding RH values used before the reprocessing. These 12 aerosol models were used as candidates for generating the aerosol look-up tables for the atmospheric corrections.

Table 13. The 12 aerosol models used before the reprocessing. The model names are formed from a one-letter code indicating the model type, "C" for coastal, "M" for maritime, and "T" for troposheric, followed by a two-digit RH value.

No.	RH [%]	Names
1–4	50, 70, 90, and 99	M50 ... M99
5–8	50, 70, 90, and 99	C50 ... C99
9–12	50, 70, 90, and 99	T50 ... T99

Figures 35a and 35b provide examples of $\epsilon(\lambda, 865)$ as a function of wavelength for these 12 aerosol models. Figure 35a is for the case of $\theta_0 = 0°$ and a sensor zenith angle of $\theta = 45°$, whereas Fig. 35b is for $\theta_0 = 60°$ and $\theta = 45°$ with a relative azimuthal angle of $\phi = 90°$. As discussed in the previous section, the $\epsilon(\lambda, 865)$ values, as shown in Figs. 35a and 35b, were used as guides to select the aerosol model, and its optical and radiative properties were extrapolated from the SeaWiFS NIR bands into the visible spectrum in the atmospheric corrections.

As shown in Figs. 35a and 35b, the T50 and M99 aerosol models give the highest and lowest $\epsilon(\lambda, 865)$ values within these 12 aerosol models, respectively. The T50 and M99 aerosol models, therefore, were taken as default models such that, if the retrieved $\epsilon(765, 865)$ value is higher (lower) than the value predicted by the T50 (M99) model, the retrieval model is defaulted to the T50 (M99) aerosols. Figures 35a and 35b show that in the single scattering case, for the M99 model, the aerosol reflectance at 412 nm contributes a factor of approximately 0.85–0.93 at 865 nm, while for the T50 model, the aerosol reflectance at the 412 nm wavelength is a factor of approximately 2.2–2.4 higher than at the 865 nm wavelength.

In the SeaWiFS data processing, however, there was evidence that some new aerosol models needed to be included, in particular, for the optical properties with lower $\epsilon(\lambda, 865)$ values:

1. It was found that there was a significant number of pixels defaulting to the M99 aerosol models, indicating that the lowest $\epsilon(765, 865)$ value predicted by the M99 model was still too high. For example, some case studies showed that about 35–40% of the retrievals defaulted to the M99 aerosol model.
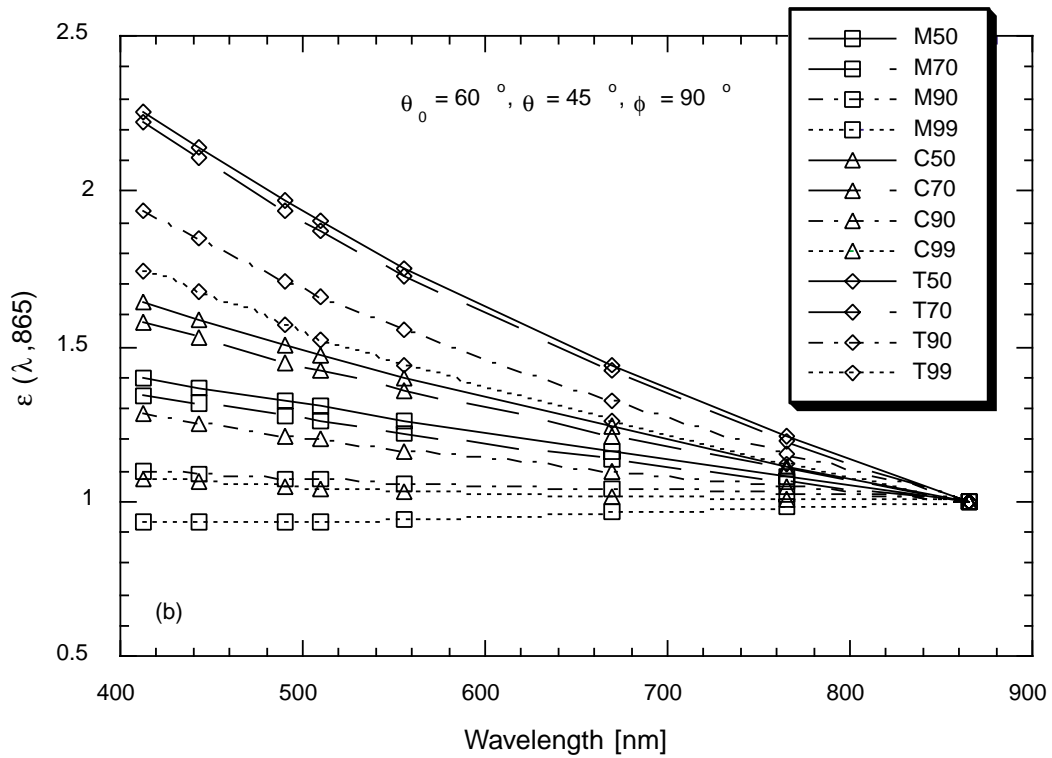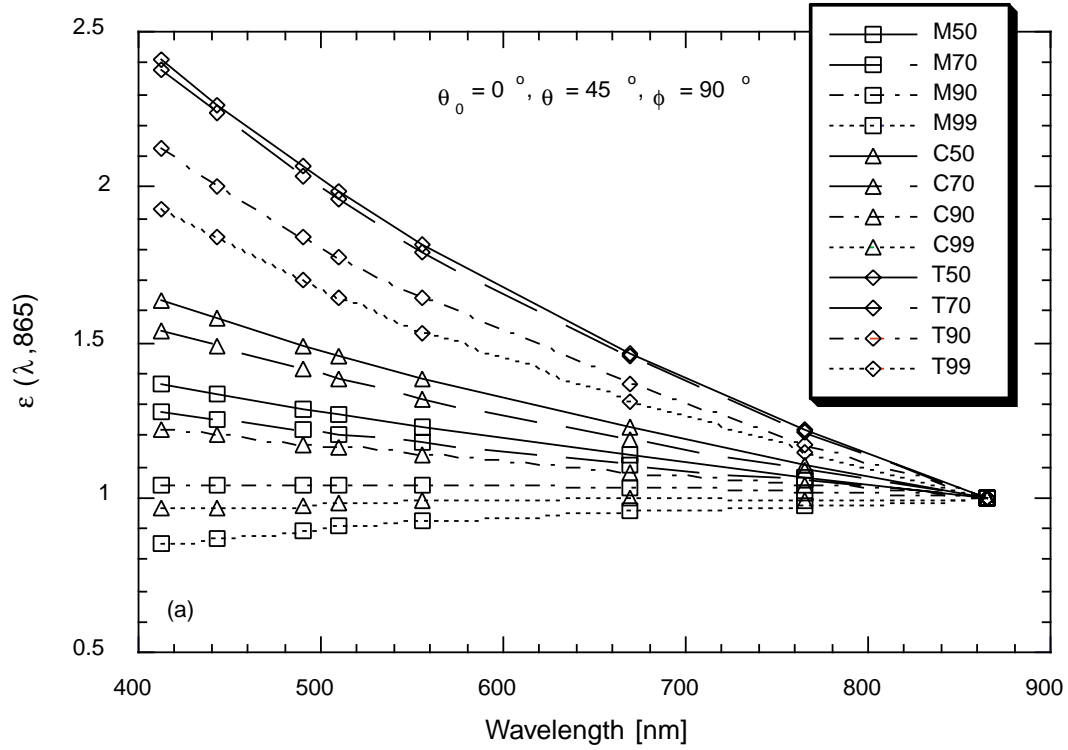
Fig. 35. The $\epsilon(\lambda, 865)$ value as a function of wavelength for the 12 aerosol models used before the reprocessing for the sensor zenith angle of $\theta = 45°$, and the solar zenith angle of **a)** $\theta_0 = 0°$ and **b)** $\theta_0 = 60°$.

2. It appeared that SeaWiFS retrieved more pixels associated with the negative water-leaving reflectance at the short wavelengths than at the long wavelengths, which indicated that probably for some cases, the aerosol contributions at the short wavelengths were overestimated.

For these reasons, the decision was made to update the aerosol look-up tables.

Following a reccommendation from H. Gordon (pers. comm.), the oceanic aerosol model from Shettle and Fenn (1979) was added into the candidate models. During the second reprocessing (August 1998 to December 1999), the C70 and T70 models were replaced by the oceanic aerosols with an RH of 90 and 99% (O90 and O99, respectively). It was found, however, that in some cases (depending on the solar and viewing geometry), the ϵ values predicted by the O90 model intersected with that of the M99 model (depending on the wavelength), e.g., the O90 model predicts a higher ϵ value at 765 nm and a lower value at 443 nm than those of the M99 model which leads to discontinuities in the SeaWiFS derived products.

In the third reprocessing, therefore, only the T70 model was replaced by the O99 model. The number of aerosol models was kept at 12, and Table 14 shows the 12 aerosol models used in the updated aerosol look-up tables. Using the same solar and viewing geometries as in Fig. 35, Figs. 36a and 36b provide the values of $\epsilon(\lambda, 865)$ as a function of wavelength, λ, for the updated aerosol models.

Table 14. The updated 12 aerosol models used in the reprocessing which include the new oceanic model type (O99).

No.	RH [%]	Names
1	99	O99
2–5	50, 70, 90, and 99	M50 … M99
6–9	50, 70, 90, and 99	C50 … C99
10–12	50, 90, and 99	T50 … T99

With the Oceanic aerosol model, the lowest $\epsilon(\lambda, 865)$ value is expanded. The O99 model predicts a factor of approximately 0.7 single scattering aerosol reflectance contribution at 412 nm as at 865 nm; this value is lower than the value from the M99 model (approximately 0.85–0.93). Inclusion of the new models decreased the number of pixels being processed with the default aerosol model by more than one half.

In addition, the computation of the $\epsilon(\lambda, 865)$ values was modified for cases where the retrieved $\epsilon(765, 865)$ value was lower than the lowest predicted values of the 12 models (i.e., the O99 model). Instead of using the default model to compute $\epsilon(\lambda, 865)$, an analytical formula (Wang and Gordon 1994) was used with retrieved $\epsilon(765, 865)$ values to estimate $\epsilon(\lambda, 865)$:

$$\epsilon(\lambda, 865) = \exp\left[\ln\left(\epsilon(765, 865)\right)\frac{865 - \lambda}{100}\right]. \qquad (29)$$

With these changes, the retrieved results are significantly improved by using the updated aerosol look-up tables (Robinson et al. 2000).

8.4 TRANSMITTANCE TABLES

Because the $t(\lambda)$ values depend on the aerosol models, it is necessary to update the transmittance tables with the updated aerosol models, i.e., including the transmittance tables for the O99 model. In the old tables (prior to August 1998), there was an error in the atmospheric diffuse transmittance tables, in which the Fresnel-reflecting ocean surface was mistakenly not included in the computations. This caused the SeaWiFS-retrieved normalized water-leaving radiance to depend strongly on the SeaWiFS scan angle, in particular, at the SeaWiFS scan edges. This error was corrected in the updated diffuse transmittance tables, and the reprocessing results show the normalized water-leaving radiances now have no obvious dependence on the SeaWiFS scanning angles (R. Eplee, pers. comm.).

8.5 WHITECAP CONTRIBUTIONS

As discussed in Sect. 8.2, the foam contribution in the SeaWiFS imagery is estimated by using a reflectance model (Koepke 1984) based on the sea-surface wind speed (Gordon and Wang 1994b). It is assumed that the foam is white, i.e., the whitecap reflectance is independent of wavelength. The *in situ* measurements, however, show a significant uncertainty in $\rho_f(\lambda)$ with the sea-surface wind speed (e.g., Monahan 1971). The measurement data are particularly noisy for sea-surface wind speeds greater than 7–$8 \, \mathrm{m \, s^{-1}}$ wherein the uncertainty is usually greater than 100% (Fig. 1 in Gordon and Wang 1994b).

In recent studies, both Frouin et al. (1996) and Moore et al. (1998) found that contrary to the previous measurements, the whitecap reflectance is spectrally dependent. The reflectance contributions are significantly smaller at the near-infrared than in the visible spectrum, because of the stronger ocean water absorption at the longer wavelengths. This reduces the reflected photons from the submerged bubbles. The SeaWiFS observations also show that the whitecap reflectance model, used in the atmospheric corrections, likely overestimated the whitecap contributions significantly, in particular, for the larger sea-surface wind speed. The overcorrection was particularly evident in very clear open ocean scenes with high surface wind, which resulted in low normalized water-leaving radiance retrievals.

The SeaWiFS Project has adopted the Frouin et al. (1996) results (with updates) for the spectral dependence, and the results from Moore et al. 2000) for the magnitude of the whitecap contributions. This leads to a reduction in the whitecap radiance contributions for SeaWiFS bands 1–8 by factors of 0.4, 0.4, 0.4, 0.4, 0.4, 0.3557, 0.3040, and 0.2580, respectively, relative to the values estimated using Gordon and Wang (1994b). The whitecap radiance for
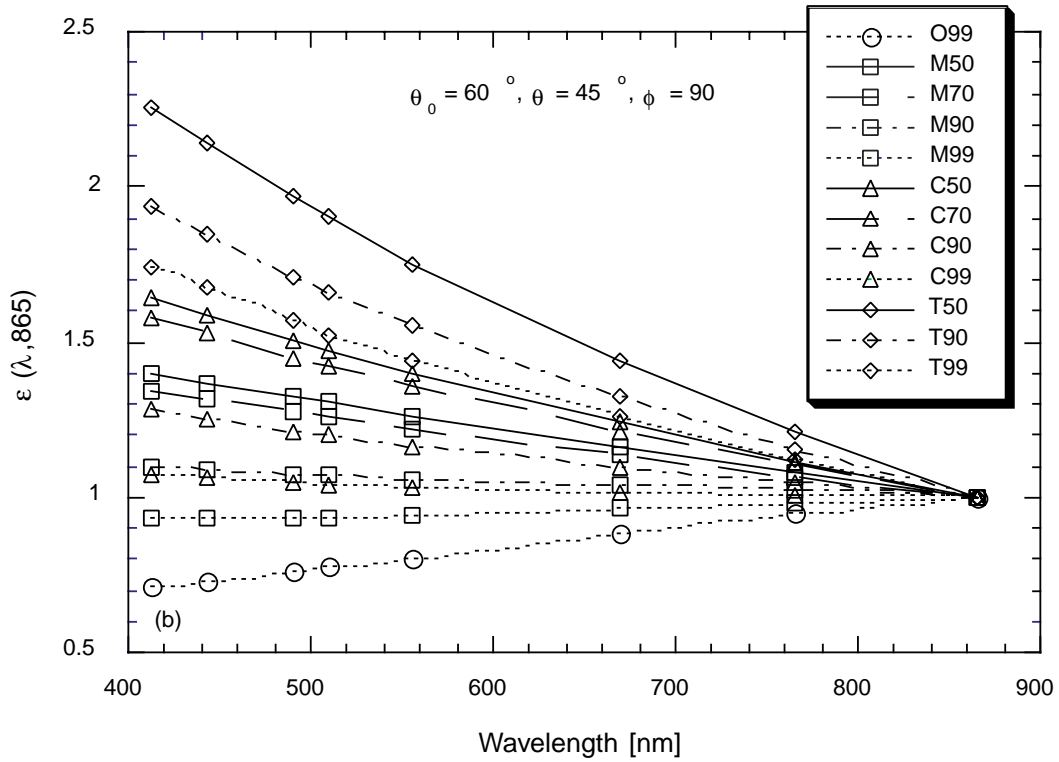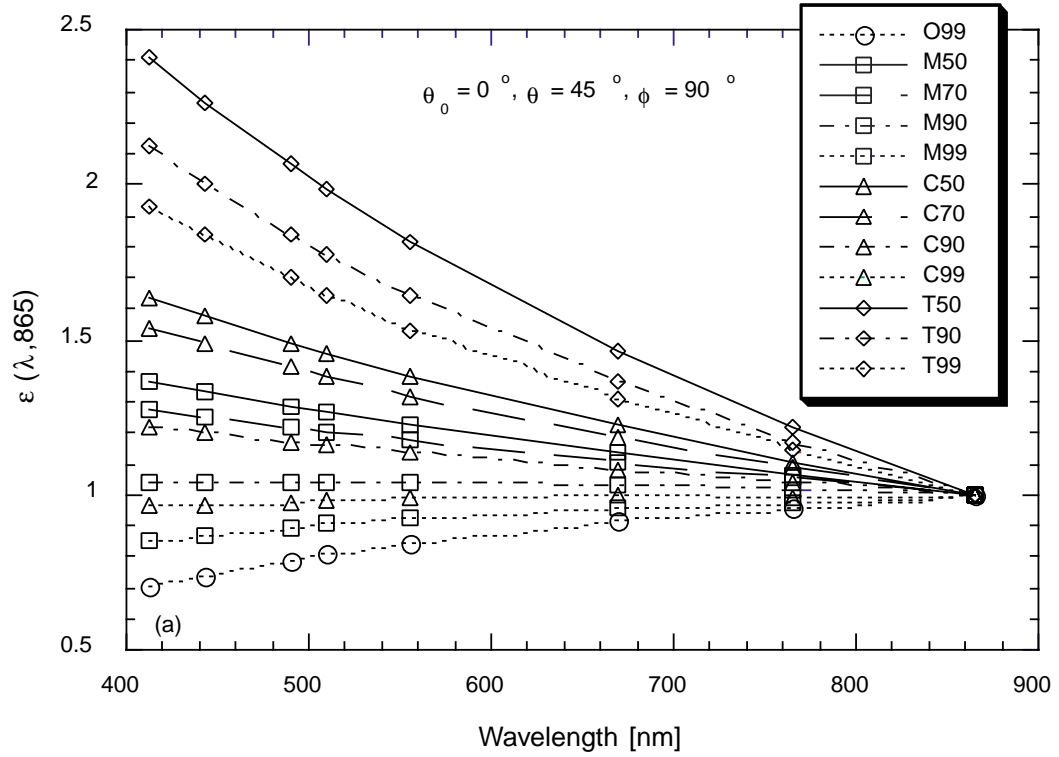
Fig. 36. The $\epsilon(\lambda, 865)$ value as a function of wavelength λ, for the 12 aerosol models used in the updated aerosol look-up tables for the sensor zenith angle of $\theta = 45°$, and the solar zenith angle of **a)** $\theta_0 = 0°$ and **b)** $\theta_0 = 60°$.
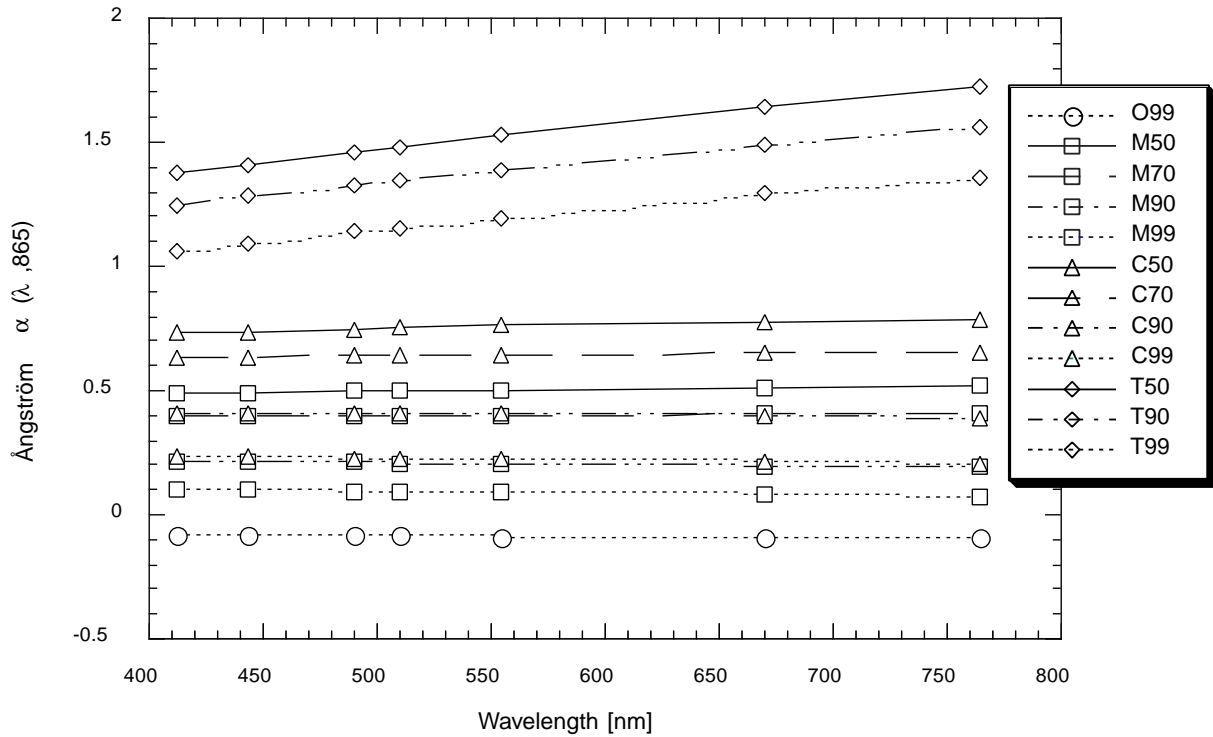
Fig. 37. The $\epsilon(\lambda, 865)$ value as a function of wavelength λ, for the SeaWiFS updated 12 aerosol models.

wind speeds greater than $8 \, \mathrm{m \, s^{-1}}$ are set equal to the value computed at $8 \, \mathrm{m \, s^{-1}}$. Results from *in situ* measurements showed similar characteristics (Moore et al. 2000). It is believed, however, that some validation efforts with more experimental data are needed to further fine tune the foam reflectance model. In addition, evaluations of the National Center for Environmental Prediction (NCEP) wind speeds using buoy winds near Hawaii and Bermuda show very good agreement, and differences between SeaWiFS and the Bermuda Test Bed Mooring (BTBM) water-leaving radiances were uncorrelated to wind speed (S. Bailey, pers. comm.) which suggests the $8 \, \mathrm{m \, s^{-1}}$ limit is not introducing a bias in the SeaWiFS products. In fact, it is better to underestimate foam radiance than to overestimate it (Gordon and Wang 1994b), because the residual will be included in the aerosol radiance.

8.6 NEW RAYLEIGH TABLES

New Rayleigh radiance look-up tables for the SeaWiFS bands were generated using the method developed by Gordon and Wang (1992) for the various ocean surface wind speeds. A bidirectionally shadowing factor for a collection of individual wind-ruffled facets (Gordon and Wang 1992) was used in all computations. These new wind speed dependent Rayleigh tables were implemented in the third reprocessing. Prior to the third reprocessing, Rayleigh tables were generated with a flat ocean surface assumption (where the wind speed was zero). The Rayleigh radiance tables were generated at eight ocean surface wind speeds corresponding to 0, 1.9, 4.2, 7.5, 11.7, 16.9, 22.9, and $30.0 \, \mathrm{m \, s^{-1}}$,

respectively. Tests showed that, with the new Rayleigh tables, the SeaWiFS-derived ocean color products are significantly improved, in particular, for cases of the larger solar zenith angles, i.e., $\theta_0 > 60°$. A detailed study for the effects of the surface roughness on the SeaWiFS derived ocean color products is currently underway.

8.7 ÅNGSTRÖM EXPONENT

The aerosol Ångström exponent is widely used in the atmospheric aerosol and radiation communities. For two wavelengths at λ_i and λ_j, the Ångström exponent is defined as

$$\frac{\tau_a(\lambda_i)}{\tau_a(\lambda_j)} \;=\; \left[\frac{\lambda_j}{\lambda_i}\right]^{\alpha(\lambda_i, \lambda_j)}, \qquad (30)$$

or

$$\alpha(\lambda_i, \lambda_j) \;=\; \frac{\ln\left[\frac{\tau_a(\lambda_i)}{\tau_a(\lambda_j)}\right]}{\ln\left[\frac{\lambda_j}{\lambda_i}\right]}, \qquad (31)$$

where $\tau_a(\lambda_i)$ and $\tau_a(\lambda_j)$ are aerosol optical thicknesses measured at λ_i and λ_j, respectively. The Ångström exponent, which is independent of the solar and viewing geometry, can be used to relate the aerosol microphysical properties (particle size) and its optical spectral dependence. Figure 37 provides values of $\alpha(\lambda, 865)$ as a function of wavelength, λ, for the 12 SeaWiFS updated aerosol models. Apparently, the $\alpha(\lambda, 865)$ value is nearly independent of the wavelength, in particular for the oceanic, maritime, and coastal aerosol models.

With the two retrieved aerosol models in the atmospheric correction process, the SeaWiFS $\alpha(\lambda_i, 865)$ can be easily derived:

$$\alpha(\lambda_i, 865) \;=\; (1-r)\,\alpha^a(\lambda_i, 865) \;+\; r\,\alpha^b(\lambda_i, 865), \quad (32)$$

where $\alpha^a(\lambda_i, 865)$ and $\alpha^b(\lambda_i, 865)$ are, respectively, the Ångström exponent from derived models a and b, and r is the ratio between two aerosol models from the retrieved ϵ values. The SeaWiFS $\alpha(\lambda_i, 865)$ retrieval routine can be very easily implemented in the SeaWiFS data processing.

It was decided that the $\alpha(510, 865)$ data will be routinely retrieved and archived. The reasons for choosing the 510 nm channel are that it is closely matched with the ground *in situ* measurement data (e.g., AERONET data) and it gives a good approximation to be used in deriving aerosol optical thickness at other SeaWiFS wavelengths (e.g., 412 nm). Nevertheless, the SeaDAS code can be easily modified to obtain $\alpha(\lambda_i, 865)$ in any of the SeaWiFS wavelengths.

Chapter 9

Correction of the Sun Glint Contamination on the SeaWiFS Aerosol Optical Thickness Retrievals

Menghua Wang

University of Maryland Baltimore County
Baltimore, Maryland

Sean W. Bailey

Futuretech Corporation
Greenbelt, Maryland

Abstract

For ocean color remote sensing, the measurement of radiances affected by sun glint has to be avoided or masked out. SeaWiFS has a capability of operationally tilting the sensor 20° away from nadir to minimize sun glint contamination, however, sun glint is still a factor near the subsolar point. In this chapter, results are presented which quantify the effect of sun glint contamination on the retrievals of atmospheric and bio-optical oceanic products. It was found that, although the sun glint contamination has a minor effect on the retrieved bio-optical oceanic products, the effect on the retrieved atmospheric products (e.g., aerosol optical thickness) is significant. A sun glint correction scheme is described, which was implemented in the SeaWiFS data processing. It was found that the sun glint correction significantly improves the derived atmospheric products in the vicinity of the subsolar point.

9.1 INTRODUCTION

In ocean color remote sensing, the radiance measured at the top of the ocean-atmosphere system can be written as stated in (13),

$$
\begin{aligned}
L_t(\lambda) \ = \ & L_r(\lambda) \ + \ L_a(\lambda) \\
& + \ L_{ra}(\lambda) \ + \ T(\lambda)L_g(\lambda) \\
& + \ t(\lambda)L_f(\lambda) \ + \ t(\lambda)L_W(\lambda),
\end{aligned}
\tag{33}
$$

where $L_r(\lambda)$, $L_a(\lambda)$, and $L_{ra}(\lambda)$ are the radiance contributions from multiple scattering of air molecules (Rayleigh scattering), aerosols, and Rayleigh-aerosol interactions, respectively (Gordon and Wang 1994a). $L_g(\lambda)$ is the specular reflection from the direct sun (sun glint) radiance, $L_f(\lambda)$ is the radiance at the sea surface resulting from sunlight and skylight reflecting off foam (or whitecaps) on the surface (Gordon and Wang 1994b), and $L_W(\lambda)$ is the water-leaving radiance. $T(\lambda)$ and $t(\lambda)$ are the atmospheric direct and diffuse transmittances at the sensor viewing direction, respectively.

As there are usually no meaningful retrievals in the regions contaminated by sun glint, measurement of radiances affected by sun glint have to be avoided or masked out. SeaWiFS has the capability of operationally tilting

the sensor 20° away from nadir to minimize sun glint contamination. Sun glint is still a factor, however, in the vicinity of the subsolar point. The SeaWiFS processing system computes $L_g(\lambda)$ from the Cox and Munk (1954) model based on the sea surface wind speed. A mask is applied to areas where the glint radiance is greater than a predetermined threshold. Although the regions with the most significant sun glint contamination are masked out, there is still some residual sun glint contamination surrounding the mask. The sun glint contamination is particularly evident in the SeaWiFS derived atmospheric products, e.g., aerosol optical thickness. It is important, therefore, to develop a correction scheme for removing the effects of sun glint contamination. The ocean pigment concentration, however, is usually less affected by sun glint contamination, because the bio-optical algorithm uses a two-band ratio value in the derived water-leaving radiances (Fraser et al. 1997).

In this chapter, the SeaWiFS sun glint mask from Cox and Munk (1954) is briefly described. Then, a sun glint contamination correction scheme and its implementation in the SeaWiFS data processing are proposed. Next, evaluations of the NCEP wind speed data are presented, which are used in the SeaWiFS data processing in comparison with *in situ* measurements. Finally, some comparison results are presented with and without sun glint corrections.

9.2 THE SeaWiFS SUN GLINT MASK

It is convenient to rewrite the sun glint radiance as:

$$L_g(\lambda) = F_0(\lambda) T_0(\lambda) L_{GN}, \qquad (34)$$

where $F_0(\lambda)$ is the solar irradiance (adjusted for Earth–sun distance variations), $T_0(\lambda)$ is the atmospheric direct transmittance in the solar direction, and L_{GN} is the normalized sun glint radiance, i.e., the value of L_g if there were no atmosphere and $F_0(\lambda) = 1$. Note that for a given pixel, the L_{GN} value depends on the solar and viewing geometry, the sea surface wind speed, and the wind direction.

The L_{GN} term is computed based on the assumption that the wind-roughened sea surface consists of a collection of individual facets obeying the Cox and Munk (1954) slope statistics. As an approximation, L_{GN} is computed with a further assumption that the wind-roughened surface slope distribution is independent of the wind direction. The inputs for the computation are, at a pixel-by-pixel level, the solar and sensor viewing geometry, as well as the surface wind speed. The computed L_{GN} value is used as the sun glint mask and is applied to areas where the glint radiance is greater than a predetermined threshold.

In the SeaWiFS data processing, the pixels for which $L_{GN} \geq 0.005$ are masked, and no further calculations for retrieving oceanic or atmospheric products occurs (McClain et al. 1995). There are also no corrections applied for pixels for which $0 < L_{GN} < 0.005$, so it is likely that there will be some sun glint contamination outside the sun glint mask. It has been found that there is no apparent bias in the SeaWiFS retrieved oceanic products (e.g., water-leaving radiances and chlorophyll concentration) around the subsolar point, but the derived aerosol optical thicknesses are always biased high in regions where $0 < L_{GN} < 0.005$. To improve the SeaWiFS atmospheric products, sun glint contamination needs to be corrected.

9.3 SUN GLINT CONTAMINATION

If L_g is known (34), it can be subtracted from the sensor-measured radiances (33), and subsequent data processing is based on the corrected radiances:

$$\begin{aligned} \hat{L}_t &= L_r(\lambda) + L_a(\lambda) + L_{ra}(\lambda) \\ &\quad + t(\lambda) L_f(\lambda) + t(\lambda) L_W(\lambda), \end{aligned} \qquad (35)$$

where $\hat{L}_t$ is the sun glint corrected radiance, which is defined as $L_t(\lambda) - F_0(\lambda) T_0(\lambda) T(\lambda) L_{GN}$, and

$$T_0(\lambda) T(\lambda) = \exp\left[-\big(\tau_r(\lambda) + \tau_a(\lambda)\big) \right. \\ \left. \left(\frac{1}{\cos\theta_0} + \frac{1}{\cos\theta} \right) \right]. \qquad (36)$$

The $\tau_r(\lambda)$ and $\tau_a(\lambda)$ terms in (36) are the optical thickness for Rayleigh (air molecules) and aerosols, respectively, and θ_0 and θ correspond to the solar and sensor zenith angles, respectively. It is assumed that the ozone absorption effects in (35) and (36) have been removed. The sun glint corrected radiance, $\hat{L}_t$, at the eight SeaWiFS bands can then be inserted into the atmospheric correction algorithm, replacing $L_t(\lambda)$, and data processing can proceed with corrected radiances.

At the time of data processing, the aerosol optical thickness in (36) is unknown, so an iterative scheme is proposed. The sun glint corrected radiance, $\hat{L}_t$, is first calculated with the uncorrected L_t, wind speed, and an initial guess for τ_a [used here as $\tau_a'(\lambda_i)$]. The initial $\hat{L}_t$ is then used to derive τ_a which is then used as the input to derive the *final* sun glint corrected radiance and the *final* sun glint corrected aerosol optical thickness.

Based on results from some case studies, the $\tau_a'(\lambda_i)$ values are estimated using the following steps:

a) L_{GN} is computed using the Cox and Munk (1954) model;

b) Setting $\tau_a(865) = 0.1$ (which is the global average value from SeaWiFS) in (36), $L_A = L_a + L_{ra}$ at the SeaWiFS 865 nm band in (35) can be derived and then converted to the aerosol reflectance using $\rho_A = \pi L_A / F_0 \cos\theta_0$; and

c) A high $\tau_a'(\lambda_i)$ value is used for a low ρ_A value (i.e., a $\tau_a'(865)$ with values of 1.0, 0.4, 0.2, and 0.12 are used, corresponding to ρ_A of 0.001, 0.005, 0.008, and 0.01, respectively).

The reason for using the large $\tau_a'(865)$ values for the low ρ_A cases is to avoid the overcorrection of the sun glint contamination due to uncertainties in the L_{GN} estimation. These uncertainties arise from either uncertainty in surface wind speed or limitations of the Cox and Munk (1954) model, i.e., for the cases of small ρ_A values (less than approximately 0.005 corresponding to $\tau_a <\approx 0.05$), confidence in the sun glint correction is low.

9.4 WIND SPEED DATA EVALUATION

To compute L_{GN}, the sea surface wind speed is needed. Based on a study and recommendation by Firestone et al. (1994), SeaWiFS uses the surface wind speed data provided by NCEP which is gridded at 1°. The SeaWiFS data processing interpolates this coarse wind data to the SeaWiFS 1 km pixel. Because the Cox and Munk (1954) model is sensitive to wind speed, some evaluations of the NCEP data were conducted. NCEP winds were compared to winds measured at the BTBM. Figure 38 provides an example scatter plot for the NCEP winds versus the *in situ* buoy data. The two data sets agreed reasonably well and there was no obvious bias of the NCEP wind data. This result lends confidence to the use of the interpolated NCEP winds in the L_{GN} calculation.
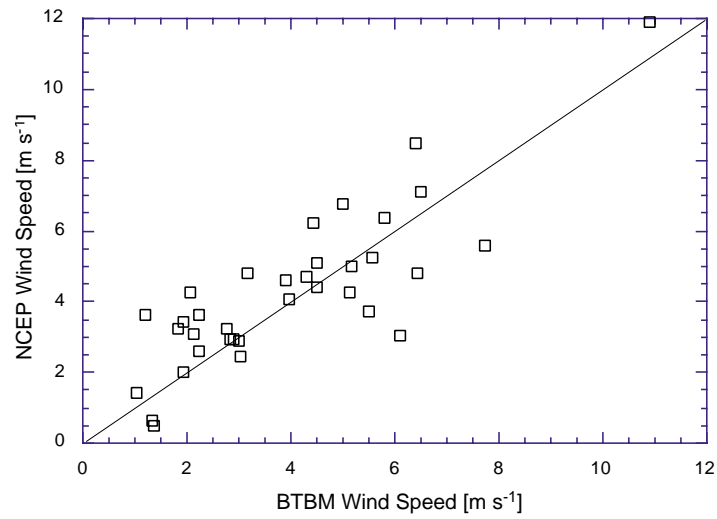
Fig. 38. NCEP surface wind speed data compared with the *in situ* buoy measurements at the BTBM.
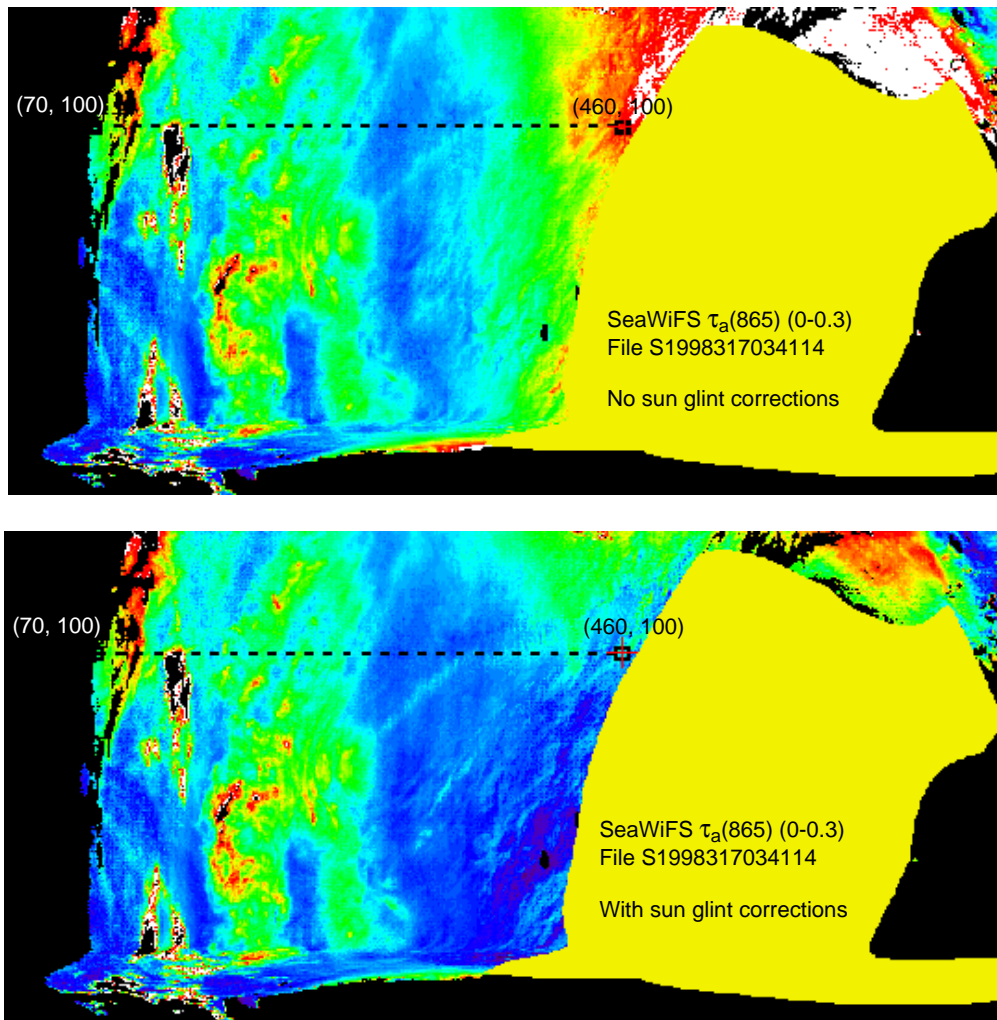
Fig. 39. The SeaWiFS derived $\tau_a(865)$ values for cases without (top panel) and with (bottom panel) the sun glint corrections.
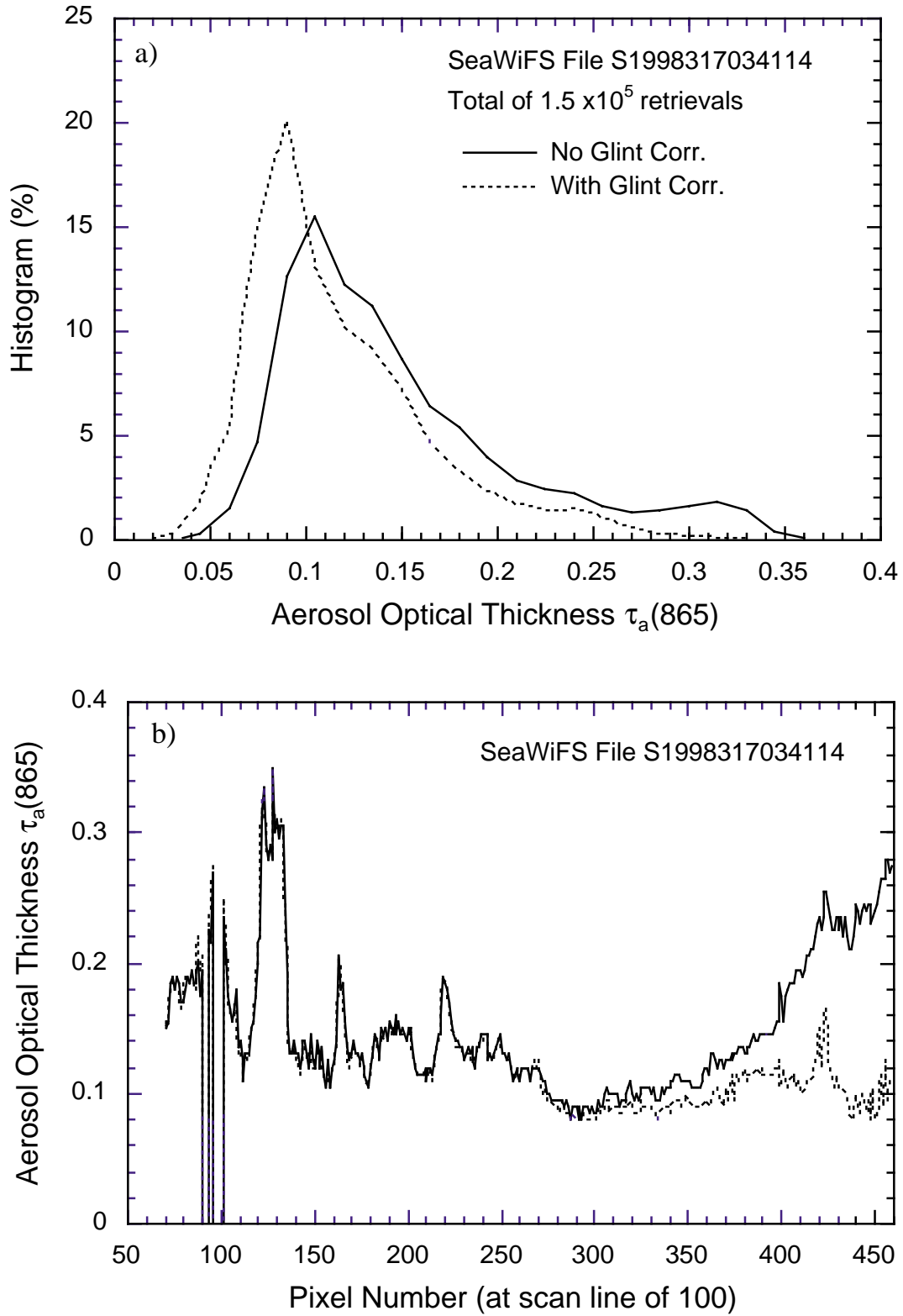
Fig. 40. A quantitative comparison of the SeaWiFS derived $\tau_a(865)$ values for cases with and without sun glint contamination corrections: **a)** histograms from the results in Fig. 39, and **b)** data from pixels 70–460 at scan line 100 (dashed line in Fig. 39).

9.5 RESULTS

To assess the efficacy of the proposed sun glint correction scheme, some case studies were conducted. Figure 39 provides an example of the SeaWiFS $\tau_a(865)$ images for cases with and without sun glint corrections. SeaWiFS data (file name S1998317034114) was acquired on 13 November 1998 along the west coast of Australia at the location around $-24°$ latitude and $120°$ longitude. The image in the top panel was processed without the sun glint correction, while the bottom image was processed with the correction applied. The value of $\tau_a(865)$ is scaled from 0–0.3. The sun glint mask (right side part of image, gray-white color) in Fig. 39 is clearly seen. In comparing two $\tau_a(865)$ images, it can be seen that the derived aerosol optical thickness is reduced around the area outside the glint mask when the correction is applied.

Figures 40a and 40b show results of a quantitative comparison of these two images. Figure 40a compares the histograms from the two cases, while Fig. 40b compares a specific scan line (the dashed line in each image in Fig. 39). Figure 40a shows that, with the sun glint corrections, the large $\tau_a(865)$ values, which correspond to the sun glint contamination regions, are much reduced. The sun glint contamination effects are clearly seen in Fig. 40b where the $\tau_a(865)$ is obviously biased, increasing as the pixel numbers increase (close to the glint mask region) for cases without the sun glint corrections. The $\tau_a(865)$ values are much more reasonable with the sun glint contamination correction applied.

The effects of sun glint contamination on the oceanic optical products were also studied. It was found that there is almost no effect on the SeaWiFS retrieved ocean products, e.g., normalized water-leaving radiances and chlorophyll concentration.

Chapter 10

Modifications to the TOMS Ozone Ancillary Data Interpolation

EWA J. AINSWORTH AND FREDERICK S. PATT

SAIC General Sciences Corporation
Beltsville, Maryland

ABSTRACT

The method for interpolating the TOMS ozone data used for level-2 processing was changed as a result of new information about the generation of the files by the TOMS Project. The new method and comparison of the old and new results are described in this report.

10.1 INTRODUCTION

The interpolation of ancillary meteorological and ozone data used for level-2 processing is made in two steps. Gridded ancillary counts are spatially and temporally approximated for all pixels within a SeaWiFS swath. The interpolation in space uses rectangular bilinear approximation. The interpolation in time follows the spatial interpolation and applies a simple linear approximation.

The ozone interpolation employs gridded equidistant cylindrical maps of ozone obtained by TOMS and the Television Infrared Observation Satellite (TIROS) Operational Vertical Sounder (TOVS) instruments. Previously, all ancillary data files [NCEP, TOMS ozone, and the TOVS ozone] were assumed to be generated as global gridded files for fixed epochs, so that the entire file could be assumed to have the same time tag. For the TOMS data, a single file was generated for each GMT day, so the time tag was assumed to be 1200 UTC on the day. In recent discussions with the TOMS Project, it was learned that the TOMS ozone data are actually generated in a similar manner to the SeaWiFS level-3 binned products, in that the data are gridded for whatever time (or times) the sensor viewed the locations on that day. In addition, the TOMS satellite orbit has a local noon descending node, like that of SeaWiFS, so the observation times for SeaWiFS and TOMS are fairly close (within approximately 1/2 orbit).

Based on the above, it was decided to change the TOMS ozone data interpolation to reflect the actual observation times for the gridded data, which varies linearly from 0000 UTC at 180° longitude, to 0000 UTC at −180°. The interpolation for the other ancillary data types remains unchanged. Figure 41 shows an example of a TOMS daily map with the latitude and longitude, and starting and ending times for the four corners of the grid. The latitudinal distance between consecutive grid points is 1.0°

and the longitudinal distance between the grid points is 1.25°. Ozone maps are, therefore, composed of 180 points in the vertical direction and 288 points in the horizontal direction.

Three TOMS or TOVS files are normally submitted for spatial and temporal approximation of ancillary ozone data for a whole SeaWiFS swath. Two files out of the three are used at the ancillary ozone approximation of each SeaWiFS scan line. This chapter describes the modification introduced to the temporal approximation of TOMS ozone ancillary data. The modification calculates the true time for each ozone grid point based on information provided within a TOMS file header.

10.2 NEW OZONE SCHEME

The linear function of time in terms of longitude for TOMS ozone files is given in Fig. 42. The function can be written as

$$T_T = \frac{(T_s - T_e)X}{360.0} + \frac{T_s + T_e}{2.0}, \qquad (37)$$

where T_T is the (sequential day of the year) time of a TOMS ozone observation along a given longitude, X is the corresponding longitude, and T_s and T_e are the (sequential day of the year) start, and end times, respectively, of the TOMS file.

The modified temporal approximation of TOMS ozone ancillary data applies the difference, ΔT, between the time of the SeaWiFS observation of the current scan line and the TOMS time associated with the corresponding longitude for each scan line pixel (ΔT^N):

$$\Delta T^N = |T_c - T_T|, \qquad (38)$$

lat   89.5
lon -179.375
time 1999.323.23:59:5999

lat   89.5
lon 179.375
time 1999.323.0:0:0
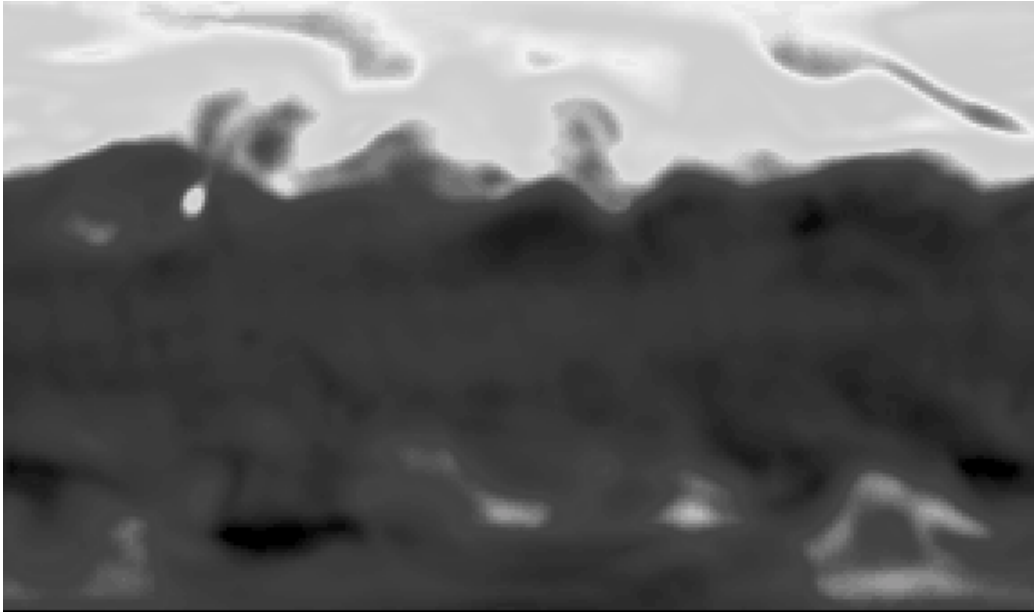
lat   -89.5
lon -179.375
time 1999.323.23:59:5999

lat   -89.5
lon 179.375
time 1999.323.0:0:0

Fig. 41. Spatial and temporal characteristics of TOMS ozone files.

Fig. 42. Linear function of time versus longitude for the new scheme of TOMS ozone interpolation.

McClain, Ainsworth, Barnes, Eplee, Patt, Robinson, Wang, and Bailey

Fig. 43. Histograms of ozone differences between the old and new schemes of TOMS approximation for SeaWiFS swaths captured around noon (left panel) and the IDL (right panel).

where T_c is the time of SeaWiFS capture of the present scan line. The same time, T_c, is used for all pixels within a scan line, because the fraction of a second which it takes SeaWiFS to attain the complete scan line can be neglected in the calculations.
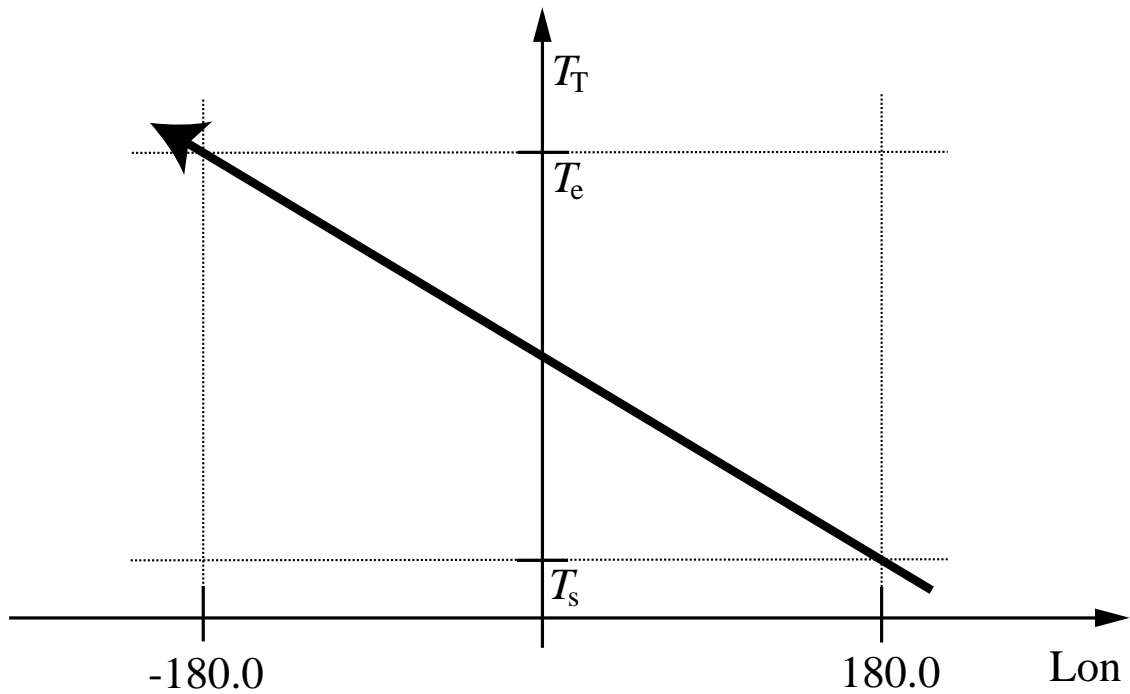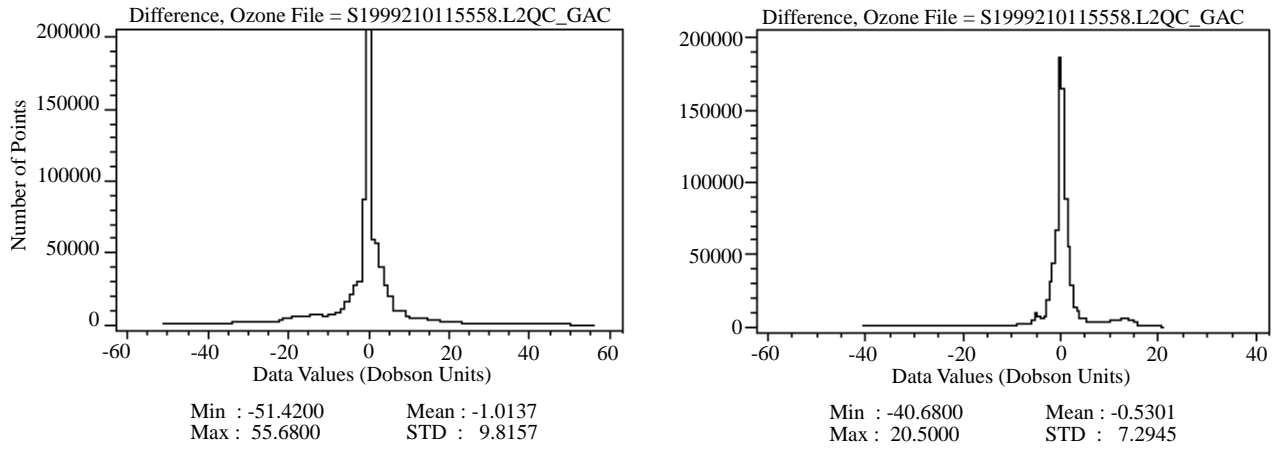
The old temporal approximation defined ΔT as a difference of scan line time from the beginning of the TOMS file:

$$\Delta T^O = |T_c - T_s|, \tag{39}$$

Although the old interpolation scheme (ΔT^O) assumed the T_s to be 1200 UTC for an entire daily ozone map, it was reading the actual T_s value from the TOMS file header which returned the time around 0000 UTC.

Temporal approximation computes weights for ozone grid points on the corners of the cell which spatially encompasses a SeaWiFS scan line point. The weights are calculated for both ancillary TOMS files used in the interpolation, W_1 and W_2 for the first and second file, respectively. Two ΔT values (ΔT_1 and ΔT_2) for each file are in the same way converted into weights for the old and new processing:

$$W_1 = \frac{\Delta T_2}{\Delta T_1 + \Delta T_2}, \tag{40}$$

and

$$W2 = \frac{\Delta T_1}{\Delta T_1 + \Delta T_2}. \tag{41}$$

The final interpolation equation is as follows:

$$F_i = W_1 F_1 + W_2 F_2, \tag{6}$$

where F_i is the interpolated ozone value and F_1 and F_2 are spatially approximated ozone values within the TOMS first and second file, respectively.

The new approximation puts the highest weight on ozone grid cells from the ancillary file that is most concurrent with the given scan line point. A low weight is given to ozone grid cells from the other ancillary file later

in time. A switch of ancillary files takes place when a scan line crosses the International Date Line (IDL). The old approximation algorithm allocates a higher weight to ozone grid cells from the ancillary file whose start time is the closest to the scan line time which gives greater weight to the nonconcurrent ozone counts at the start of the TOMS map.

Coincident TOMS and SeaWiFS acquisition times results in progressively low ΔT for ozone grid cells from the ancillary file that is most concurrent with scan line points. The new algorithm works well for all ancillary file data captured over a period of time, such as TOMS ozone where $T_e - T_s \approx 24$ h. It is also appropriate for ancillary data where the common time for the whole file is mid-time, T_m, and $T_m = T_e = T_s$. The general concept of the method, therefore, could also be applied to other ancillary files, such as TOVS. Currently, the new processing only activates when there are two ancillary files submitted to the approximation of a scan line and both are TOMS ozone.

10.3 RESULTS

The new TOMS ozone approximation scheme introduces noticeable differences for SeaWiFS swaths in both ozone content and chlorophyll concentration. The modified algorithm was executed on eight-day data and produced level-2 products. A two-day run produced level-2 and quality control products for both conventional and altered algorithms of TOMS ozone approximation.

10.3.1 Ozone Comparison

Old and modified TOMS ozone approximation schemes were compared. There was a substantial difference in ozone counts both with over- and underestimation. Figure 43 compares histograms based on the ozone value differences between the old and new schemes for a near-noon and near-midnight (near the IDL) SeaWiFS swaths. Within the entire two-day sequence of SeaWiFS processing, the new
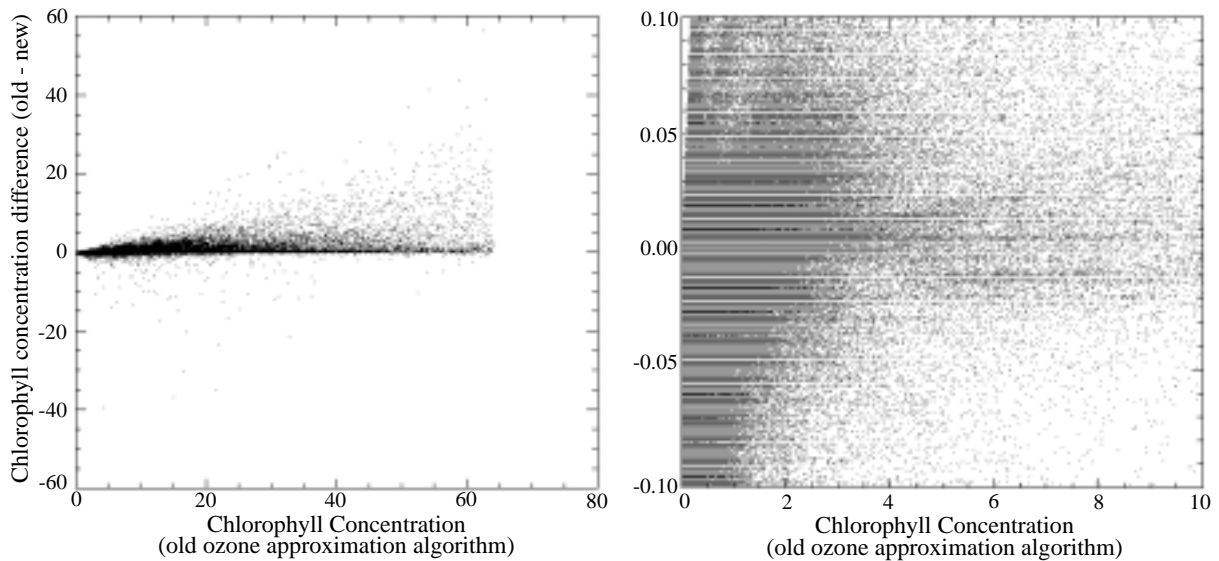
Fig. 44. Scatterplots of two-day chlorophyll concentration values obtained by the old approximation scheme as a function of the chlorophyll level difference between the old and new algorithms.

method of ozone approximation from TOMS files produces a difference of up to 20% from the previous algorithm.

The switch of the concurrent TOMS files along the IDL results in discontinuities in the ozone approximation values. The artifacts are created because successive day-to-day ozone maps do not continuously fall one into another, and the new scheme puts the largest weight on ozone cells located in the most concurrent file causing the switch at the IDL. The amount of the discontinuity reaches up to 12–17%.

10.3.2 Chlorophyll Comparison

The modified algorithm of ozone approximation from TOMS files has caused measurable changes in the chlorophyll concentration values compared to the old method. The results were obtained on SeaWiFS GAC data captured over two days and processed using ozone information calculated according to the old and new scheme of TOMS interpolation. In the comparison of old and new chlorophyll concentration results, only those pixels which were not flagged by either level-2 processing algorithm were considered.

Figure 44 shows two scatterplots of differences in chlorophyll levels produced by the old and new methods as a function of chlorophyll concentration using the old ozone approximation scheme. The first plot shows the full scale of chlorophyll levels and data differences, and the second plot is a magnification of the smaller chlorophyll concentrations and difference values. The scatterplots indicate that there are some isolated pixels for which the difference in chlorophyll levels between the two methods is as high as 100%.

Histograms of chlorophyll concentration differences between the two schemes for a two-day period of SeaWiFS

capture are displayed in Fig. 45. The same data are shown for two ranges of differences in chlorophyll levels. The percentage of significantly changed chlorophyll values is small, therefore, only narrow domains around the zero level of chlorophyll difference can show on the histogram.

Overestimation of chlorophyll levels by the old algorithm is much more common, about 72%, for larger chlorophyll difference values exceeding $0.1\,\mathrm{mg\,m^{-3}}$. Within the lower difference range (below $0.1\,\mathrm{mg\,m^{-3}}$), 74% of counts are underestimated by the old method in comparison with the new scheme.

The overwhelming majority (96.8%) of chlorophyll concentration variances between the two methods account for chlorophyll level differences smaller than $0.1\,\mathrm{mg\,m^{-3}}$. This value could be nonetheless significant, as the chlorophyll concentration of much of the global ocean is in the range of $0.1\,\mathrm{mg\,m^{-3}}$. The bulk of chlorophyll changes, 70%, is below $0.01\,\mathrm{mg\,m^{-3}}$.

The discontinuity of new ozone approximation along the IDL is not visually discernible even in rescaled chlorophyll concentration images. The difference can only be observed in comparison with chlorophyll counts obtained with the old method of ozone approximation. Within the limited data set, only intermediate chlorophyll concentration levels around $0.3\,\mathrm{mg\,m^{-3}}$ were observed for the IDL regions. The differences between the two algorithms in these areas can be estimated up to 20% for either side of the IDL.

10.4 CONCLUSIONS

A new algorithm for the temporal interpolation of ancillary TOMS ozone data was needed to reflect the actual observation times for TOMS gridded maps. The new scheme

Min : -39.2850	Mean : -0.00143761
Max : 56.4080	STD : 0.244098
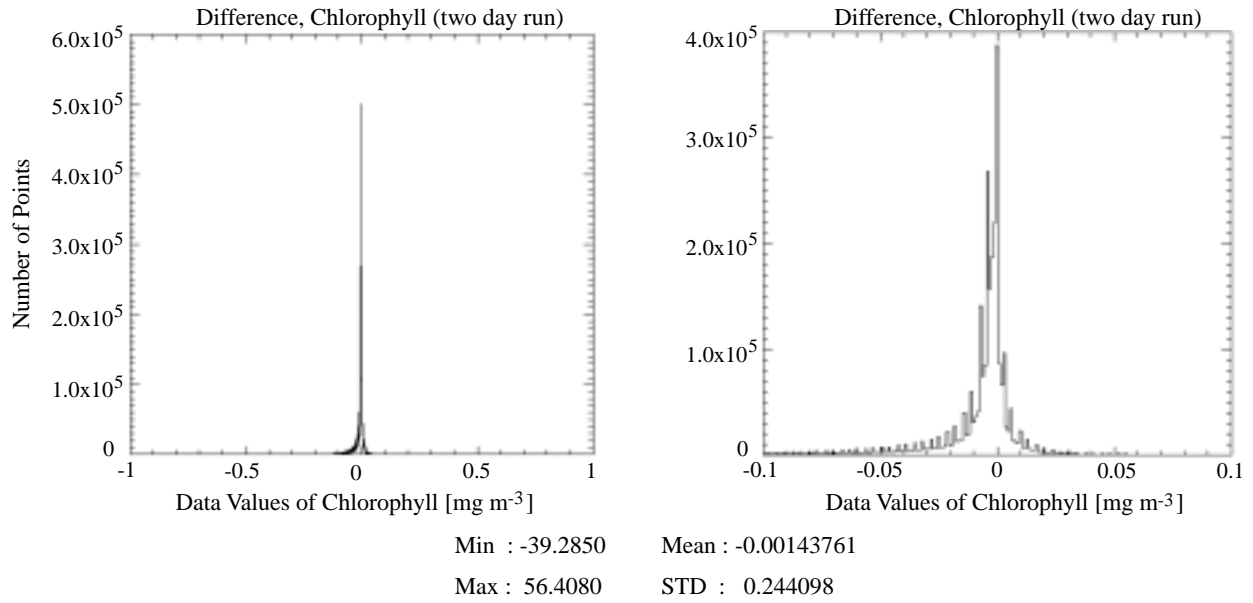
Fig. 45. Histograms of differences in chlorophyll concentrations between chlorophyll levels obtained using the old and new ozone approximation schemes for two days of SeaWiFS data.

introduces measurable differences in chlorophyll concentration counts compared to the old algorithm. In 96.8% of the cases considered, however, the change in chlorophyll concentration is below $0.1\,\mathrm{mg\,m^{-3}}$, and in 70% of the cases, the change is below $0.01\,\mathrm{mg\,m^{-3}}$. Within the 3.2% range of cases, there are some isolated occurrences when the new method causes a large variation in chlorophyll readings reaching as much as 100%.

Appendices

Appendix A

Cited Volumes

The following is a listing of the volumes in the *SeaWiFS Technical Report Series* (Prelaunch) and the *SeaWiFS Postlaunch Technical Report Series* cited in Table 1.

SeaWiFS Technical Report Series (Prelaunch)

Vol. 5
Mueller, J.L., and R.W. Austin, 1992: Ocean Optics Protocols for SeaWiFS Validation. *NASA Tech. Memo. 104566, Vol. 5,* S.B. Hooker and E.R. Firestone, Eds., NASA Goddard Space Flight Center, Greenbelt, Maryland, 43 pp.

Vol. 13
McClain, C.R., K.R. Arrigo, J. Comiso, R. Fraser, M. Darzi, J.K. Firestone, B. Schieber, E-n. Yeh, and C.W. Sullivan, 1994: Case Studies for SeaWiFS Calibration and Validation, Part 1. *NASA Tech. Memo. 104566, Vol. 13,* S.B. Hooker and E.R. Firestone, Eds., NASA Goddard Space Flight Center, Greenbelt, Maryland, 52 pp., plus color plates.

Vol. 14
Mueller, J.L., 1993: The First SeaWiFS Intercalibration Round-Robin Experiment, SIRREX-1, July 1992. *NASA Tech. Memo. 104566, Vol. 14,* S.B. Hooker and E.R. Firestone, Eds., NASA Goddard Space Flight Center, Greenbelt, Maryland, 60 pp.

Vol. 16
Mueller, J.L., B.C. Johnson, C.L. Cromer, J.W. Cooper, J.T. McLean, S.B. Hooker, and T.L. Westphal, 1994: The Second SeaWiFS Intercalibration Round-Robin Experiment, SIRREX-2, June 1993. *NASA Tech. Memo. 104566, Vol. 16,* S.B. Hooker and E.R. Firestone, Eds., NASA Goddard Space Flight Center, Greenbelt, Maryland, 121 pp.

Vol. 18
Firestone, E.R., and S.B. Hooker, 1995: SeaWiFS Technical Report Series Cumulative Index: Volumes 1–17. *NASA Tech. Memo. 104566, Vol. 18,* S.B. Hooker and E.R. Firestone, Eds., NASA Goddard Space Flight Center, Greenbelt, Maryland, 47 pp.

Vol. 19
McClain, C.R., R.S. Fraser, J.T. McLean, M. Darzi, J.K. Firestone, F.S. Patt, B.D. Schieber, R.H. Woodward, E-n. Yeh, S. Mattoo, S.F. Biggar, P.N. Slater, K.J. Thome, A.W. Holmes, R.A. Barnes, and K.J. Voss, 1994: Case Studies for SeaWiFS Calibration and Validation, Part 2. *NASA Tech. Memo. 104566, Vol. 19,* S.B. Hooker, E.R. Firestone, and J.G. Acker, Eds., NASA Goddard Space Flight Center, Greenbelt, Maryland, 73 pp.

Vol. 20
Hooker, S.B., C.R. McClain, J.K. Firestone, T.L. Westphal, E-n. Yeh, and Y. Ge, 1994: The SeaWiFS Bio-Optical Archive and Storage System (SeaBASS), Part 1. *NASA Tech. Memo. 104566, Vol. 20,* S.B. Hooker and E.R. Firestone, Eds., NASA Goddard Space Flight Center, Greenbelt, Maryland, 40 pp.

Vol. 22
Barnes, R.A., W.L. Barnes, W.E. Esaias, and C.R. McClain, 1994: Prelaunch Acceptance Report for the SeaWiFS Radiometer. *NASA Tech. Memo. 104566, Vol. 22,* S.B. Hooker, E.R. Firestone, and J.G. Acker, Eds., NASA Goddard Space Flight Center, Greenbelt, Maryland, 32 pp.

Vol. 23
Barnes, R.A., A.W. Holmes, W.L. Barnes, W.E. Esaias, C.R. McClain, and T. Svitek, 1994: SeaWiFS Prelaunch Radiometric Calibration and Spectral Characterization. *NASA Tech. Memo. 104566, Vol. 23,* S.B. Hooker, E.R. Firestone, and J.G. Acker, Eds., NASA Goddard Space Flight Center, Greenbelt, Maryland, 55 pp.

Vol. 24
Firestone, E.R., and S.B. Hooker, 1995: SeaWiFS Technical Report Series Cumulative Index: Volumes 1–23. *NASA Tech. Memo. 104566, Vol. 24,* S.B. Hooker and E.R. Firestone, Eds., NASA Goddard Space Flight Center, Greenbelt, Maryland, 36 pp.

Vol. 25
Mueller, J.L., and R.W. Austin, 1995: Ocean Optics Protocols for SeaWiFS Validation, Revision 1. *NASA Tech. Memo. 104566, Vol. 25,* S.B. Hooker, E.R. Firestone, and J.G. Acker, Eds., NASA Goddard Space Flight Center, Greenbelt, Maryland, 66 pp.

Vol. 26
Siegel, D.A., M.C. O'Brien, J.C. Sorensen, D.A. Konnoff, E.A. Brody, J.L. Mueller, C.O. Davis, W.J. Rhea, and S.B. Hooker, 1995: Results of the SeaWiFS Data Analysis Round-Robin (DARR-94), July 1994. *NASA Tech. Memo. 104566, Vol. 26,* S.B. Hooker and E.R. Firestone, Eds., NASA Goddard Space Flight Center, Greenbelt, Maryland, 58 pp.

Vol. 27
Mueller, J.L., R.S. Fraser, S.F. Biggar, K.J. Thome, P.N. Slater, A.W. Holmes, R.A. Barnes, C.T. Weir, D.A. Siegel, D.W. Menzies, A.F. Michaels, and G. Podesta, 1995: Case Studies for SeaWiFS Calibration and Validation, Part 3. *NASA Tech. Memo. 104566, Vol. 27,* S.B. Hooker, E.R. Firestone, and J.G. Acker, Eds., NASA Goddard Space Flight Center, Greenbelt, Maryland, 46 pp.

Vol. 28
McClain, C.R., K.R. Arrigo, W.E. Esaias, M. Darzi, F.S. Patt, R.H. Evans, J.W. Brown, C.W. Brown, R.A. Barnes, and L. Kumar, 1995: SeaWiFS Algorithms, Part 1. *NASA Tech. Memo. 104566, Vol. 28,* S.B. Hooker, E.R. Firestone, and J.G. Acker, Eds., NASA Goddard Space Flight Center, Greenbelt, Maryland, 38 pp., plus color plates.

Vol. 31
Barnes, R.A., A.W. Holmes, and W.E. Esaias, 1995: Stray Light in the SeaWiFS Radiometer. *NASA Tech. Memo. 104566, Vol. 31,* S.B. Hooker, E.R. Firestone, and J.G. Acker, Eds., NASA Goddard Space Flight Center, Greenbelt, Maryland, 76 pp.

Vol. 32
Campbell, J.W., J.M. Blaisdell, and M. Darzi, 1995: Level-3 SeaWiFS Data Products: Spatial and Temporal Binning Algorithms. *NASA Tech. Memo. 104566, Vol. 32,* S.B. Hooker, E.R. Firestone, and J.G. Acker, Eds., NASA Goddard Space Flight Center, Greenbelt, Maryland, 73 pp., plus color plates.

Vol. 33

Moore, G.F., and S.B. Hooker, 1996: Proceedings of the First SeaWiFS Exploitation Initiative (SEI) Team Meeting. *NASA Tech. Memo. 104566, Vol. 33,* S.B. Hooker and E.R. Firestone, Eds., NASA Goddard Space Flight Center, Greenbelt, Maryland, 53 pp.

Vol. 34

Mueller, J.L., B.C. Johnson, C.L. Cromer, S.B. Hooker, J.T. McLean, and S.F. Biggar, 1996: The Third SeaWiFS Intercalibration Round-Robin Experiment (SIRREX-3), 19–30 September 1994. *NASA Tech. Memo. 104566, Vol. 34,* S.B. Hooker, E.R. Firestone, and J.G. Acker, Eds., NASA Goddard Space Flight Center, Greenbelt, Maryland, 78 pp.

Vol. 35

Robins, D.B., A.J. Bale, G.F. Moore, N.W. Rees, S.B. Hooker, C.P. Gallienne, A.G. Westbrook, E. Marañón, W.H. Spooner, and S.R. Laney, 1996: AMT-1 Cruise Report and Preliminary Results. *NASA Tech. Memo. 104566, Vol. 35,* S.B. Hooker and E.R. Firestone, Eds., NASA Goddard Space Flight Center, Greenbelt, Maryland, 87 pp.

Vol. 36

Firestone, E.R., and S.B. Hooker, 1996: SeaWiFS Technical Report Series Cumulative Index: Volumes 1–35. *NASA Tech. Memo. 104566, Vol. 36,* S.B. Hooker and E.R. Firestone, Eds., NASA Goddard Space Flight Center, Greenbelt, Maryland, 55 pp.

Vol. 37

Johnson, B.C., S.S. Bruce, E.A. Early, J.M. Houston, T.R. O'Brian, A. Thompson, S.B. Hooker, and J.L. Mueller, 1996: The Fourth SeaWiFS Intercalibration Round-Robin Experiment (SIRREX-4), May 1995. *NASA Tech. Memo. 104566, Vol. 37,* S.B. Hooker and E.R. Firestone, Eds., NASA Goddard Space Flight Center, Greenbelt, Maryland, 65 pp.

Vol. 38

McClain, C.R., M. Darzi, R.A. Barnes, R.E. Eplee, J.K. Firestone, F.S. Patt, W.D. Robinson, B.D. Schieber, R.H. Woodward, and E-n. Yeh, 1996: SeaWiFS Calibration and Validation Quality Control Procedures. *NASA Tech. Memo. 104566, Vol. 38,* S.B. Hooker and E.R. Firestone, Eds., NASA Goddard Space Flight Center, Greenbelt, Maryland, 68 pp.

Vol. 39

Barnes, R.A., E-n. Yeh, and R.E. Eplee, 1996: SeaWiFS Calibration Topics, Part 1. *NASA Tech. Memo. 104566, Vol. 39,* S.B. Hooker and E.R. Firestone, Eds., NASA Goddard Space Flight Center, Greenbelt, Maryland, 66 pp.

Vol. 40

Barnes, R.A., R.E. Eplee, Jr., E-n. Yeh, and W.E. Esaias, 1997: SeaWiFS Calibration Topics, Part 2. *NASA Tech. Memo. 104566, Vol. 40,* S.B. Hooker and E.R. Firestone, Eds., NASA Goddard Space Flight Center, Greenbelt, Maryland, 67 pp.

Vol. 41

Yeh, E-n., R.A. Barnes, M. Darzi, L. Kumar, E.A. Early, B.C. Johnson, and J.L. Mueller, 1997: Case Studies for SeaWiFS Calibration and Validation, Part 4. *NASA Tech. Memo. 104566, Vol. 41,* S.B. Hooker and E.R. Firestone, Eds., NASA Goddard Space Flight Center, Greenbelt, Maryland, 35 pp.

Vol. 43

Firestone, E.R., and S.B. Hooker, 1998: SeaWiFS Prelaunch Technical Report Series Final Cumulative Index. *NASA Tech. Memo. 1998–104566, Vol. 43,* S.B. Hooker and E.R. Firestone, Eds., NASA Goddard Space Flight Center, Greenbelt, Maryland, 69 pp.

SeaWiFS Postlaunch Technical Report Series

Vol. 1

Johnson, B.C., J.B. Fowler, and C.L. Cromer, 1998: The SeaWiFS Transfer Radiometer (SXR). *NASA Tech. Memo. 1998–206892, Vol. 1,* S.B. Hooker and E.R. Firestone, Eds., NASA Goddard Space Flight Center, Greenbelt, Maryland, 58 pp.

Vol. 2

Aiken, J., D.G. Cummings, S.W. Gibb, N.W. Rees, R. Woodd-Walker, E.M.S. Woodward, J. Woolfenden, S.B. Hooker, J-F. Berthon, C.D. Dempsey, D.J. Suggett, P. Wood, C. Donlon, N. González-Benítez, I. Huskin, M. Quevedo, R. Barciela-Fernandez, C. de Vargas, and C. McKee, 1998: AMT-5 Cruise Report. *NASA Tech. Memo. 1998–206892, Vol. 2,* S.B. Hooker and E.R. Firestone, Eds., NASA Goddard Space Flight Center, Greenbelt, Maryland, 113 pp.

Vol. 3

Hooker, S.B., G. Zibordi, G. Lazin, and S. McLean, 1999: The SeaBOARR-98 Field Campaign. *NASA Tech. Memo. 1999–206892, Vol. 3,* S.B. Hooker and E.R. Firestone, Eds., NASA Goddard Space Flight Center, Greenbelt, Maryland, 40 pp.

Vol. 4

Johnson, B.C., E.A. Early, R.E. Eplee, Jr., R.A. Barnes, and R.T. Caffrey, 1999: The 1997 Prelaunch Radiometric Calibration of SeaWiFS. *NASA Tech. Memo. 1999–206892, Vol. 4,* S.B. Hooker and E.R. Firestone, Eds., NASA Goddard Space Flight Center, Greenbelt, Maryland, 51 pp.

Vol. 5

Barnes, R.A., R.E. Eplee, Jr., S.F. Biggar, K.J. Thome, E.F. Zalewski, P.N. Slater, and A.W. Holmes 1999: The SeaWiFS Solar Radiation-Based Calibration and the Transfer-to-Orbit Experiment. *NASA Tech. Memo. 1999–206892, Vol. 5,* S.B. Hooker and E.R. Firestone, Eds., NASA Goddard Space Flight Center, 28 pp.

Vol. 7

Johnson, B.C., H.W. Yoon, S.S. Bruce, P-S. Shaw, A. Thompson, S.B. Hooker, R.E. Eplee, Jr., R.A. Barnes, S. Maritorena, and J.L. Mueller, 1999: The Fifth SeaWiFS Intercalibration Round-Robin Experiment (SIRREX-5), July 1996. *NASA Tech. Memo. 1999–206892, Vol. 7,* S.B. Hooker and E.R. Firestone, Eds., NASA Goddard Space Flight Center, 75 pp.

Vol. 8

Hooker, S.B., and G. Lazin, 2000: The SeaBOARR-99 Field Campaign. *NASA Tech. Memo. 2000–206892, Vol. 8,* S.B. Hooker and E.R. Firestone, Eds., NASA Goddard Space Flight Center, 46 pp.

Vol. 11

O'Reilly, J.E., and 24 Coauthors, 2000: SeaWiFS Postlaunch Calibration and Validation Analyses, Part 3. *NASA Tech. Memo. 2000–206892, Vol. 11,* S.B. Hooker and E.R. Firestone, Eds., NASA Goddard Space Flight Center, 49 pp.

Vol. 13

Hooker, S.B., G. Zibordi, J-F. Berthon, S. Bailey, and C. Pietras, 2000: The SeaWiFS Photometer Revision for Incident Surface Measurement (SeaPRISM) Field Commissioning. *NASA Tech. Memo. 2000-206892, Vol. 13,* S.B. Hooker and E.R. Firestone, Eds., NASA Goddard Space Flight Center, (in press).

Vol. 14

Hooker, S.B., H. Claustre, J. Ras, L. Van Heukelem, C. Targa, D. van der Linde, J-F. Berthon, R. Barlow, and H. Sessions, 2000: The First SeaWiFS HPLC Analysis Round-Robin Experiment (SeaHARRE-1). *NASA Tech. Memo. 2000–206892, Vol. 14,* S.B. Hooker and E.R. Firestone, Eds., NASA Goddard Space Flight Center, Greenbelt, Maryland, (in press).

GLOSSARY

AAOT   *Acqua Alta* Oceanographic Tower
AERONET   Aerosol Robotic Network
AMT   Atlantic Meridional Transect
AU   Astronomical Unit

BATS   Bermuda Atlantic Time-series Study
BRDF   Bidirectional Reflectance Distribution Function
BTBM   Bermuda Test Bed Mooring

CalCOFI   California Cooperative Fisheries Institute
CVT   Calibration and Validation Team
CZCS   Coastal Zone Color Scanner

DAAC   Distributed Active Archive Center

GAC   Global Area Coverage

HDF   Hierarchical Data Format
HOT   Hawaii Optical Time-series
HPLC   High Performance Liquid Chromatography
HRPT   High Resolution Picture Transmission

IDL   Interactive Data Language or International Date Line (depending on usage).

JRC   Joint Research Centre (Ispra, Italy)

LAC   Local Area Coverage

MOBY   Marine Optical Buoy
MOCE   Marine Optical Characterization Experiment
MODIS   Moderate Resolution Imaging Spectroradiometer
MOS   Marine Optical Spectroradiometer

NCEP   National Center for Environmental Prediction
NCSA   National Center for Supercomputing Applications
NDVI   Normalized Difference Vegetation Index
NIR   Near-Infrared

OCTS   Ocean Color and Temperature Sensor (Japan)

PlyMBODy   Plymouth Marine Bio-Optical Data Buoy
PROSOPE   Productivity of Pelagic Oceanic Systems (French translation)

QC   Quality Control

RH   Relative Humidity

SeaBAM   SeaWiFS Bio-optical Algorithm Mini-workshop
SeaBASS   SeaWiFS Bio-optical Archive Storage System
SeaDAS   SeaWiFS Data Analysis System
SeaPRISM   SeaWiFS Photometer Revision for Incident Surface Measurement
SeaWiFS   Sea-viewing Wide Field-of-view Sensor
SIMBIOS   Sensor Intercomparison and Merger for Biological and Interdisciplinary Ocean Studies
SIO   Scripps Institution of Oceanography
SIRREX   SeaWiFS Intercalibration Round-Robin Experiment
SQM   SeaWiFS Quality Monitor
SXR   SeaWiFS Transfer Radiometer

TAO   Tropical Atmosphere–Ocean
TIROS   Television Infrared Observation Satellite
TOA   Top of the Atmosphere
TOGA   Tropical Ocean Global Atmosphere
TOMS   Total Ozone Mapping Spectrometer
TOVS   TIROS Operational Vertical Sounder

UTC   Coordinated Universal Time (definition reflects actual usage instead of following the letters of the acronym)

SYMBOLS

a_0 Constant term of function of illuminated fraction of the lunar surface.
a_1 Linear term of function of illuminated fraction of the lunar surface.

b_0 Constant term of interpolation of lunar phase function.
b_1 Linear term of interpolation of lunar phase function.
b_2 Quadratic term of interpolation of lunar phase function.

$c_1(\lambda)$ Wavelength-dependent phase angle correction factors.
C_a Chlorophyll a.
C_{dark} Dark count from sensor output data.
C_{out} Counts from sensor output data.

d Detector.
D_{IM} SeaWiFS–moon distance in the mean radius of the lunar orbit (R_{M}).
D_{SM} Sun–moon distance in astronomical units (AU).

E_s Surface irradiance.

$f_1(\lambda)$ Illuminated fraction of the lunar surface.
$f_2(\lambda)$ Interpolated lunar phase function.
$f_3(\lambda)$ Difference between measured and fitted integrated lunar radiances.
$f_4(\lambda)$ Correction factor for the variation in the azimuthal angle.
$F_0(\lambda)$ Extraterrestrial solar irradiance adjusted for the Earth–sun distance variations.
F_1 Spatially approximated ozone count for the first ancillary TOMS file.
F_2 Spatially approximated ozone count for the second ancillary TOMS file.
F_i Final interpolated value of approximated ozone count.
f/Q Ocean surface bidirectional reflectance parameter.

g Gain.

G_7 Gain factor for band 7.

G_8 Gain factor for band 8.

$G_{7:8}$ Combined gain for band 7 and 8.

h Shorthand notation variable, see (19).

K Approximated aerosol effects in atmospheric diffuse transmittance.

K_1 Counts-to-radiance conversion factor.

K_2 Detector temperature-dependent correction factor.

K_3 Scan modulation correction.

$K(490)$ Diffuse attenuation coefficient at 490 nm.

K_a Aerosol effects (0.0054) estimated for an aerosol optical thickness of 0.1 and the maritime aerosol model for 90% relative humidity.

$L(\lambda)$ Radiance.

$L_a(\lambda)$ Radiance measured at the TOA from aerosol scattering alone.

L_A Aerosol radiance equal to $L_a + L_{ra}$.

L_B^A L_{WN} ratio constructed from band A divided by band B.

$L_{as}(\lambda)$ Radiance arising from aerosol single scattering.

$L_c(\lambda)$ Fitted integrated lunar radiance.

$L_f(\lambda)$ The foam, or whitecap-leaving, radiance at the sea surface.

$L_g(\lambda)$ Sun glint radiance at the sea surface.

$L_{GN}(\lambda)$ The normalized sun glint radiance.

$L_m(\lambda)$ Measured integrated lunar radiance.

$L_r(\lambda)$ Radiance measured at the TOA from Rayleigh scattering alone.

$L_{ra}(\lambda)$ Radiance at the TOA from Rayleigh-aerosol interactive scattering.

$L_S(\lambda)$ Calibrated at-sensor radiance.

$\hat{L}_t$ Sun glint corrected radiance.

$L_t(\lambda)$ Radiance measured at the TOA.

$L_W(\lambda)$ Water-leaving radiance.

$L_{WN}(\lambda)$ Normalized water-leaving radiance.

$L_{WN}^{S:M}$ The ratios of the SeaWiFS values to the MOBY values for normalized water-leaving radiance.

M Half-angle mirror side correction factor.

ms Half-angle mirror side.

N_M Mean number of scan lines in a lunar image.

N_1 Lunar radiance normalizing factor to a common sun–moon distance.

N_2 Lunar radiance normalizing factor to a common SeaWiFS–moon distance.

N_3 Lunar radiance normalizing factor for the illuminated fraction of the lunar surface.

N_4 Lunar radiance normalizing factor to a common number of scan lines in a lunar image.

N_5 Lunar radiance normalizing factor to a common phase angle.

N_6 Lunar radiance normalizing factor for the wavelength-dependent phase angle correction.

pxl Pixel number along a SeaWiFS scan line.

r Ratio between two aerosol models from the derived ϵ values.

R Distance between two bodies.

R_B Ratio of the SeaWiFS diffuser BRDF to lambertian BRDF.

R_M Mean radius of the lunar orbit.

t Time tag of the sensor output data.

$t(\lambda)$ Diffuse transmittance of the atmosphere at the sensor viewing direction.

t_0 Reference time for temporal corrections to the

T Detector temperature from the sensor output data. radiometric response of the instrument.

$T(\lambda)$ Direct transmittance of the atmosphere at the sensor viewing direction.

$T_0(\lambda)$ Direct transmittance of the atmosphere at the solar direction.

T_c Time of SeaWiFS capture of a scan line.

T_e Sequential day of the year time for the end of TOMS file.

T_m Mid-time.

T_{ref} Detector reference temperature.

T_s Sequential day of the year time for the start of TOMS file.

T_T Sequential day of the year time of TOMS ozone observation along a given longitude.

W_1 Weights used in the temporal approximation of ozone counts for the first ancillary TOMS file.

W_2 Weights used in the temporal approximation of ozone counts for the second ancillary TOMS file.

X Longitude.

α SeaWiFS vicarious gain.

$\alpha(\lambda_i, \lambda_j)$ Ångström coefficient for the wavelengths λ_i and λ_j.

$\alpha^a(\lambda_i, 865)$ Ångström exponent from the derived model a.

$\alpha^b(\lambda_i, 865)$ Ångström exponent from the derived model b.

β Constant term in the temporal correction to the radiomteric response of the instrument.

γ Linear term in the temporal correction to the radiometric response of the instrument.

δ Quadratic term in the temporal correction to the radiometric response of the instrument.

ΔT Difference of scan line time from the beginning of the TOMS file.

ΔT_1 ΔT value converted into weights for the old and new processing.

ΔT_2 ΔT value converted into weights for the old and new processing.

ΔT^N Difference in Julian time between SeaWiFS and TOMS observations for the new algorithm.

ΔT^O Difference in Julian time between SeaWiFS and TOMS observations for the old algorithm.

$\epsilon(765, 865)$ Atmospheric correction parameter.

$\epsilon(\lambda, 865)$ ϵ value of atmospheric correction for wavelengths λ and 865 nm.

$\epsilon(\lambda_i, \lambda_j)$ Ratio of single-scattered aerosol reflectance between two wavelengths, $\rho_{as}(\lambda_i)/\rho_{as}(\lambda_j)$.

θ Sensor zenith angle.

θ_0 Solar zenith angle.

ϑ Phase angle of the lunar calibrations.

λ Wavelength.

λ_i, λ_j Wavelengths corresponding to sensor spectral bands i and j.

ρ Reflectance.

$\rho_a(\lambda)$ Reflectance measured at the TOA from aerosol scattering alone.

ρ_A Aerosol reflectance.

$\rho_{as}(\lambda)$ Single-scattered aerosol reflectance.

$\rho_f(\lambda)$ Reflectance at the sea surface from foam (or whitecaps).

$\rho_r(\lambda)$ Reflectance measured at the TOA from Rayleigh scattering alone.

$\rho_{ra}(\lambda)$ Reflectance at the TOA from Rayleigh-aerosol interactive scattering.

$\rho_t(\lambda)$ Reflectance measured at the TOA.

$\rho_W(\lambda)$ Water-leaving reflectance at the sea surface.

σ Standard deviation.

$\sigma(X)$ Standard deviation of quantity X.

$\tau_a(\lambda)$ Aerosol optical thickness.

$\tau_a'(\lambda_i)$ Initial estimate for $\tau_a(\lambda)$.

$\tau_{\mathrm{oz}}(\lambda)$ Ozone optical thickness.

$\tau_r(\lambda)$ Rayleigh (air molecules) optical thickness.

ϕ Azimuthal angle.

φ Azimuthal angle of incident sunlight on the Sea-WiFS diffuser

ψ Angle of rotation in azimuth relative to the Sea-WiFS diffuser.

References

Aiken, J., D.G. Cummings, S.W. Gibb, N.W. Rees, R. Woodd-Walker, E.M.S. Woodward, J. Woolfenden, S.B. Hooker, J-F. Berthon, C.D. Dempsey, D.J. Suggett, P. Wood, C. Donlon, N. González-Benítez, I. Huskin, M. Quevedo, R. Barciela-Fernandez, C. de Vargas, and C. McKee, 1998: AMT-5 Cruise Report. *NASA Tech. Memo. 1998–206892, Vol. 2,* S.B. Hooker and E.R. Firestone, Eds., NASA Goddard Space Flight Center, Greenbelt, Maryland, 113 pp.

——, N.W. Rees, S. Hooker, P. Holligan, A. Bale, D. Robins, G. Moore, R. Harris, and D. Pilgrim, 2000: The Atlantic Meridional Transect: overview and synthesis of data. *Prog. Oceanogr.,* **45,** 257–312.

Ainsworth, E.J., and F.S. Patt, 2000: "Modifications to the TOMS ozone ancillary data interpolation." In: McClain, C.R., E.J. Ainsworth, R.A. Barnes, R.E. Eplee, Jr., F.S. Patt, W.D. Robinson, M. Wang, and S.W. Bailey, Sea-WiFS Postlaunch Calibration and Validation Analyses, Part 1. *NASA Tech. Memo. 2000–206892, Vol. 9,* S.B. Hooker and E.R. Firestone, Eds., NASA Goddard Space Flight Center, Greenbelt, Maryland, 69–73.

Bailey, S.W., C.R. McClain, P.J. Werdell, and B.D. Schieber, 2000: "Normalized water-leaving radiance and chlorophyll *a* match-up analyses." In: McClain, C.R., R.A. Barnes, R.E. Eplee, Jr., B.A. Franz, N.C. Hsu, F.S. Patt, C.M. Pietras, W.D. Robinson, B.D. Schieber, G.M. Schmidt, M. Wang, S.W. Bailey, and P.J. Werdell, 2000: SeaWiFS Postlaunch Calibration and Validation Analyses, Part 2. *NASA Tech. Memo. 2000–206892, Vol. 10,* S.B. Hooker and E.R. Firestone, Eds., NASA Goddard Space Flight Center, Greenbelt, Maryland, 45–52.

Barnes, R.A., and R.E. Eplee, 1996: "The SeaWiFS solar diffuser." In: Barnes, R.A., E-n. Yeh, and R.E. Eplee, 1996: SeaWiFS Calibration Topics, Part 1, *NASA Tech. Memo. 104566, Vol. 39,* S.B. Hooker and E.R. Firestone, Eds., NASA Goddard Space Flight Center, Greenbelt, Maryland, 54–61.

——, ——, and F.S. Patt, 1998: "SeaWiFS measurements of the moon." In: Sensors, Systems, and Next-Generation Satellites II, *SPIE,* **3498,** 311–324.

——, and C.R. McClain, 1999: "The calibration of SeaWiFS after two years on orbit." In: Sensors, Systems, and Next-Generation Satellites V, *SPIE,* **3870,** 214–227.

——, R.E. Eplee, Jr., F.S. Patt, and C.R. McClain, 1999a: Changes in the radiometric sensitivity of SeaWiFS determined from lunar and solar-based measurements. *Appl. Opt.,* **38,** 4,649–4,664.

——, ——, S.F. Biggar, K.J. Thome, E.F. Zalewski, P.M. Slater, and A.W. Holmes, 1999b: The SeaWiFS Solar Radiation-Based Calibration and the Transfer-to-Orbit Experiment. *NASA Tech. Memo. 1999–206892, Vol. 5,* S.B. Hooker and E.R. Firestone, Eds., NASA Goddard Space Flight Center, Greenbelt, Maryland, 28 pp.

Brown, C.W., 1995: "Classification of coccolithophore blooms in ocean color imagery." In: McClain, C.R., W.E. Esaias, M. Darzi, F.S. Patt, R.H. Evans, J.W. Brown, K.R. Arrigo, C.W. Brown, R.A. Barnes, and L. Kumar, 1995: Case Studies for SeaWiFS Calibration and Validation, Part 4. *NASA Tech. Memo. 104566, Vol. 28,* S.B. Hooker, E.R. Firestone, and J.G. Acker, Eds., NASA Goddard Space Flight Center, Greenbelt, Maryland, 13–19.

——, and J.A. Yoder, 1994: Coccolithophorid blooms in the global ocean. *J. Geophys. Res.,* **99,** 7,467–7,482.

Clark, D., H.R. Gordon, K.J. Voss, Y. Ge, W. Broenkow, and C. Trees, 1997: Validation of atmospheric correction over the oceans. *J. Geophys. Res.,* **102,** 17,209-17,217.

Cox, C., and W. Munk, 1954: Measurements of the roughness of the sea surface from photographs of the sun's glitter. *J. Opt. Soc. Am.,* **44,** 838–850.

Darzi, M., 1998: SeaWiFS Algorithm Flow Chart. *NASA Contractor Report 1998–206848,* NASA Goddard Space Flight Center, Greenbelt, Maryland, 36 pp.

——, F.S. Patt, and L. Kumar, 1995: "Algorithm for the application of the sensor calibration for SeaWiFS level-2 processing." In: McClain, C.R., K. Arrigo, W.E. Esaias, M. Darzi, F.S. Patt, R.H. Evans, J.W. Brown, C.W. Brown, R.A. Barnes, and L. Kumar, 1995: SeaWiFS Algorithms, Part 1. *NASA Tech. Memo. 104566, Vol. 28,* S.B. Hooker, E.R. Firestone, and J.G. Acker, Eds., NASA Goddard Space Flight Center, Greenbelt, Maryland, 26–32.

Eplee, R.E., Jr., and R.A. Barnes, 2000: "Lunar data analysis for SeaWiFS calibration." In: McClain, C.R., E.J. Ainsworth, R.A. Barnes, R.E. Eplee, Jr., F.S. Patt, W.D. Robinson, M. Wang, and S.W. Bailey, 2000: SeaWiFS Postlaunch Calibration and Validation Analyses, Part 1. *NASA Tech. Memo. 2000–206892, Vol. 9,* S.B. Hooker and E.R. Firestone, Eds., NASA Goddard Space Flight Center, Greenbelt, Maryland, 17–27.

——, and C.R. McClain, 2000: "MOBY data analysis for vicarious calibration of SeaWiFS." In: McClain, C.R., E.J. Ainsworth, R.A. Barnes, R.E. Eplee, Jr., F.S. Patt, W.D. Robinson, M. Wang, and S.W. Bailey, 2000: SeaWiFS Postlaunch Calibration and Validation Analyses, Part 1. *NASA Tech. Memo. 2000–206892, Vol. 9,* S.B. Hooker and E.R. Firestone, Eds., NASA Goddard Space Flight Center, Greenbelt, Maryland, 43–50.

——, and F.S. Patt, 2000: "Cloud-top radiance analysis for SeaWiFS bilinear gain knee calibration." In: McClain, C.R., E.J. Ainsworth, R.A. Barnes, R.E. Eplee, Jr., F.S. Patt, W.D. Robinson, M. Wang, and S.W. Bailey, 2000: SeaWiFS Postlaunch Calibration and Validation Analyses, Part 1. *NASA Tech. Memo. 2000–206892, Vol. 9,* S.B. Hooker and E.R. Firestone, Eds., NASA Goddard Space Flight Center, Greenbelt, Maryland, 13–16.

——, R.A. Barnes, and F.S. Patt, 2000: "Solar data analysis for SeaWiFS calibration." In: McClain, C.R., E.J. Ainsworth, R.A. Barnes, R.E. Eplee, Jr., F.S. Patt, W.D. Robinson, M. Wang, and S.W. Bailey, 2000: SeaWiFS Postlaunch Calibration and Validation Analyses, Part 1. *NASA Tech. Memo. 2000–206892, Vol. 9,* S.B. Hooker and E.R. Firestone, Eds., NASA Goddard Space Flight Center, Greenbelt, Maryland, 28–37.

Evans, R.H., and H.R. Gordon, 1994: Coastal zone color scanner "system calibration": A retrospective examination. *J. Geophys. Res.,* **99,** 7,293–7,307.

Firestone, J.K., R.H. Woodward, and C.R. McClain, 1994: "An evaluation of surface wind products for use in SeaWiFS." In: McClain, C.R., R.S. Fraser, J.T. McLean, M. Darzi, J.K. Firestone, F.S. Patt, B.D. Schieber, R.H. Woodward, E-n. Yeh, S. Mattoo, S.F. Biggar, P.N. Slater, K.J. Thome, A.W. Holmes, R.A. Barnes, and K.J. Voss, 1994: Case Studies for SeaWiFS Calibration and Validation, Part 2. *NASA Tech. Memo. 104566, Vol. 19,* S.B. Hooker and E.R. Firestone, Eds., NASA Goddard Space Flight Center, Greenbelt, Maryland, 50–64.

Fraser, R.S., S. Mattoo, E-n. Yeh, and C.R. McClain, 1997: Algorithm for atmospheric and glint corrections of satellite measurements of ocean pigment. *J. Geophys. Res.,* **102,** 17,107–17,118.

Frouin, R., M. Schwindling, and P.Y. Deschamps, 1996: Spectral reflectance of sea foam in the visible and near infrared: *In situ* measurements and remote sensing implications. *J. Geophys. Res.,* **101,** 14,361–14,371.

Gordon, H.R., 1995: Remote sensing of ocean color: a methodology for dealing with broad spectral bands and significant out-of-band response. *Appl. Opt.,* **34,** 8,363–8,374.

——, 1998: In-orbit calibration strategy for ocean color sensors. *Remote Sens. Environ.,* **63,** 265–278.

——, and D.K. Clark, 1981: Clear water radiances for atmospheric correction of coastal zone color scanner imagery. *Appl. Opt.,* **20,** 4,175–4,180.

——, J.W. Brown, and R.H. Evans, 1988: Exact Rayleigh scattering calculations for use with the Nimbus-7 Coastal Zone Color Scanner. *Appl. Opt.,* **27,** 862–871.

——, and M. Wang, 1992: Surface roughness considerations for atmospheric correction of ocean color sensors. 1: Rayleigh scattering component. *Appl. Opt.,* **31,** 4,247–4,260.

——, and ——, 1994a: Retrieval of water-leaving radiance and aerosol optical thickness over the oceans with SeaWiFS: a preliminary algorithm. *Appl. Opt.,* **33,** 443–452.

——, and ——, 1994b: Influence of oceanic whitecaps on atmospheric correction of ocean color sensors. *Appl. Opt.,* **33,** 7,354–7,763.

Gregg, W.W., F.S. Patt, and R.H. Woodward, 1993: The Simulated SeaWiFS Data Set, Version 1. *NASA Tech. Memo. 104566, Vol. 9,* S.B. Hooker, E.R. Firestone, and A.W. Indest, Eds., NASA Goddard Space Flight Center, Greenbelt, Maryland, 17 pp.

——, ——, A.L. Mezaache, J.D. Chen, J.A. Whiting, 1994: The Simulated SeaWiFS Data Set, Version 2. *NASA Tech. Memo. 104566, Vol. 15,* S.B. Hooker and E.R. Firestone, Eds., NASA Goddard Space Flight Center, Greenbelt, Maryland, 42 pp., plus color plates.

Hapke, B., 1986: Bidirectional reflectance spectroscopy. 4. Extinction and the opposition effect. *Icarus,* **67,** 246–280.

Helfenstein, P., and J. Veverka, 1987: Photometric properties of lunar terrains derived from Hapke's equation. *Icarus,* **72,** 342–357.

Hooker, S.B., W.E. Esaias, G.C. Feldman, W.W. Gregg, and C.R. McClain, 1992: An Overview of SeaWiFS and Ocean Color, *NASA Tech. Memo. 104566, Vol. 1,* S.B. Hooker and E.R. Firestone, Eds., NASA Goddard Space Flight Center, Greenbelt, Maryland, 25 pp., plus color plates.

——, and J. Aiken, 1998: Calibration evaluation and radiometric testing of field radiometers with the SeaWiFS Quality Monitor. *J. Atmos. Ocean. Tech.,* **15,** 995–1,007.

——, G. Zibordi, G. Lazin, and S. McLean, 1999: The Sea-BOARR-98 Field Campaign. *NASA Tech. Memo. 1999–206892, Vol. 3,* S.B. Hooker and E.R. Firestone, Eds., NASA Goddard Space Flight Center, Greenbelt, Maryland, 40 pp.

——, and C.R. McClain, 2000: A comprehensive plan for the calibration and validation of SeaWiFS data. *Prog. Oceanogr.,* **45,** 427–465.

——, and S. Maritorena, 2000: An evaluation of oceanographic radiometers and deployment methodologies. *J. Atmos. Ocean. Tech.,* **17,** 811–830.

Hsu, N.C., W.D. Robinson, S.W. Bailey, and P.J. Werdell, 2000: "The description of the SeaWiFS absorbing aerosol index." In: McClain, C.R., R.A. Barnes, R.E. Eplee, Jr., B.A. Franz, N.C. Hsu, F.S. Patt, C.M. Pietras, W.D. Robinson, B.D. Schieber, G.M. Schmidt, M. Wang, S.W. Bailey, and P.J. Werdell, 2000: SeaWiFS Postlaunch Calibration and Validation Analyses, Part 2. *NASA Tech. Memo. 2000–206892, Vol. 10,* S.B. Hooker and E.R. Firestone, Eds., NASA Goddard Space Flight Center, Greenbelt, Maryland, 3–5.

Johnson, B.C., F. Sakuma, J.J. Butler, S.F. Biggar, J.W. Cooper, J. Ishida, and K. Suzuki, 1997: Radiometric measurement comparison using the Ocean Color and Temperature Scanner (OCTS) visible and near infrared integrating sphere. *J. Res. Natl. Inst. Stand. Technol.,* **102,** 627–646.

——, P-S Shaw, S.B. Hooker, and D. Lynch, 1998: Radiometric and engineering performance of the SeaWiFS Quality Monitor (SQM): a portable light source for field radiometers. *J. Atmos. Ocean. Technol.,* **15,** 1,008–1,022.

——, E.E. Early, R.E. Eplee, Jr., R.A. Barnes, and R.T. Caffrey, 1999: The 1997 Prelaunch Radiometric Calibration of SeaWiFS. *NASA Tech. Memo. 1999–206892, Vol. 4,* S.B. Hooker and E.R. Firestone, Eds., NASA Goddard Space Flight Center, Greenbelt, Maryland, 51 pp.

Kieffer, H.H., and J.M. Anderson, 1998: "Use of the moon for spacecraft calibration over 350–2500 nm." In: Sensors, Systems, and Next-Generation Satellites II, *SPIE,* **3498,** 325–336.

Koepke, P., 1984: Effective reflectance of oceanic whitecaps. *Appl. Opt.,* **23,** 1,816–1,824.

Lane, A.P., and W.M. Irvine, 1973: Monochromatic phase curves and albedos for the lunar disk. *Astron. J.,* **78,** 267–277.

McClain, C.R., W.E. Esaias, W. Barnes, B. Guenther, D. Endres, S.B. Hooker, G. Mitchell, and R. Barnes, 1992: Calibration and Validation Plan for SeaWiFS. *NASA Tech. Memo. 104566, Vol. 3,* S.B. Hooker and E.R. Firestone, Eds., NASA Goddard Space Flight Center, Greenbelt, Maryland, 41 pp.

——, R.H. Evans, J.W. Brown, and M. Darzi, 1995: "SeaWiFS quality control masks and flags: initial algorithms and implementation strategy." In: McClain, C.R., W.E. Esaias, M. Darzi, F.S. Patt, R.H. Evans, J.W. Brown, K.R. Arrigo, C.W. Brown, R.A. Barnes, and L. Kumar, 1995: Case Studies for SeaWiFS Calibration and Validation, Part 4. *NASA Tech. Memo. 104566, Vol. 28,* S.B. Hooker, E.R. Firestone, and J.G. Acker, Eds., NASA Goddard Space Flight Center, Greenbelt, Maryland, 3–7.

——, M. Darzi, R.A. Barnes, R.E. Eplee, Jr., J.K. Firestone, F.S. Patt, W.D. Robinson, B.D. Schieber, R.H. Woodward, and E-n. Yeh, 1996: SeaWiFS Calibration and Validation Quality Control Procedures. *NASA Tech. Memo. 104566, Vol. 38,* S.B. Hooker and E.R. Firestone, Eds., NASA Goddard Space Flight Center, Greenbelt, Maryland, 68 pp.

——, M.L. Cleave, G.C. Feldman, W.W. Gregg, S.B. Hooker, and N. Kuring, 1998: Science quality SeaWiFS data for global biosphere research. *Sea Technol.,* **39,** 10–16.

——, and G.S. Fargion, 1999: SIMBIOS Project 1998 Annual Report. *NASA Tech. Memo. 1999–208645,* NASA Goddard Space Flight Center, Greenbelt, Maryland, 105 pp.

Monahan, E.C., 1971: Oceanic whitecaps. *J. Phys. Oceanogr.,* **1,** 139–144.

Moore, K.D., K.J. Voss, and H.R. Gordon, 1998: Spectral reflectance of whitecaps: Instrumentation, calibration, and performance in coastal waters. *J. Atmos. Ocean. Tech.,* **15,** 496–509.

——, ——, and ——, 2000: Spectral reflectance of whitecaps: Their contribution to water-leaving radiance. *J. Geophys. Res.,* **105,** 6,493–6,499.

Morel, A., and B. Gentili, 1996: Diffuse reflectance of oceanic waters. III. Implication of bidirectionality for the remote sensing problem, *Appl. Opt.,* **35,** 4,850–4,862.

Mueller J.L., 2000: "SeaWiFS algorithm for the diffuse attenuation coefficient, $K(490)$, using water-leaving radiances at 490 and 555 nm."In: O'Reilly, J.E., and 24 Coauthors, SeaWiFS Postlaunch Calibration and Validation Analyses, Part 3. *NASA Tech. Memo. 2000–206892, Vol. 11,* S.B. Hooker and E.R. Firestone, Eds., NASA Goddard Space Flight Center, Greenbelt, Maryland, 24–27.

O'Reilly, J.E., S. Maritorena, B.G. Mitchell, D.A. Siegel, K.L. Carder, S.A. Garver, M. Kahru, and C. McClain, 1998: Ocean color chlorophyll algorithms for SeaWiFS. *J. Geophys. Res.,* **103,** 24,937–24,953.

——, and 21 Coauthors, 2000: "Ocean color chlorophyll *a* algorithms for SeaWiFS, OC2, and OC4: Version 4," In: O'Reilly, J.E., and 24 Coauthors, 2000: SeaWiFS Postlaunch Calibration and Validation Analyses, Part 3. *NASA Tech. Memo. 2000–206892, Vol. 11,* S.B. Hooker and E.R. Firestone, Eds., NASA Goddard Space Flight Center, Greenbelt, Maryland, 9–23.

Robins, D.B., A.J. Bale, G.F. Moore, N.W. Rees, S.B. Hooker, C.P. Gallienne, A.G. Westbrook, E. Marañón, W.H. Spooner, and S.R. Laney, 1996: AMT-1 Cruise Report and Preliminary Results. *NASA Tech. Memo. 104566, Vol. 35,* S.B. Hooker and E.R. Firestone, Eds., NASA Goddard Space Flight Center, Greenbelt, Maryland, 87 pp.

Robinson, W.D., and M. Wang, 2000: "Vicarious calibration of SeaWiFS band 7." In: McClain, C.R., E.J. Ainsworth, R.A. Barnes, R.E. Eplee, Jr., F.S. Patt, W.D. Robinson, M. Wang, and S.W. Bailey, 2000: SeaWiFS Postlaunch Calibration and Validation Analyses, Part 1. *NASA Tech. Memo. 2000–206892, Vol. 9,* S.B. Hooker and E.R. Firestone, Eds., NASA Goddard Space Flight Center, 38–42.

——, G.M. Schmidt, C.R. McClain, and P.J. Werdell, 2000: "Changes made in the operational SeaWiFS processing." In: McClain, C.R., R.A. Barnes, R.E. Eplee, Jr., B.A. Franz, N.C. Hsu, F.S. Patt, C.M. Pietras, W.D. Robinson, B.D. Schieber, G.M. Schmidt, M. Wang, S.W. Bailey, and P.J. Werdell, 2000: SeaWiFS Postlaunch Calibration and Validation Analyses, Part 2. *NASA Tech. Memo. 2000–206892, Vol. 10,* S.B. Hooker and E.R. Firestone, Eds., NASA Goddard Space Flight Center, Greenbelt, Maryland, 12–28.

Shettle, E.P., and R.W. Fenn, 1979: Models for the Aerosols of the Lower Atmosphere and the Effects of Humidity Variations on Their Optical Properties. *AFGL-TR-79-0214,* U.S. Air Force Geophysics Laboratory, Hanscom Air Force Base, Massachusetts, 94 pp.

Siegel, D.A., M. Wang, S. Maritorena, and W. Robinson, 2000: Atmospheric correction of satellite ocean color imagery: the black pixel assumption. *Appl. Opt.,* **39,** 3,582–3,591.

Vance, T.C., J.D. Schumacher, P.J. Stabeno, C.T. Baier, T. Wyllie-Echeverria, C.T. Tynan, R.D. Brodeur, J.M. Napp, K.O. Coyle, M.B. Decker, G.L. Hunt Jr., D. Stockwell, T.E. Whitledge, M. Jump, and S. Zeeman, 1998: Aquamarine waters recorded for the first time in the Eastern Bering Sea. *EOS,* **79,** 121 and 126.

Wang, M., 1999: Atmospheric correction of ocean color sensors: Computing atmospheric diffuse transmittance. *Appl. Opt.,* **38,** 451–455.

——, 2000: "The SeaWiFS atmospheric correction algorithm updates." In: McClain, C.R., E.J. Ainsworth, R.A. Barnes, R.E. Eplee, Jr., F.S. Patt, W.D. Robinson, M. Wang, and S.W. Bailey, 2000: SeaWiFS Postlaunch Calibration and Validation Analyses, Part 1. *NASA Tech. Memo. 2000–206892, Vol. 9,* S.B. Hooker and E.R. Firestone, Eds., NASA Goddard Space Flight Center, Greenbelt, Maryland, 57–63.

——, and H.R. Gordon, 1994: A simple, moderately accurate, atmospheric correction algorithm for SeaWiFS. *Remote Sens. Environ.,* **50,** 231–239.

——, and B. Franz, 2000: Comparing the ocean color measurements between MOS and SeaWiFS: A vicarious intercalibration approach for MOS. *IEEE Trans. Geosci. Remote Sens.,* **38,** 184–197.

——, and S.W. Bailey, 2000: "Correction of the sun glint contamination on the SeaWiFS aerosol optical thickness retrievals." In: McClain, C.R., E.J. Ainsworth, R.A. Barnes, R.E. Eplee, Jr., F.S. Patt, W.D. Robinson, M. Wang, and S.W. Bailey, 2000: SeaWiFS Postlaunch Calibration and Validation Analyses, Part 1. *NASA Tech. Memo. 2000–206892, Vol. 9,* S.B. Hooker and E.R. Firestone, Eds., NASA Goddard Space Flight Center, Greenbelt, Maryland, 64–68.

——, ——, C.M. Pietras, and C.R. McClain, 2000: "SeaWiFS aerosol optical thickness match-up analyses." In: McClain, C.R., R.A. Barnes, R.E. Eplee, Jr., B.A. Franz, N.C. Hsu, F.S. Patt, C.M. Pietras, W.D. Robinson, B.D. Schieber, G.M. Schmidt, M. Wang, S.W. Bailey, and P.J. Werdell, 2000: SeaWiFS Postlaunch Calibration and Validation Analyses, Part 2. *NASA Tech. Memo. 2000–206892, Vol. 10,* S.B. Hooker and E.R. Firestone, Eds., NASA Goddard Space Flight Center, Greenbelt, Maryland, 39–44.

Woodward, R.H., R.A. Barnes, C.R. McClain, W.E. Esaias, W.L. Barnes, and A.T. Mecherikunnel, 1993: Modeling of the SeaWiFS Solar and Lunar Observations. *NASA Tech. Memo. 104566, Vol. 10,* S.B. Hooker and E.R. Firestone, Eds., NASA Goddard Space Flight Center, Greenbelt, Maryland, 26 pp.

Yang, H., and H.R. Gordon, 1997: Remote sensing of ocean color: assessment of water-leaving radiance bidirectional effects on atmospheric diffuse transmittance. *Appl. Opt.,* **36,** 7,887–7,897.

Zibordi, G., J.P. Doyle, and S.B. Hooker, 1999: Offshore tower shading effects on in-water optical measurements. *J. Atmos. Ocean. Tech.,* **16,** 1,767–1,779.

The SeaWiFS Postlaunch Technical Report Series

Vol. 1

Johnson, B.C., J.B. Fowler, and C.L. Cromer, 1998: The SeaWiFS Transfer Radiometer (SXR). *NASA Tech. Memo. 1998–206892, Vol. 1,* S.B. Hooker and E.R. Firestone, Eds., NASA Goddard Space Flight Center, Greenbelt, Maryland, 58 pp.

Vol. 2

Aiken, J., D.G. Cummings, S.W. Gibb, N.W. Rees, R. Woodd-Walker, E.M.S. Woodward, J. Woolfenden, S.B. Hooker, J-F. Berthon, C.D. Dempsey, D.J. Suggett, P. Wood, C. Donlon, N. González-Benítez, I. Huskin, M. Quevedo, R. Barciela-Fernandez, C. de Vargas, and C. McKee, 1998: AMT-5 Cruise Report. *NASA Tech. Memo. 1998–206892, Vol. 2,* S.B. Hooker and E.R. Firestone, Eds., NASA Goddard Space Flight Center, Greenbelt, Maryland, 113 pp.

Vol. 3

Hooker, S.B., G. Zibordi, G. Lazin, and S. McLean, 1999: The SeaBOARR-98 Field Campaign. *NASA Tech. Memo. 1999–206892, Vol. 3,* S.B. Hooker and E.R. Firestone, Eds., NASA Goddard Space Flight Center, Greenbelt, Maryland, 40 pp.

Vol. 4

Johnson, B.C., E.A. Early, R.E. Eplee, Jr., R.A. Barnes, and R.T. Caffrey, 1999: The 1997 Prelaunch Radiometric Calibration of SeaWiFS. *NASA Tech. Memo. 1999–206892, Vol. 4,* S.B. Hooker and E.R. Firestone, Eds., NASA Goddard Space Flight Center, Greenbelt, Maryland, 51 pp.

Vol. 5

Barnes, R.A., R.E. Eplee, Jr., S.F. Biggar, K.J. Thome, E.F. Zalewski, P.N. Slater, and A.W. Holmes 1999: The SeaWiFS Solar Radiation-Based Calibration and the Transfer-to-Orbit Experiment. *NASA Tech. Memo. 1999–206892, Vol. 5,* S.B. Hooker and E.R. Firestone, Eds., NASA Goddard Space Flight Center, 28 pp.

Vol. 6

Firestone, E.R., and S.B. Hooker, 2000: SeaWiFS Postlaunch Technical Report Series Cumulative Index: Volumes 1–5. *NASA Tech. Memo. 2000–206892, Vol. 6,* S.B. Hooker and E.R. Firestone, Eds., NASA Goddard Space Flight Center, Greenbelt, Maryland, 14 pp.

Vol. 7

Johnson, B.C., H.W. Yoon, S.S. Bruce, P-S. Shaw, A. Thompson, S.B. Hooker, R.E. Eplee, Jr., R.A. Barnes, S. Maritorena, and J.L. Mueller, 1999: The Fifth SeaWiFS Intercalibration Round-Robin Experiment (SIRREX-5), July 1996. *NASA Tech. Memo. 1999–206892, Vol. 7,* S.B. Hooker and E.R. Firestone, Eds., NASA Goddard Space Flight Center, 75 pp.

Vol. 8

Hooker, S.B., and G. Lazin, 2000: The SeaBOARR-99 Field Campaign. *NASA Tech. Memo. 2000–206892, Vol. 8,* S.B. Hooker and E.R. Firestone, Eds., NASA Goddard Space Flight Center, 46 pp.

81

Vol. 9

McClain, C.R., E.J. Ainsworth, R.A. Barnes, R.E. Eplee, Jr.,
F.S. Patt, W.D. Robinson, M. Wang, and S.W. Bailey,
2000: SeaWiFS Postlaunch Calibration and Validation
Analyses, Part 1. *NASA Tech. Memo. 2000–206892, Vol.
9,* S.B. Hooker and E.R. Firestone, Eds., NASA Goddard
Space Flight Center, 82 pp.